MONTE CARLO NEUTRONIC SIMULATIONS FOR A NEW APPROACH TO

PARAMETRIC INAA AND Mo-99 PRODUCTION FEASIBILITY AT MURR

_____

A Dissertation presented to

the Faculty of the Graduate School

at the University of Missouri-Columbia

_____

In Partial Fulfillment

of the Requirements for the Degree

Doctor of Philosophy

_____

by

NICKIE J.J. PETERS

Dr. John David Robertson, Dissertation Supervisor

August 2009

ACKNOWLEDGMENTS

ABSTRACT

A novel approach to parametric instrumental neutron activation analysis at MURR has been established. In particular, a detailed MCNP5 steady-state model of the MURR core was developed. The model, which was based on the most recent continuous-energy neutron data from the ENDF and JEFF libraries, was used to compute the local continuous-energy neutron flux distribution. By coupling the computed flux spectrum to the energy-dependent (n, γ) cross-sections for a range of nuclides, their intrinsic reaction rates were predicted in irradiation channel ROW2. The model was initially benchmarked by measuring the intrinsic (n, γ) reaction rates for a set of mostly dilute single-element standards in ROW2.

Results show that the model predicts the absolute reaction rates of many nuclides including those with high epithermal sensitivity (e.g., Au-197 and Zr-96), and non-1/v nuclides (e.g. Lu-176) within ±5% of the measured values. Using predicted (n, γ) reaction-rates characterized as the parameter π_{theo}, trace-elemental concentrations were determined in NIST standard reference materials, bovine liver, obsidian and coal fly ash. The agreements with the certified values were generally within ±5%. The new methodology has produced agreements with the certified values that are better for a greater number of elements than k_0. The model was also combined with MONTEBURNS and ORIGEN to test the feasibility of Mo-99 production at MURR from fissioning LEU. Results from a 5-gram low-enriched uranium target show predictions of Mo-99 end-of-irradiation yields are within 3% of the measured value. This dissertation entails a complete study of the MCNP5 model and the new neutron activation analysis method.

CONTENTS

List of Figures .... Page

Chapter 1 Introduction

1.1 Overview of Neutron Activation Analysis

Neutron activation analysis (NAA) is a powerful analytical technique used to determine trace-elemental concentrations in the ppm to ppb range. NAA was first developed in the mid 1930's by George F. de Hevesy. Here, it was discovered that elements in a sample can be identified after exposure to a neutron field using the different gamma rays emitted [1, 2]. It was revealed that the emitted gamma rays resulted from a neutron capture nuclear interaction with the different nuclei in the sample. In particular, the gamma rays are primarily produced following the radioactive decay of the product from an ^{A}X (n, γ) $^{(A+1)}Y$ nuclear reaction. Figure 1.1 shows a schematic of a neutron capture nuclear interaction.
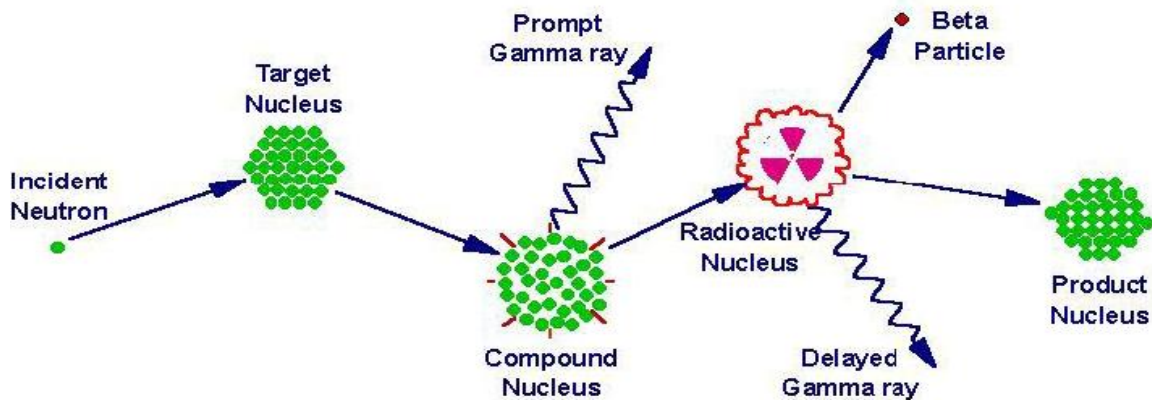
Fig. 1.1 A schematic of a neutron capture nuclear reaction. The delayed gamma ray is characteristic of the radioactive daughter nucleus [3].

The method became practically applicable in the 1950's when reactor neutron sources became available. Since then, several different modes of the NAA technique have been developed which utilize either the energy of the neutrons or the type of emitted gamma rays. Those NAA techniques that employ only epithermal neutrons (i.e., 0.5 eV $\leq E_n \leq$ 0.1 eV) or fast neutrons (i.e., $E_n \geq$ 0.1) eV) are called epithermal neutron activation analysis (ENAA) and fast neutrons activation analysis (FNAA), respectively. Prompt-gamma neutron activation analysis (PGNAA) utilizes the prompt gamma rays that are emitted during the formation of the compound nucleus in the (n, γ) reaction. However, these techniques are for specialized analyses. The most applicable form of NAA is the conventional approach which utilizes the delayed gamma rays produced by irradiation with thermal neutrons. Over 60% of all elements are measurable by standard NAA.

NAA is a widely used analytical technique in many applications today. Recent reviews of the importance of NAA in applications ranging from the analysis of environmental pollutants, the food and silk industry, and biomedical studies can be found in references [4-6]. A set of review publications on the use of spectroscopic techniques in the Journal of Geostandards and Geoanalytical Research between 2004 − 2008 [7-9] referred to NAA as a mature technique and shows that the number of publications from 2003 - 2007 based in the technique initially declined, but stabilized to represent a small but steady fraction (4.5%) of the total publications in the geo-analytical (spectroscopic) field. However, the lower number of research publications in NAA have been mainly attributed to the limited access due to security risks and the costly nature of nuclear reactor facilities. A review in 2004 [10] compared NAA to the new powerful analytical technique, inductively-coupled plasma mass spectroscopy (ICP-MS) [11, 12], for

applications in geosciences. Here [10], it is reported that both the limit of detection and dynamic range of elements by the NAA method are super-ceded by ICP-MS. In light of this, NAA does offer advantages over such techniques which include the ability to analyze both large and small samples, and performing measurements without destroying the samples in contrast to methods such as ICP-MS, where a complete digestion of the sample is required. Depending on the sample, digestion times can be extensive. However, this is not the case, in particular for instrumental NAA; here, no chemical processing is involved. For this reason, INAA is non-destructive and virtually free of any potential contamination during sample preparation. In addition, INAA is free of chemical matrix interferences unlike most other spectroscopic techniques such as ICP-MS.

In most instrumental NAA methodologies, the concentration of an element in the sample can be determined by measuring the specific activity of the radioactive daughter nuclide using the delayed gamma rays [1, 2, 13, 14]. The basic equation in NAA from which the measured activity is determined, begins with the relationship

$$R_c = A I \varepsilon \tag{1.1}$$

where R_c is the measured count rate from the sample, A is the measured activity, I is the gamma abundance and ε is the gamma ray detection efficiency. Theoretically, A can be written exactly as

$$A = n_{target} S D C \int_0^\infty \phi_n(E) \sigma_c(E) dE \tag{1.2}$$

where n_{target} is the number of target atoms of the analyte, $\phi_n(E)$ is the continuous-energy neutron flux spectrum, $\sigma_c(E)$ is the energy-dependent neutron capture cross-section, and S, D and C are corrections for decay, saturation and counting, respectively. Following

3

equation 1.2, it is evident that the sensitivity of an NAA measurement depends on a number of factors including decay, counting, irradiation times, detector efficiencies, gamma ray and isotopic abundances and the energy-dependent neutron flux. Of these parameters, the neutron flux distribution is most difficult to address since there are no experimental ways to measure the exact functional form of the local neutron distribution at the irradiation positions at reactor facilities. There are flux-unfolding techniques [15] that use flux monitors to determine the flux spectrum. However, the unfolded flux spectrum is group-wise or bin structured with limited energy resolution since the flux monitors used are individually sensitive unique energy regions. Up until now, flux models used in equation 1.2 were lacking the details of a realistic $\phi_n(E)$.

To avoid errors and complications introduced by the variations in an unknown local $\phi_n(E)$, most instrumental NAA (INAA) measurements employ the standard comparator (relative) method [14, 16]. In the comparator method, a well known reference standard for each element to be determined is irradiated under identical conditions as the sample. Therefore, the expression to determine elemental concentration is reduced to a simple ratio of corrected specific activities between the standard comparator and the sample, which is given as

$$\rho = \frac{\left[\dfrac{R_c}{mass\,S\,D\,C}\right]_{sample}}{\left[\dfrac{R_c}{mass\,S\,D\,C\,\rho}\right]_{std}} \tag{1.3}$$

where, ρ is the concentration in µg/g, R_c is the measured count rate, S, D and C are the corrections for saturation, decay and counting, respectively, and subscripts *sample* and

std represent the parameters for the sample and standard respectively. The advantage of using equation 1.3 follows from the theoretical definition of the activity in R_c, (see equation 1.1 and 1.2) since both standard and analyte are irradiated under identical conditions. In the standard comparator approach, uncertainty in $\phi_n(E)$ does not affect the measurements. However, preparing standards is lab-labor intensive and introduces possibilities for errors. Any error in the standards can lead to incorrect results. Moreover, the standard comparator method requires that a standard be provided for every element of interest in the sample. For large number of samples, the comparator approach can also be time consuming. Beginning in the 1960's single–comparator approaches have been developed to replace the rather cumbersome nature of the standard comparator approach [17]. In this case, a single, universal comparator standard is used for measurement of any element in a sample. However, a single-comparator approach requires good understanding of the complex neutron flux distribution $\phi_n(E)$ at the irradiation position to account for the differences in the integral in equation 1.2. Up until now, advancement in single-comparator techniques has been slow due to the limitations of the less accurate approximations used for the local neutron flux distribution. To better understand the importance of the need for a detailed flux model, the next section provides an overview of neutron transport at reactor facilities.

1.2 Neutron Transport Theory

The capability to use facilities such as the University of Missouri Research Reactor (MURR) for powerful analytic methods such as INAA and isotope production can be

optimized if a detailed knowledge of the neutron distribution is acquired. This is particularly the case in many INAA methods, where the major uncertainties are still related to imprecise knowledge of the neutron flux distribution [13, 14]. Because the total neutron distribution is impacted by the state of the system [18], it is important to carefully consider the reactor's configuration whenever measurements based on the neutron flux are made. However, due to its complexity and the fact that all reactors are different, it is very difficult to accurately study the neutron distribution experimentally. As a result, various theoretical models involving nuclear reactor systems have been developed over the years for an improved understanding of the neutron distribution [18-20].

In reactor theory, the equation of state is governed by the following mathematical relationship in order to conserve the total neutron density;

$$Source \quad - \quad Absorption \quad - \quad Leakage = \frac{\partial n}{\partial t} \, . \tag{1.4}$$

where n is the neutron density in $neutrons \bullet cm^{-3}$. Equation 1.4 implies that for a given reactor, the rate of change in the neutron density n with time ($\partial n / \partial t$), is equal to the rate of production (from the source) minus the rate of the absorbance and loss through leakage [18]. For a reactor in a steady (or equilibrium) state, the rate term on the right of equation 1.4 is equal to zero, i.e.,

$$\frac{\partial n}{\partial t} = 0 \, . \tag{1.5}$$

At steady state, equation 1.4 becomes,

$$Source \quad = \quad Absorption \quad + \quad Leakage \, . \tag{1.6}$$

Here, the neutron source comes from the fuel elements in the core, neutron *Absorption* is all of the interactions that result in the disappearance of neutrons including those that result in the production of other neutrons, and *Leakage* is neutrons escaping the system due to the reactor's finite size. For the purpose of this work, this overview will only consider the steady state condition.

Equation 1.6 is generally referred to as the critical equation [18], which can be written in a full mathematical form if expressions are derived for all three rate terms. Deriving proper rate equations for the *Source* and *Absorption* terms can be done empirically and by measurements. The leakage term on the other hand presents a challenge. The diffusion theory solution to this equation calculates neutron leakage from the reactor is based on the theory of (gaseous) diffusion, where particles will move from an area of high concentration to an area of low concentration [21, 22] . For each neutron, its trajectory defines a random motion from both elastic and inelastic scattering from different nuclides within the system. The net motion of the scattering is called the scattering mean free path [18]. Although the scattering free path is random for individual neutrons, when large amounts of neutrons are considered, there is a net movement of particles. This net motion depicts the movement of neutrons from an area of high neutron density to an area of low neutron density. Compared to gaseous diffusion, neutron diffusion can be treated quite precisely since it is reasonable to assume that the only interactions are between neutrons and the relatively fixed nuclei within the medium. This simplification is due to the fact that interactions between neutrons are extremely rare and the reaction probability with electrons is essentially zero. In any case, the statistical mechanics procedures derived by Boltzmann for gaseous diffusion can be applied to neutron transport [18, 21, 22].

In this method, a small volume element with a specific location in the system is considered. Within the element, each neutron is given an energy and a direction regardless of whether it is entering or leaving the volume element. For steady state conditions, the rate of change of the neutron density with respect to time must be equal to zero. That is, the vector sum of all neutrons entering and leaving the volume element must be zero. Mathematically, the concept leads from a complex algebraic expression known as the time-integrated Boltzmann transport equation [21, 22]. Its exact form can be expressed as

$$\iiiint_{V\,E\,0\,\Omega}^{\infty} J \bullet \nabla dVdEdtd\Omega + \rho_a \iiiint_{V\,E\,0\,\Omega}^{\infty} \sigma_T \phi dVdEdtd\Omega =$$

$$\rho_a \iiiint_{V\,E\,0\,\Omega}^{\infty} \bar{v}\sigma_f \phi dVdEdtd\Omega + \rho_a \iiiint_{V\,E\,0\,\Omega}^{\infty} (2\sigma_{n,2n} + 3\sigma_{n,3n} + \ldots)\phi dVdEdtd\Omega$$

(1.7)

where, the first term describes the total neutron leakage as the divergence [23] of the neutron current vector J in cm^2 per sec, the second term is the total neutron capture rate per second, the third term is the major component of neutron source rate in neutrons per fission per second, and the last term is the minor component of neutron source rate due to any (n, xn) reactions given as $(\sigma_{n,2n} + \sigma_{n,3n}...)$, ρ_a is the atom density, σ_T is the total absorbance cross-section, σ_f is the microscopic fission cross-section, $\bar{v}$ is the average number of prompt neutrons per fission (~2.5 for U-235), ϕ is the flux distribution and the phase-space variables of the integration are, energy E, time $t(0 \to \infty)$, direction Ω and implicitly r for position with incremental volume dV around r [24].

8

The objective of solving equation 1.7 is to use its solution to obtain detailed information about the system at steady state. For instance, one quantity that may be the most important consequence is the neutron flux at a given point per unit time, which is equal to nv. At any point, n represents the number density of neutrons with a velocity v. An exact analytical solution to equation 1.7 exactly is not possible. In the past, achieving a viable solution to the expression for the transport equation 1.7 numerically was limited by less accurate neutron cross-section data. Therefore, simpler approximations were made for the different rates terms in equation 1.7 so that an approximate solution could be achieved [18]. A simple model in reactor theory was developed called the diffusion theory approximation [18]. Here, the neutrons are considered mono-energetic (i.e., the neutron velocity is a constant). Using this approach, it has been shown that the general solution for the spatial flux distribution in $neutrons \bullet cm^{-2} \bullet s^{-1}$ for an infinite plane source in a non-multiplying medium of finite thickness (x) can be expressed as

$$\phi(x) = Ae^{-\kappa x} + Ce^{\kappa x},$$
(1.8)

where κ is the reciprocal diffusion length of the neutron in cm^{-1}, which is material dependent and A and C are constants to be determined by the boundary conditions [18]. Applying the appropriate boundary conditions, the spatial flux distribution for an infinite plane source in a non-multiplying finite medium is shown to have the form

$$\phi(x) = \frac{\sinh[\kappa(a - x)]}{\kappa D \cosh(\kappa a)} Q,$$
(1.9)

9

where a is the thickness of the medium in cm, D is the diffusion coefficient in $cm^2 \bullet s^{-1}$,

κ is again the reciprocal diffusion length in cm^{-1}, and Q is the strength of the source in

$neutrons \bullet cm^{-2} \bullet s^{-1}$ [18]. Figure 1.2 depicts an illustration of the flux distribution in a

finite non-multiplying medium from an infinite plane source.
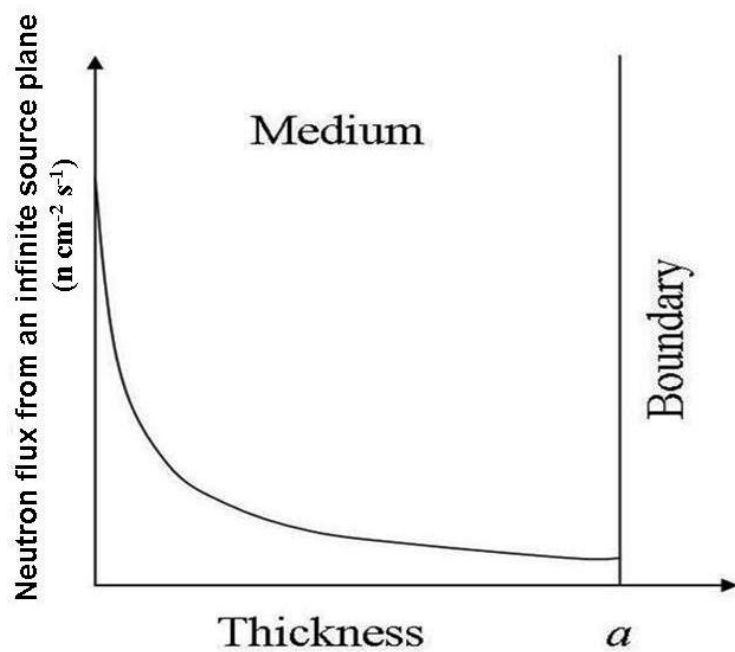
Fig. 1.2 An illustration of the spatial flux distribution in $neutrons \bullet cm^{-2} \bullet s^{-1}$ from an

infinite plane source through a finite, non-multiplying medium of thickness a in cm.

.

Clearly, this simple approach is not accurate enough to describe the flux distribution

in a real reactor system. A reactor consists of many different materials including partially

fissionable fuel material, cladding, moderator, neutron-absorbing and structural materials.

Each of these materials will transport neutrons differently. Consequently the flux

distribution in each material will be different. For instance, the flux distribution in Figure

1.2 describes mono-energetic neutrons' spatial distribution as a function of distance from

the source. In a (thermal) reactor, the neutron distribution is made up of a complex

functional distribution that depends on both distance (from the source) and neutron energies.

The spatial neutron distribution outwards from a realistic reactor core generally follows an exponential-like form as depicted in Figure 1.2 [18]. However, this is only true for the total neutron flux. When the spatial neutron distribution is separated into distinct energy groups the distributions may vary significantly [18]. Consider a simplified model of a steady state infinitely long cylindrical reactor that consists of a fuel, surrounded by a beryllium reflector and a moderator (light water). In this case, the peak thermal (low energy) neutron flux may appear in the beryllium reflector, while the peak fast (high energy) neutron flux occurs in the fuel [18]. Figure 1.3 illustrates the thermal and fast spatial flux distributions in such a case.
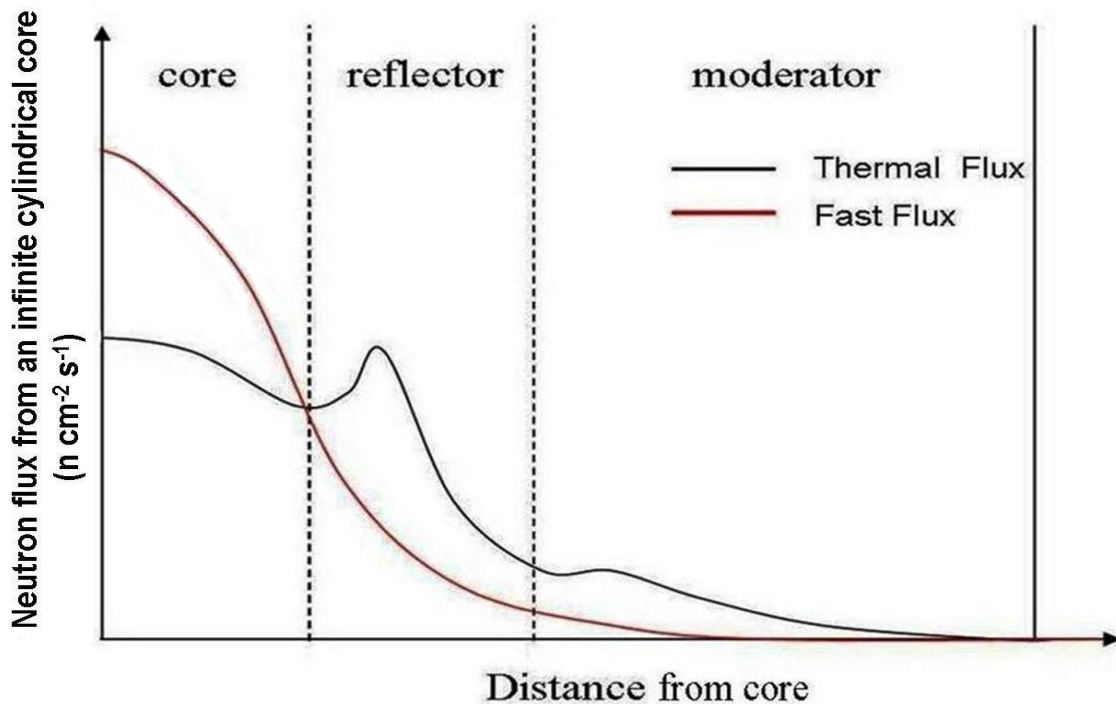
Fig. 1.3 The thermal and fast spatial flux distributions in $neutrons \bullet cm^{-2} \bullet s^{-1}$ for a simple critical reactor model as a function of distance from the core.

Considering a slice of the spatial distribution shown in Figure 1.3 along the energy axis at some distance x from the core in the moderator, the generic example of the shape of a reactor neutron flux as a function of energy is depicted in Figure 1.4.
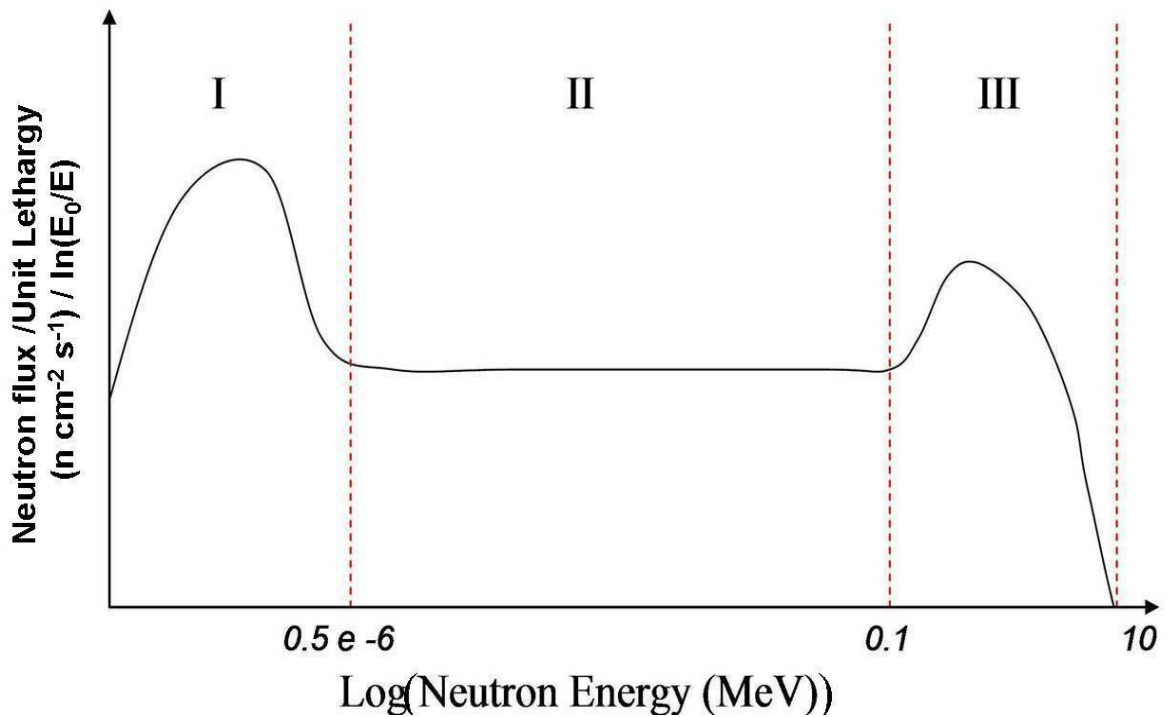
Fig. 1.4 A generic example of the neutron energy distribution at some distance x from the core (i.e., the source) in a non-multiplying medium using a unit lethargy scale.

The flux spectrum in Figure 1.4 is displayed on a unit lethargy scale which describes the logarithmic fractional decrease in energy of the neutrons. The unit is given as $\ln(E_0 / E_n)$ where E_0 is the (fission) neutron energy and E_n is the lower limit of the

neutron energy. Since most (over 90%) of the neutrons at research reactors are at thermal energies (low energy), on a normal unit energy plot, details of the intermediate and fast portions of the spectrum would be difficult to observe. Therefore, the unit lethargy scale was introduced as a convenient way to fit the full energy spectrum on one plot showing all details. Here, the spectrum can be divided into three distinct regions: Region I, which depicts the distribution of neutrons at thermal energies, Region II, which depicts the distribution of neutrons that are being moderated by non-multiplying mediums, and Region III, the distribution of neutrons that are being produced by the source.

Region I describes the behavior of neutrons at energies less than 0.5 eV (i.e., thermal energies). These neutrons are analogous to the behavior of a gas in thermal equilibrium with its surroundings. Therefore, the shape of the neutron distribution in reactors at thermal energies appears Boltzmann-like [18, 21, 22]. It has been suggested that this region is not an ideal Boltzmann distribution and may be better described by a combination of several different Boltzmann distributions [25].

Region II reflects the ideal case where neutrons between 0.5 eV and 0.1 MeV are moderated in a homogenous, non-multiplying medium. After being produced from the source, neutrons will lose their kinetic energies as $1/E_{neutron}$ until they are thermalized [18, 25]. Consequently, this portion of the spectrum appears flat on a unit lethargy scale. However, in many reactors, the overall moderating medium is a heterogeneous mix of different moderators. For example, at MURR, there are three main moderating materials, which include beryllium, light-water and graphite. Because the moderating power for each of these materials is different [18] and of neutron absorbing impurities are present

13

(particularly in beryllium and graphite) the shape of the epithermal neutron energy distribution is likely to deviate from 1/E for such reactors.

Region III generally depicts the distribution of source neutrons although not all of the neutrons come directly from fission. Source neutrons generally possess energies between 0.1 MeV and 10 MeV. The majority of these neutrons is generated as a direct result of fission; these are called prompt fission neutrons and possess an average energy of ~2 MeV and have a distribution described as a watts-fission spectrum [26]. A small portion of source neutrons is generated through their emission from unstable neutron-rich fission fragments; these are called delayed neutrons [18, 26]. An even smaller portion (less than 1%) is produced through (n, xn) and (γ, n) reactions within the fuel and materials [18, 26]. To fully understand neutron transport in reactors, it is clear that more sophisticated methods are needed to obtain a viable solution to equation 1.7 to properly describe the flux distribution in the real system. For applications in activation analysis or isotope production, a flux model that accurately describes all regions of the flux spectrum is necessary for accurate predictions.

1.3 Flux Models for Activation Applications

There are presently two prominent approaches that have been developed to address the flux distribution at the target position in INAA. In INAA, to generally reduce the uncertainties in the flux at reactors, the concentration of the analyte is determined in comparison to a well-referenced standard [13, 14]. When a standard is used for every element measured, this is referred to as the comparator method [13, 14]. In the standard

14

comparator method, each element to be determined and its standard are irradiated in identical conditions (see section 1.1). However, there are difficulties in obtaining a well-referenced comparator standard for every analyte. In addition, each multi-element measurement will require its own multi-element standard. Therefore, for elements where no suitable standards can be used for the comparator approach (e.g. for nuclides that have neutron capture cross-sections with non-1/v behavior in the thermal energy region such as lutetium and europium) problems related to the unknown flux distribution is likely to be an issue.

An alternate approach is a single-comparator parametric technique known as k_0-INAA [14, 27, 28]. In the single-comparator k_0 approach, the local neutron flux is approximated by a semi-parameterization of the local neutron energy spectrum [13, 28]. However, the approximation is still limited and is usually the main source of error. In single-comparator approaches such as k_0-INAA, the three-group approximation illustrated in Figure 1.4 of the flux spectrum is used as a basis in parameterization of the local flux spectrum. Because the contribution from the fast part of the flux spectrum to the activity is relatively small for most NAA measurements, it is usually neglected. Therefore, a two-group approximation consisting of the thermal and epithermal portions is used for practical k_0 applications. Here, the two-group flux is described as the flux ratio f, where f is defined as

$$f = \frac{\Phi_{THERMAL}}{\Phi_{EPI}} \, ,$$ (1.10)

where $\Phi_{THERMAL}$ and Φ_{EPI} represent the average thermal and epithermal flux, respectively. To account for any local deviations from the ideal *1/E* epithermal spectrum the flux-shaping factor α is introduced so that $\Phi_{EPI} \sim 1/E^{1+\alpha}$ [27, 29, 30]. The epithermal flux shaping factor *α* can be deduced from three experimental techniques, which include the bare triple probe method, the cadmium ratio multi-monitor method and the cadmium covered multi-monitor method. These methods are fully described in the work by Brockman et al. [29] and references therein. In k_0 parametric INAA, the correction factor α is expected to directly impact nuclides whose intrinsic activation rates are sensitive to the epithermal portion of the local flux spectrum or those with a high Q_0 value, such the nuclide ^{96}Zr with $Q_0 = 238$. Q_0 is defined as ratio of the resonance integral (RI) to thermal capture cross-section [28]. Here, the resonance integral is an averaging over the resonance region of the cross-section based on a $1/E_{neutron}$ epithermal energy spectrum. The general expression for RI is defined as

$$RI = \int_{0.5}^{\infty} \sigma(E) \frac{dE}{E} \tag{1.11}$$

where, $\sigma(E)$ is the energy dependent cross-section and the integration limits start from the thermal cut-off energy and extend up to 10 MeV in practical applications [31]. Figure 1.5 shows a plot of the neutron capture cross-section for ^{96}Zr.
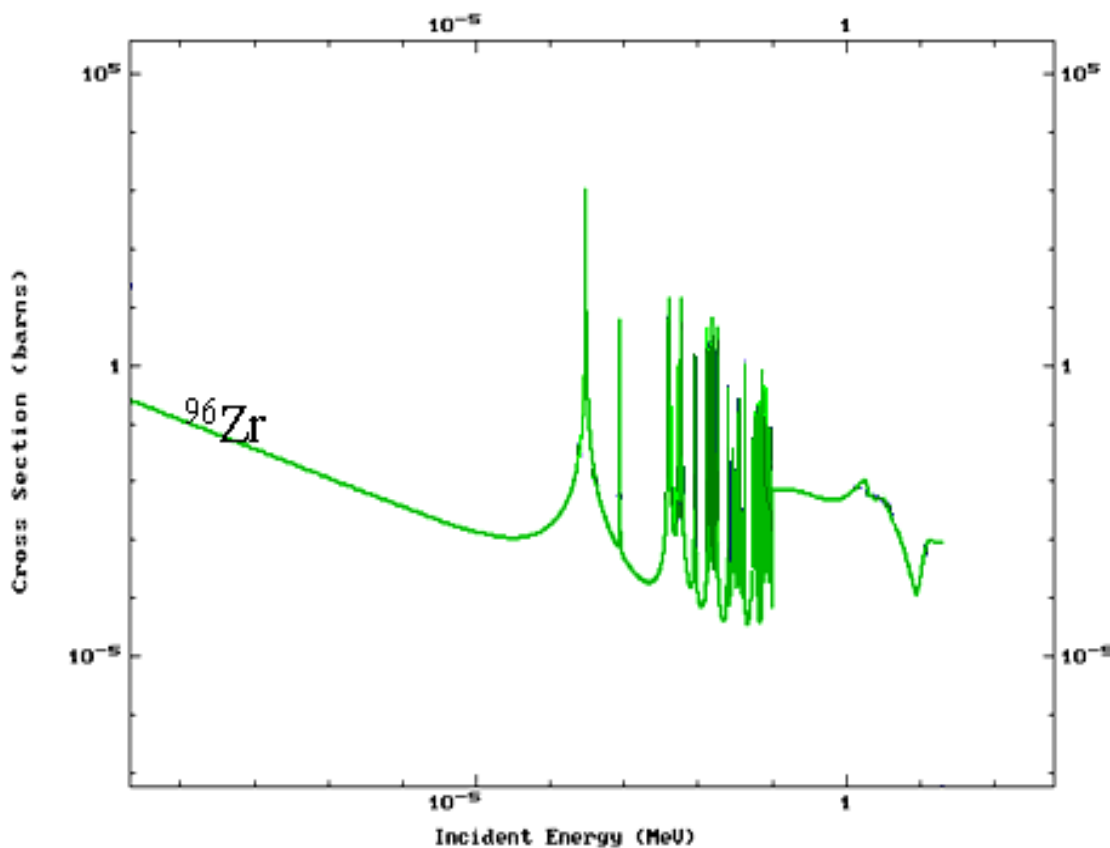
Fig. 1.5 A plot of the energy-dependent neutron capture cross-section for ^{96}Zr. In the energy region below 0.5 eV depicts the thermal capture cross-section and usually varies as 1/v. The energy region above 0.5 eV (i.e., the epithermal cross-section) shows a number of resonance peaks, the largest at 338 eV.

Naturally, in the k_0 method the RI is also modified by α. However, recent reports on using k_0 at MURR with an average epithermal flux of ~2.0 x 10^{12} n•cm^{-2}•s^{-1} showed that α had no significant impact on the measurements of high Q_0 nuclides [29]. This reveals an inadequacy of the two-group flux model at MURR. Consequently, the need to develop

a better flux model at MURR was investigated in this work for applications in single-comparator INAA.

With access to complex neutronic codes and public availability of largely improved neutron cross-section data, a numerical solution to equation 1.7 is now attainable on an ordinary personal computer. In this work, the state-of-the-art Monte Carlo N-particle transport code MCNP5 [24, 32] and the latest ENDF-B/VII.0 [33] neutron libraries are used to compute the steady-state neutron flux distribution. The objective here is to create a realistic continuous-energy flux model to predict accurate (n, γ) reaction rates for use in INAA and isotope production calculations at MURR. In this respect, the theoretical expression for the activity, in equation 1.2 can be calculated exactly. As such the work reported here is divided into two parts. Chapters 2-6 describe the development of a new approach in INAA using MCNP5, whereas Chapter 7 describes the applications of the model to isotope production of ^{99}Mo from fission. Chapter 2 describes the use of the complex particle transport code MCNP5 to compute the continuous-energy neutron flux spectrum in the irradiation channel ROW2 at MURR. The computed flux spectrum is then used to predict activation rates for parametric INAA and benchmarked against measured values.

Chapter 2 Theoretical and Experimental Methods

2.1 Theoretical Approach: The MCNP5 MURR Core Model

With the vast improvement in computing capabilities, neutron transport codes have become an essential tool for investigating the complex flux distributions in reactor systems. Some of these codes, in particular MCNP5 [24, 32], have the ability to use continuous-energy cross-section data, such as the Evaluated Nuclear Data Files (ENDF) and the Japanese-European Fusion Files (JEFF) libraries [33, 34], to model three-dimensional neutron transport through any defined material. Conveniently, these calculations can now be done on a personal computer in reasonable time. In this work, a new parametric methodology in INAA has been established using a detailed MCNP5 model of the MURR core. Here, accurate neutron capture reaction rates for many interesting nuclides are computed in ROW2 based on the detailed local flux spectrum and the continuous-energy capture cross-sections from ENDF-B/VII.0 and JEFF 3.1 neutron data libraries [33, 34]. The computed reaction rates are characterized as a new parameter π_A, where π_A is given as

$$\pi_A = \frac{r_{abs}(standard)}{r_{abs}(analyte)} \tag{2.1}$$

$r_{abs}(analyte)$ is the intrinsic reaction rate of the analyte and $r_{abs}(standard)$ is the intrinsic reaction rate of a chosen comparator nuclide. The ratio π_A scales the total flux absolutely so that it can be used as a universal parameter. The backbone of this new approach is the ability to compute the local neutron flux distributions at any irradiation position with high

accuracy using MCNP5 [24, 32]. MCNP5 is a general-purpose transport code that can selectively transport electrons, neutrons and photons in three dimensions [24, 32]. However, for this work, transporting electrons is not of significance. Therefore, the mode of transport was generally set to default to neutrons and photons only.

The code is based on a Monte Carlo method [24, 32], where source particles are randomly generated from initially sampling a well-defined source distribution. Next, the particles (with an initial energy and direction) are allowed to randomly propagate through the system. Each particle motion and survival is governed by the sum of all its macroscopic interaction cross-sections with each material within the system. A major advantage of MCNP5 over other transport methods is its ability to use continuous-energy cross-sections instead of group-wise cross-sections [24, 32, 35]. Since continuous-energy cross-sections are more precise than group-wise cross-sections, a more detailed flux spectrum can be computed. Consequently, any response function, in this case the neutron-capture reaction rate, can be tallied exactly as a continuous-energy function. Careful considerations were taken into account during the development of the model in order to compute correct flux distributions and reaction rates. In this chapter, the creation of the MURR core MCNP5 model is discussed in full detail.

To better understand the details of the MCNP5 MURR core model, a brief description of the physical core is outlined. MURR is pool-type, light-water moderated reactor with a stationary cylindrical core configuration. Its peak thermal power is 10 megawatts and it operates at full power on a 150-hour fuel cycle.
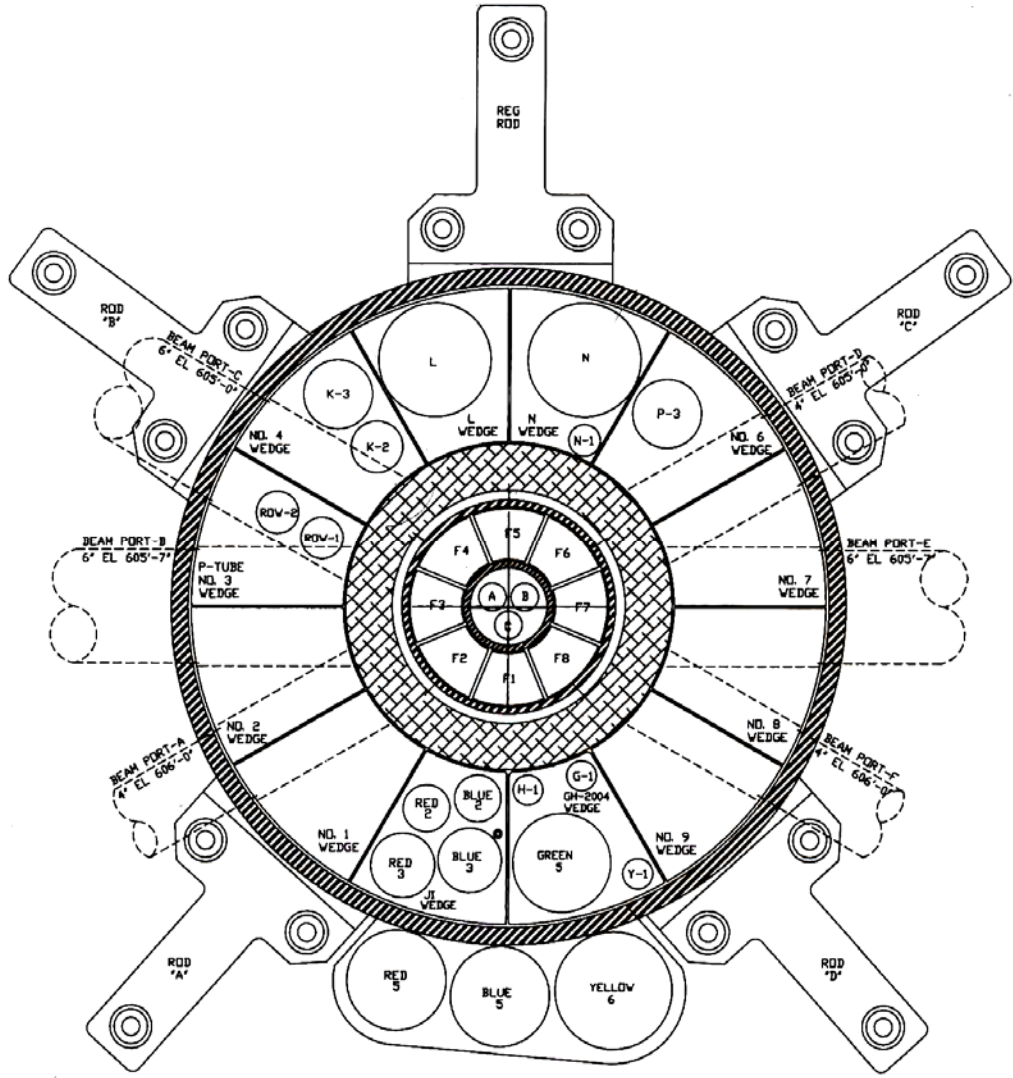
Fig. 2.1 A scaled cross-sectional schematic of the MURR core.

Figure 2.1 shows the cross-sectional view of MURR's cylindrical core design. At the center of the core is the flux trap in which there are three irradiation positions labeled A – C. The peak thermal flux within a flux trap is ~ 6.0 x 10^{14} neutrons per $cm^{-2}s^{-1}$. Surrounding the flux trap is the fuel assembly, which is made up of eight elements containing dispersion-type highly-enriched uranium (HEU) (92.3% ^{235}U) in the form of uranium-aluminide with aluminum cladding. For each cycle, the core attains criticality

21

with two fresh fuel elements and six spent or used fuel elements. The fuel assembly is contained within a 6160 – series aluminum pressure vessel and is cooled by looping pressurized light-water through the pressure vessel. The water temperature in the aluminum pressure vessel is ~ 323K.

Between the outside walls of the pressure vessel and the inner surface of the beryllium reflector, are boral control blades which maintain the core's steady state. The beryllium reflector maintains the fission chain reaction in the fuel. Outside beryllium reflector is a ring of segmented graphite reflectors. Each wedge is individually encased in customized aluminum cladding. The graphite wedge region is where the bulk of the irradiation channels and neutron beam ports are located. Many of these graphite wedges are machined to accommodate different irradiation channels and neutron beam ports. These beam ports are sometimes flooded with water or with helium depending on the application's need. The aluminum-encased graphite reflectors (and the rest of the inner-core) are located within a second 6160-series aluminum vessel. The edge of the second aluminum vessel defines the extent of the core.

The first step to create the MURR core model was to define a scaled geometrical representation of the reactor core according to precise engineering specifications. The geometrical representation of the MURR core MCNP5 model is depicted in Figure 2.2.
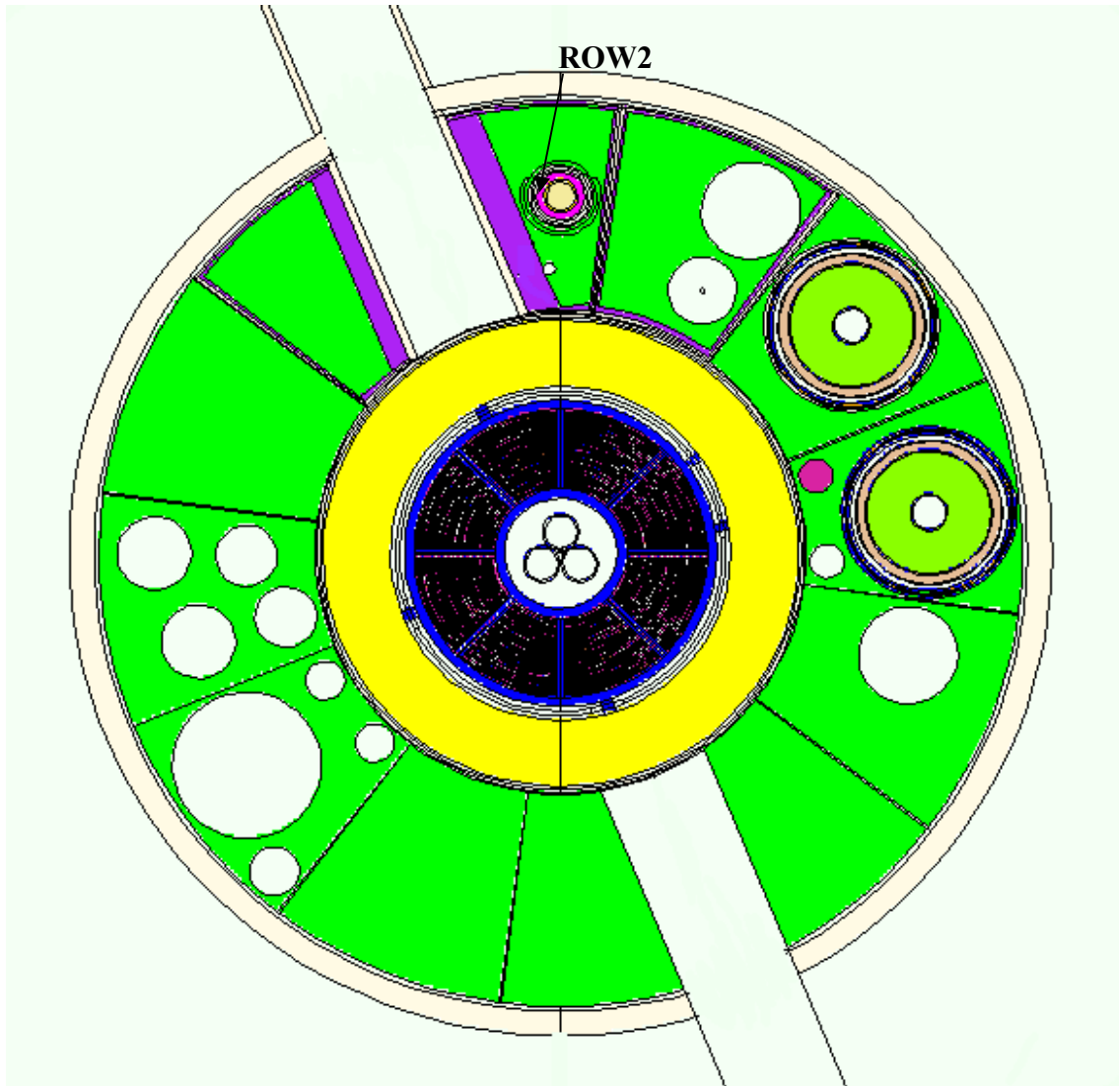
Fig. 2.2 A detailed MCNP5 model of the MURR core showing the ROW2 irradiation position. The model is rotated -60 degrees in reference to Figure 2.1. The green area represents the graphite wedge region.

The MURR core MCNP5 model was created to reflect a typical end-of-week steady-state core configuration. In the model, each material is carefully defined by considering the physical and intrinsic properties of all structural materials, fuel and moderators. In

addition, the position of the control blades and the contents of all irradiation channels and beam ports were considered. The densities, particularly for graphite, beryllium and the aluminum-dispersion fuel are specified based on documented engineering references [36-40]. The elemental compositions of each material were defined according to certification values, (see Appendix A2). For instance, the graphite wedges were modeled as nuclear grade graphite including all impurities as documented by ref [38]. Precise atomic fractions were defined for each isotope of all elements in the model. The fuel was modeled to have two fresh and six used fuel elements each at ~75% burnup based on 10MWD. Since an equilibrium core is being modeled, some burnup processes are considered in the fuel and the beryllium reflector. One such important process in the fuel is the production of the fission-product poison Xe-135. Other fission poisons are produced (e.g. Sm-151), but Xe-135 is major fission poison due to its large thermal neutron capture cross-section of 2,647,600 barns. The steady-state or equilibrium production value for the fission-poison Xe-135 can cause up to a 5% change in the total neutron flux [18]. Therefore, trace concentrations (~1.5 ppm) of Xe-135 is added to the fuel material definition to estimate its equilibrium value.

For the beryllium reflector, irradiation damage was estimated by age of the physical beryllium reflector. There are two main things that can affect the performance of the beryllium reflector: an increase in the effective absorption cross-section and a decrease in the atom density of the beryllium atoms. Due to burnup of beryllium, there is a build up of ^{6}Li, ^{3}He and ^{3}H. The nuclides ^{6}Li and ^{3}He have large thermal neutron absorbance cross-sections of $\sigma(n, t) = 940$ barns and $\sigma(n, p) = 5328$ barns, respectively. The presence of ^{6}Li and ^{3}He increases the total macroscopic absorbance cross-section of the beryllium

reflector for thermal neutrons. Since beryllium nuclei are constantly being removed and replaced by gaseous products (^{3}He and ^{3}H), the reflective and moderating (i.e., the scattering) properties of the reflector are reduced. As a result, there is a decrease in reflection of thermal neutrons and an increase in leakage of higher energy neutrons [39, 41, 42] from the reflector. One study illustrates how increased thermal neuron-capture in the beryllium reflector due to ^{6}Li, ^{3}He and ^{3}H build-up significantly affected the criticality of the MARIA multipurpose high flux research reactor [41]. Since the present beryllium reflector in the MURR core is over two years old, it was modeled at a reduced density to account for beryllium burnup. For a new beryllium reflector, the theoretical density of 1.85 g/cm^3 is used. As the reflector ages under a high neutron-flux, its density is slightly reduced. The modeled density of the beryllium reflector was obtained by estimating the total amount of Be atoms that has transmuted over the age of the reflector and taking the difference from the initial number of Be atoms. The estimated reduction in the beryllium reflector density was ~ 5%.

Next, a complete set of recently updated continuous-energy neutron cross-sections were assigned to the various nuclides present in each reactor material. These cross-section data were obtained from the publicly available JEFF 3.1 and ENDF/B-VII.0 libraries [33, 34]. For each material, the set of cross-section data includes the total neutron absorption data and fast scattering data. When the material is a moderator, a special set of thermal neutron scattering data, the S(α, β) tables [35, 43-46], are also included. Thermal neutron scattering data is essential in the models of the moderators in order to predict correct (thermal) flux distributions [32].

25

When neutrons are moderated to thermal energies, their velocities become comparable to that of the thermal motions of the atoms in the surrounding medium. The basic treatment is the thermal free gas approximation, which excludes chemical binding effects [24, 32, 35, 45, 46]. This can be best described by the Optical Model where the neutron is seen as a plane wave interacting with opaque glass spheres (the atoms) [47]. However, thermal neutrons also interact with the chemical system in the environment (i.e., the molecular bonds) within the medium. At thermal energies the neutron wavelength is large enough to interact with various rotational and vibrational states of the chemical bonds sometimes causing the creation of phonons (or excitation modes) [19, 43, 44, 48]. For materials such as graphite, silicon, bismuth or beryllium where the macro-structure can either constitute a single-crystal, poly-crystalline or even an amorphous arrangement, thermal-neutron scattering laws in each case are different [40, 49, 50]. In the MCNP5 model of MURR, the most appropriate thermal-scattering law S(α, β) is selected to correct for chemical binding effects on thermal-neutron transport in each moderator modeled.

The S(α, β) laws are a set of complex functions that are based on the momentum transfer α, and the energy transfer β, for a scattering event in the thermal energy domain [35]. However, the energy distributions of thermal neutrons and the states of the chemical bonds within the moderator are both temperature dependent. Therefore, in each moderator model, S(α, β) laws are selected with respect to the most appropriate temperature in addition to the appropriate macro-structure. There are corrected S(α, β) laws preprocessed at various temperatures in ENDF format for selected moderators including light-water, beryllium, graphite and, even recently, aluminum [33, 35, 45, 46].

26

Customized S(α, β) laws can be generated using the LEAPR and THERMR module of the complex cross-section processing code NJOY 99 [35]. However, specific details about the major vibrational modes and the frequency distribution of the moderator chemical bonds are required. These are usually obtained from ab-inito calculations.

In creating a realistic MURR core model, specific S(α, β) law temperatures were selected for light-water, beryllium and graphite. Two temperatures for light-water were modeled to account for the fact that the water temperature in the pressure vessel (i.e., the primary loop) is higher than that of the pool water (i.e., the secondary loop). In the primary loop, the water is 340K, in the model, the closest publicly available nuclear data S(α, β) laws for light-water (350K) was used from ENDF-B/VI. For water surrounding the core (i.e., the secondary loop) the average temperature is closer to 310K. However, there are no readily available S(α, β) laws for water at this temperature, therefore S(α, β) laws at 300K were used. For the beryllium reflector, the S(α, β) values for poly-crystalline beryllium metal at 300K were used. However, it is possible that the temperature of the beryllium is elevated due to neutron and gamma heating. Unfortunately, the beryllium reflector temperature cannot be readily measured during normal reactor operation. In addition, the lowest temperatures available for beryllium S(α, β) laws are limited to 293K, 300K and 400K [33]. However, it is reasonable to assume that the temperature is less than 373K since boiling does not occur in the pool water surrounding the beryllium reflector. Also, due to the fact that beryllium is an excellent thermal conductor, heat transfer to the surrounding water should be sufficient to prevent excessive elevation of the beryllium reflector temperature above 325K.

In the graphite reflector region, each wedge is thermally isolated from its aluminum casing via ceramic spacers. This is done so that the graphite is operated at a high temperature so that the stored Wigner energy is dissipated and annealing of the dislocated atoms caused by neutron bombardment takes place [36]. Unfortunately, there is also no way to readily measure the temperature of the graphite wedges at full power. Therefore, selecting the most appropriate set of publicly available $S(\alpha, \beta)$ scattering law for graphite was based on best engineering estimates in addition to annealing temperatures for poly-crystalline graphite [36, 51]. However, a recent study has reported that nuclear grade graphite is more complex than just poly-crystalline graphite [40]. It follows that there is an amorphous component to its micro-structure. The study reports that without the amorphous component, differences between $S(\alpha, \beta)$ scattering laws vary as much as 30 % for some temperatures. Unfortunately, the thermal scattering data from Ref. [40] are not publicly available and could not be obtained for use in this work. For this reason, the publicly available ENDF-B/VI $S(\alpha, \beta)$ scattering laws for poly-crystalline graphite at 600K were used in the MURR core model.

For MURR's aluminum-dispersion type HEU fuel [37] and all other materials where no publicly available or appropriate $S(\alpha, \beta)$ scattering laws are readily available, the simpler and less accurate free gas approximation [32, 35, 45] was used for their thermal neutron scattering. The thermal free gas-approximation is automated in MCNP5 once the temperature of the material is specified. Here, the fast neutron data is reconstructed at the correct temperatures from engineering specifications for the MURR core. This is especially important where there are large resonance peaks in the material cross-section, since Doppler broadening of the resonance peaks occurs as the temperature of the

material increases [32, 35]. Figure 2.3 shows a plot of the ENDF-B/VI energy-dependent fission (n, fission) cross-section for U-235 and the energy-dependent (n, γ) cross-section for U-238. In both cases, above the thermal energy region (i.e., greater then 0.5 eV) the cross-sections are dominated by large resonance peaks, each of which will be Doppler broadened as the temperature of the fuel material increases. Consequently, an increase in the fuel material temperature changes the fuel's capture-to-fission ratio, which can affect the fission rate. However, once the core is at equilibrium, the temperature of the fuel material is expected to be constant.

For engineering specifications at MURR, the average temperature of the core during steady state is less than 420K. However, the actual temperature profile of the fuel assembly will vary in correlation with the fission-rate distribution in different sections of the fuel. In the MURR core, the inner and outer edges of the fuel-assembly show larger fission rates (and higher temperatures) than the interior of the assembly. In the MCNP5 model, the fast neutron cross-sections of uranium were Doppler-broadened to reflect this temperature profile across the fuel assembly. The MCNP5 package has default sets of neutron cross-section libraries that include both fast data as well as thermal scattering neutron data. However, many of these cross-sections are outdated [24]. Therefore, new fast neutron and fission cross-sections for U-234, U-235 and U-238 from ENDF/B-VII.0 [33] were processed as a part of this work with NJOY 99 [35] into the MCNP5 usable ACE file formats.
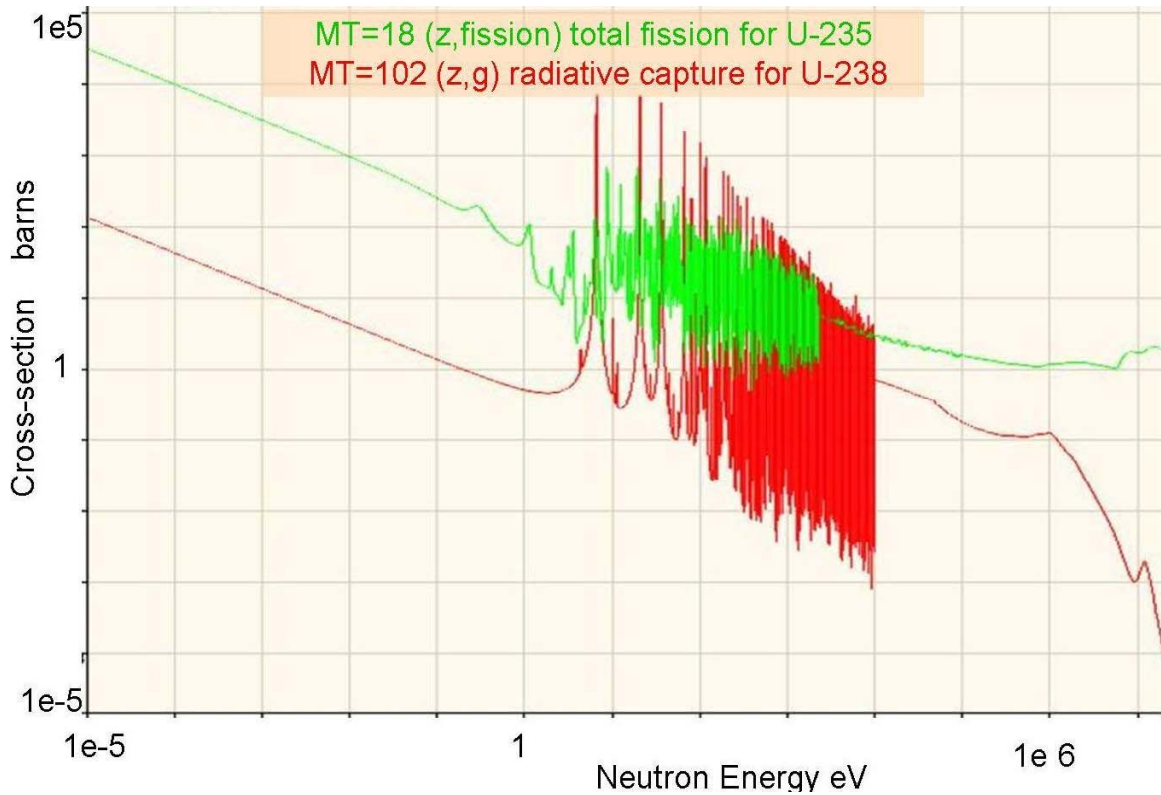
Fig. 2.3 The ENDF 6 continuous–energy microscopic total fission cross-section for [235]U (green) and capture for [238]U (red) both at 300K from ENDF 6.8. Note the large resonance peaks for [238]U above 0.5 eV.

For the rest of the model description the focus is on the graphite-wedge region of the MURR model for benchmarking purposes. As mentioned before, this region surrounds the inner core and contains the general sites for most irradiation experiments. In particular, irradiation channels ROW1 and ROW2 in graphite wedge No. 4 are two of the most frequently used irradiation sites at MURR for neutron activation analysis (see Figure 2.4). In this work, the benchmarking experiments for the MCNP5 model were performed in irradiation channel ROW2.

At MURR, targets are transported in and out of ROW2 via a pneumatic-tube transport system (PTS). All targets are always secured within a Rabbit made of high density polyethylene, which is shuttled into the irradiation position via the PTS. For this reason, it was essential to include the Rabbit as a fixed part of the MCNP5 MURR core model for the irradiation computations. The configuration of materials may change within the rabbit from time to time. However, for the benchmarking irradiations in ROW2, the Rabbit always includes a spacer made of polystyrene foam to fix the sample in its position. The panels in Figure 2.4 show the detailed cross-sectional (a), and longitudinal (b) model of ROW2 with the Rabbit and sample in the irradiation position. Panel (c) shows a photograph of a Rabbit with sample in position.

PTS

ROW2

Water gap

Rabbit with Sample

Polystyrene foam
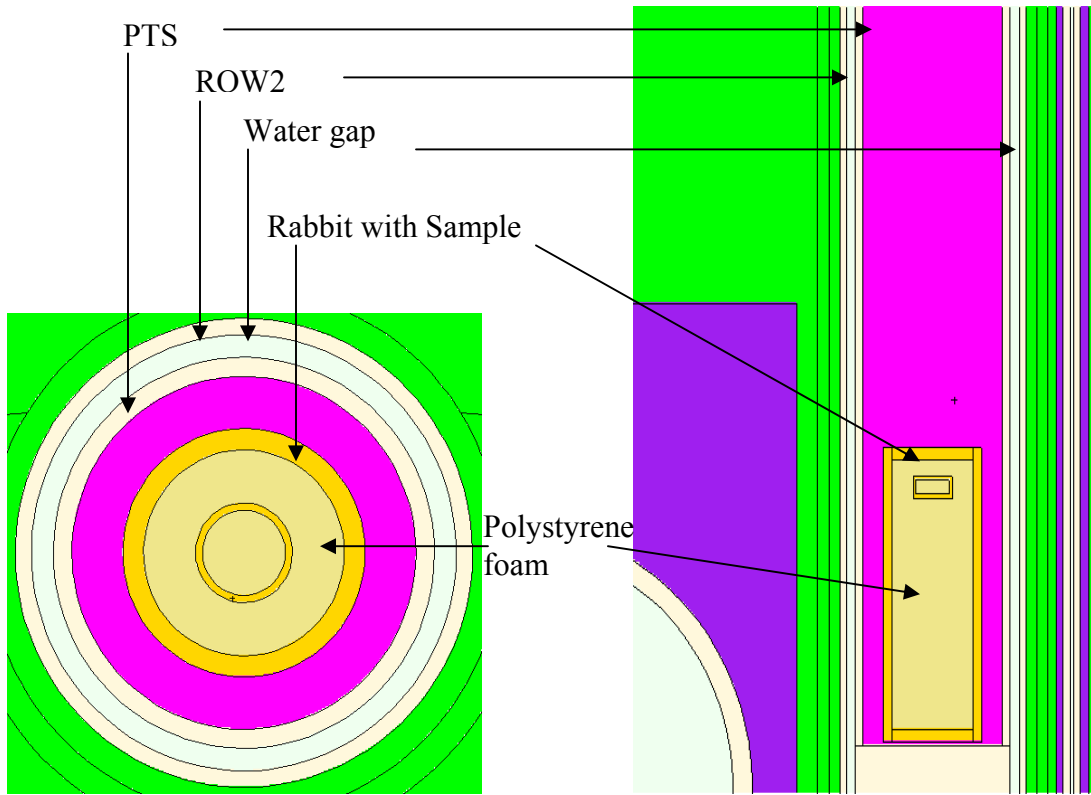
(a)

(b)

(c)

Fig. 2.4 Panels (a) and (b) show detailed sections of ROW2 and the Rabbit geometry. Panel (c) is a photograph showing the Rabbit and sample position.

High-density polyethylene (HDPE) is a hydrogenous material; therefore, its presence is expected to further thermalize the neutron flux that traverses it. In order to correctly predict the flux spectrum within the Rabbit, the appropriate thermal scattering laws were added to completely define the HDPE material in the model. There are S(α, β) laws available for polyethylene, however, the laws are only available for two temperatures, 293.6K and 350K. Although no temperature measurements were ever made for irradiated Rabbits in ROW2 at MURR, even after seven seconds of irradiation, there is enough gamma and neutron heating to raise the temperature of the rabbit well above room temperature (293.6K). One study [52] shows that temperatures rise linearly as a function of gamma dosage on polyethylene. For this reason, S(α, β) laws at 350K were used for the polyethylene Rabbit and target vials.

Finally, the height of the boral control blades is modeled to reflect the physical height in the reactor core on the day of any benchmarking measurements. Also all beam ports in the vicinity of ROW2 were checked for their status (flooded or dry) and are modeled to reflect the configuration at the time of the benchmarking measurements.

2.2 MCNP5 Criticality Calculations

For the calculations, the kcode (or criticality) mode was selected. In kcode problems, MCNP solves the neutron transport equation, (equation 1.7) by reducing the expression to an eigenvalue problem, solving for k_{eff} (the eigenvalue) and the flux distribution $\phi(E)$ (the eigen-function). This is expressed as,

$$(L + C)\phi(E) = S\phi(E) + \frac{1}{k_{eff}} M\phi(E)$$

33

where *L, C, a*nd *S* are the leakage, capture, source, respectively, and M is an arbitrary function set to one, [[24] and references therein]. Here, k_{eff} is defined as the ratio of second generation neutrons to the first generation neutrons [18].

Rearranging equation 2.1 to equation 2.2 a numerical solution is obtained by the standard power-law iterative method [32]. The transport equation is expressed as

$$\phi(E)^{n+1} = \frac{1}{k_{eff}^{n+1}} \left(\frac{M}{L+C-S} \right) \phi(E)^n \quad , \qquad (2.2b)$$

using initial approximations for k_{eff} and the flux distribution $\phi(E)$. For a criticality calculation the default initial approximation used for k_{eff} and $\phi(E)$ are 1.0000 and the watts-fission spectrum for neutrons, respectively [32]. The kcode parameters are set for 50000 neutrons to be generated each cycle, for 1000 active cycles. For a valid kcode calculation, both k_{eff} and a term that quantifies the fission-source distribution *S* must each converge. A solution for the fission source distribution is obtained in a fashion similar to k_{eff} and $\phi(E)$. A detailed discussion of *S* is provided in Ref. [32]. Once k_{eff} and $\phi(E)$ have converged, the resulting tallied flux distribution or response function is statistically consistent but not necessarily correct. In earlier less accurate MCNP5 models of the MURR core, k_{eff} converged at significantly larger values where the excess reactivity Δk_{eff}, which is defined as the difference between k_{eff} and unity, was 0.13. For the most recent equilibrium model of MURR in this work, k_{eff} converged at 1.00042

(0.00021). Figure 2.5 shows the quick convergence of k_{eff} for an MCNP5 model of an

equilibrium core at MURR.
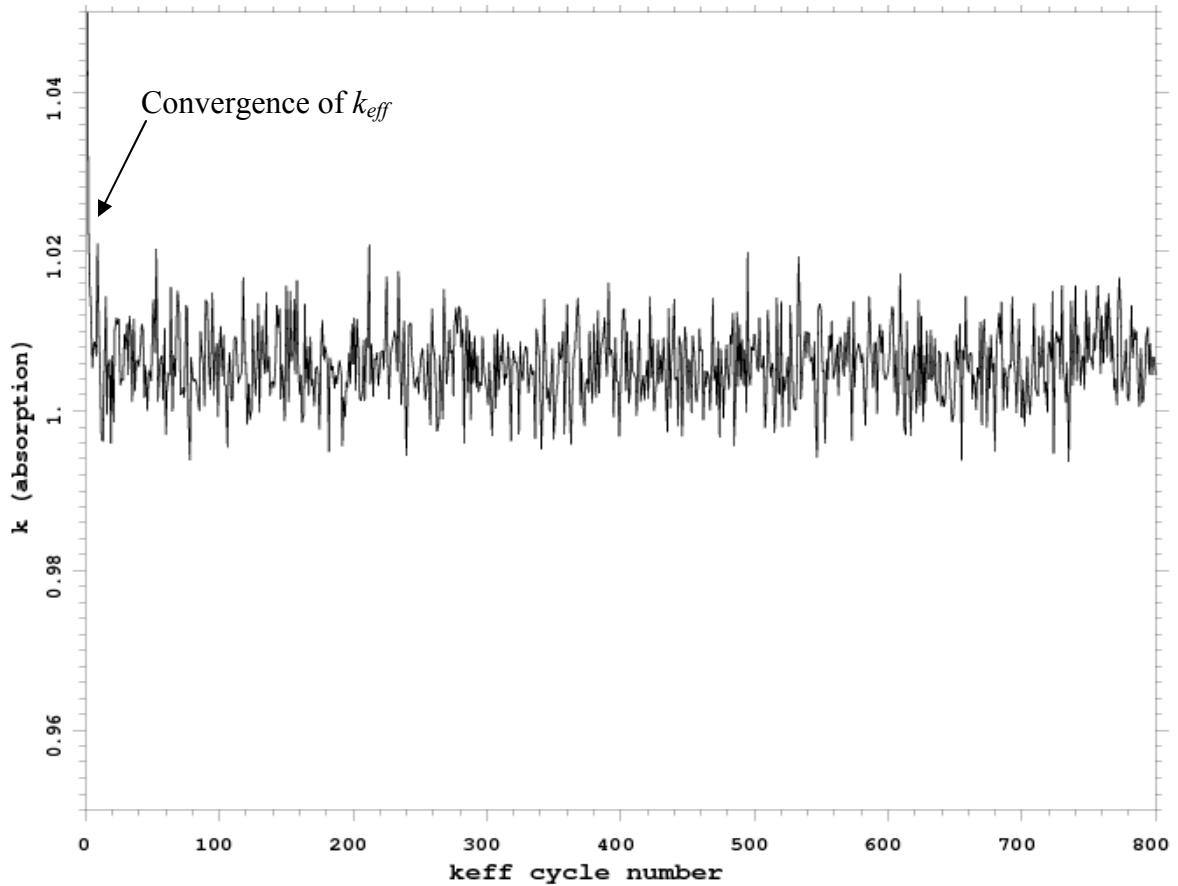
Fig. 2.5 A plot showing the quick convergence of k_{eff} based on the neutron absorption, for

the MCNP5 equilibrium core model of MURR.

In addition, the tallied flux for these earlier models over-predicted the flux in ROW2

by over 40% of the expected value. However, with increasing details in the model the

tallied flux in ROW2 approached the measured value as will be shown in Chapter 3. A

contour map of the calculated steady state total flux distribution using MCNP5 for

MURR is presented in Figure 2.6(a). The map shows a transverse section through the core centerline. The moderators' effect on the flux distribution is clearly visible in the region where there is graphite and water. The key on the right of the map shows the intensity of the neutron flux on an absolute scale. Figure 2.6(b) shows the computed steady-state flux distribution $\phi(E)$ in the target position in ROW2 on a unit lethargy scale.

(a)

Detailed Flux Spectrum Rabbit
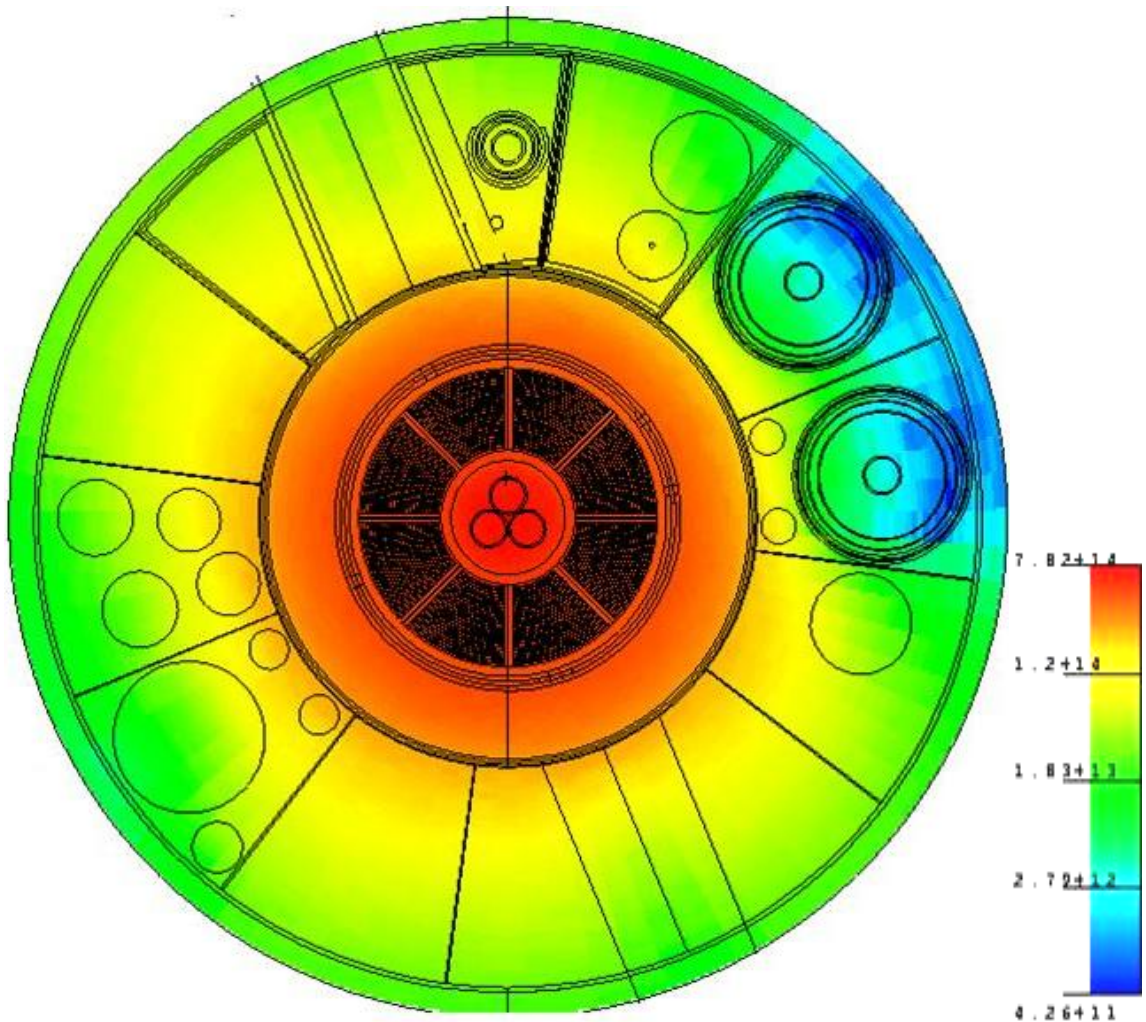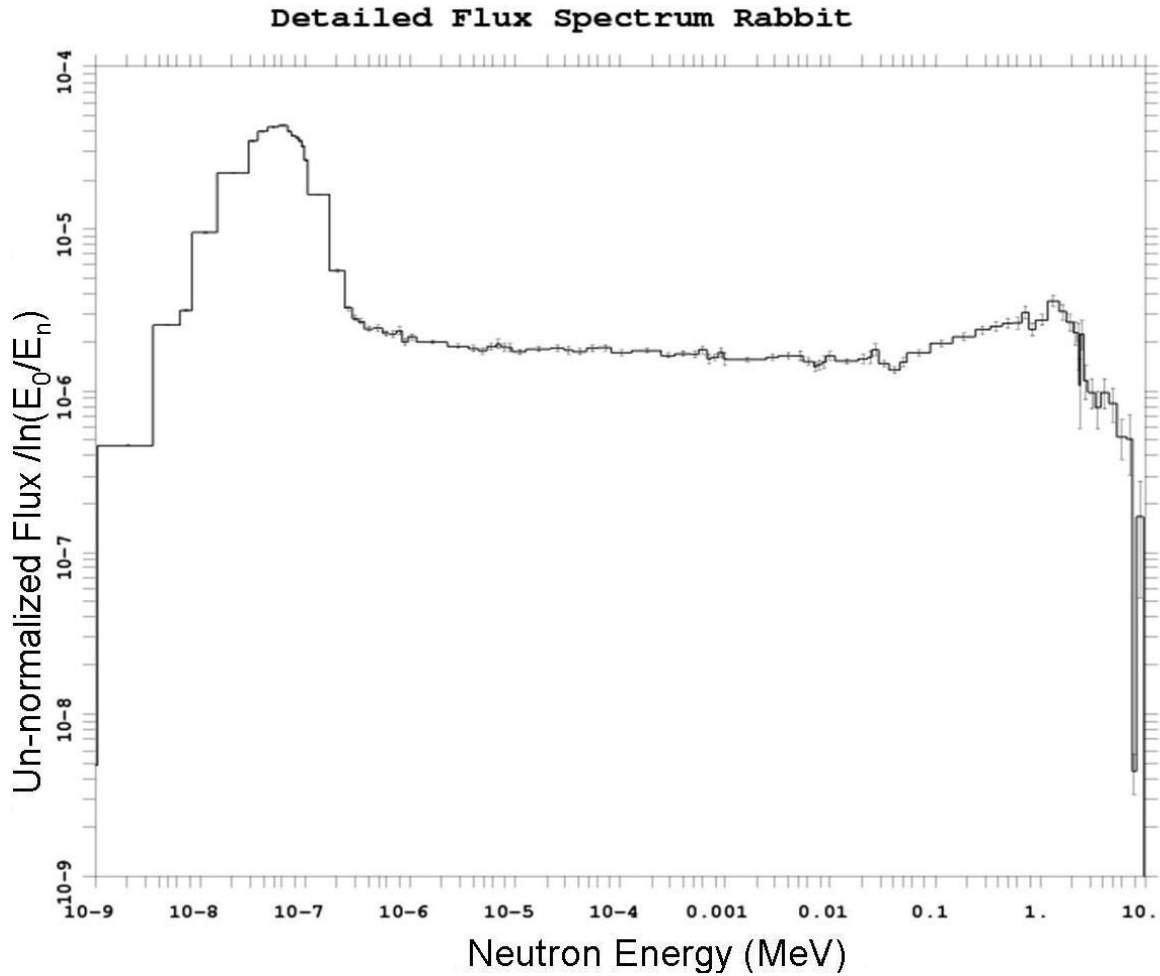
(b)

Fig. 2.6 Panel (a) shows a transverse, color-enhanced contour plot of the calculated total steady-state flux distribution through the core centerline of MURR. Panel (b) shows the un-normalized MCNP5 computed flux spectrum on a unit lethargy scale in the target position of ROW2. The fact that the epithermal portion of the spectrum in panel (b) is not flat indicates a non-ideal flux distribution in ROW2.

An important characteristic of the continuous-energy flux spectrum in Figure 2.6(b) is that the epithermal portion is not flat. In other NAA parametric models, a flux-correction

factor is used to predict the non-ideal behavior in the flux spectrum [30, 53-58]. However, a single correction factor cannot realistically account for all variations on the shape of the flux spectrum especially where the irradiation site has a complex configuration [59, 60]. In addition, Gould et al. [56] have indicated that time-variation must be considered with the use of flux correction factors such as alpha, but this may also add more uncertainty in determining a value for alpha. On the other hand, the ability of MCNP5 to accurately predict realistic continuous-energy flux distributions without the use of a flux correction factor has been benchmarked by several facilities for various applications [61-67]. One instant is reported where MCNP5 models were used to accurately study the effects of irradiating large samples for prompt-gamma NAA in ref. [65].

All response functions, including reaction rates, are tallied by MCNP5 as continuous-energy integrals. That is, any energy-dependent function can be immediately coupled to $\phi(E)$ in the form

$$F = C \int_{E1}^{E2} R(E)\phi(E)dE \quad ,$$

(2.3)

where F is any response function, C is a normalization constant, $R(E)$ can be any energy dependent function, $\phi(E)$ is the calculated flux distribution, and $E1$ and $E2$ represent the energy bins for the integration. Therefore, in the intrinsic reaction rate, r_{abs}, calculations in ROW2, $R(E)$ is the (n, γ) capture cross-section $\sigma_c(E)$ and equation 2.2 is written as

$$r_{abs} = P \int_0^\infty \sigma_c(E)\phi(E)dE \quad .$$

(2.4a)

38

Here, the constant P, is a multiplier used to normalize the reaction rate to the reactor power [32]. The value for P is determined by the following;

$$P = PWR_{thermal} \bullet \frac{1}{1.602 \times 10^{-13} \ (J/MeV) \bullet E_{fission}} \bullet \bar{v}_{fission}(s^{-1}) \bullet \frac{1 \times 10^{-24} cm^2}{1 \, barn} \qquad (2.4b)$$

where, $PWR_{thermal}$ is the steady-state thermal power of the facility in megawatts, $E_{Fission}$ is the total recoverable energy from each fission event in MeV and $\bar{v}_{fission}$ is the average number of neutrons from each fission event per second. If $PWR_{thermal}$ is measured, and literature values for $E_{Fission}$ and $\bar{v}_{fission}$ are used [18, 24, 32], a value for P can be obtained. However, $E_{Fission}$ and $\bar{v}_{fission}$ may vary for different reactor configurations such as MURR. Therefore, in this work P was obtained by the ratio of the measured intrinsic reaction rate to the un-normalized intrinsic reaction rate from the MCNP model. That is, a rearranging equation 2.4 and replacing r_{abs} with the measured value gives

$$P = \frac{r_{abs}(measured)}{\int\limits_{0}^{\infty} \phi(E)\sigma(E)\,dE} \, . \qquad (2.4c)$$

Here, the reaction rates for gold were used as gold is the established standard comparator in single comparator INAA. Gold in its natural form is mono-isotopic and its neutron capture cross-section is well documented.

For the reaction rate calculations in ROW2, a surface source (SS) [24, 32] was written around ROW2 during the kcode calculation. Initially, over 3.1 x 10^7 tracks are written to

39

the SS. However, the statistics of the SS calculations are vastly improved by increasing the number of transport histories [24, 32]. In addition, the calculation efficiency is increased since the use of SS allows for changes (including truncation) in the model's geometry everywhere except for where the surface source is defined. For the actual computations, the lower integration limit was set to 0 MeV and the upper integration limit was chosen to be 10 MeV. At 10 MeV and greater, the neutron capture cross-sections are very small (i.e., on the order of milli-barns or less) and the corresponding reaction rates are negligible.

Initially, the ROW2 irradiation position was characterized by predicting the intrinsic (n, γ) production rates of fourteen nuclides; [198]Au, [97]Zr, [66]Cu, [27]Mg, [56]Mn, ^{177}Lu, [114m]In, [69m]Zn, [99]Mo, [125m]Sn, ^{51}Cr, [79]Br, [24]Na and [51]Ti. The reaction rates of the parent nuclides are predicted within a matrix modeled as low density polystyrene foam. The matrix is included so that a realistic flux gradient is modeled through the sample to include any effects of neutron self-shielding [13, 68, 69]. The parent for each daughter nuclide listed is defined as a "dummy" material in the model so that its microscopic capture cross-section is used for tallying purposes [24, 32]. Therefore, the tallied reaction rates are based on the volume-averaged flux in the target.

The 14 benchmarking nuclides were selected based on their respective ratio of resonance integral to thermal cross-section (i.e., their Q_0 values). Nuclides such as [96]Zr are extremely sensitive to epithermal activation (a high Q_0 value), while others like [65]Cu are very insensitive to epithermal activation. The epithermal portion of the flux spectrum is expected to be very important in computing the activation rate for nuclides with high Q_0 value. Figure 2.7 (a) shows the continuous-energy capture cross-sections for [96]Zr and

40

⁶⁵Cu. The difference in epithermal and thermal neutron sensitivity between ^{96}Zr and ^{65}Cu can be observed directly in Figure 2.7 (a) by comparing the size of their resonance peaks and the magnitude of the 1/v portion of the excitation function. Figure 2.7(b) shows the computed continuous-energy reaction rates in ROW2 for ^{96}Zr (bold) and ^{65}Cu (dashed). For the ^{96}Zr reaction rate over 80% of the total reaction rate is contributed from the resonance-capture reactions. On the other hand for ^{65}Cu, over 90% of contribution to the total reaction rate is from the thermal (1/v) region.
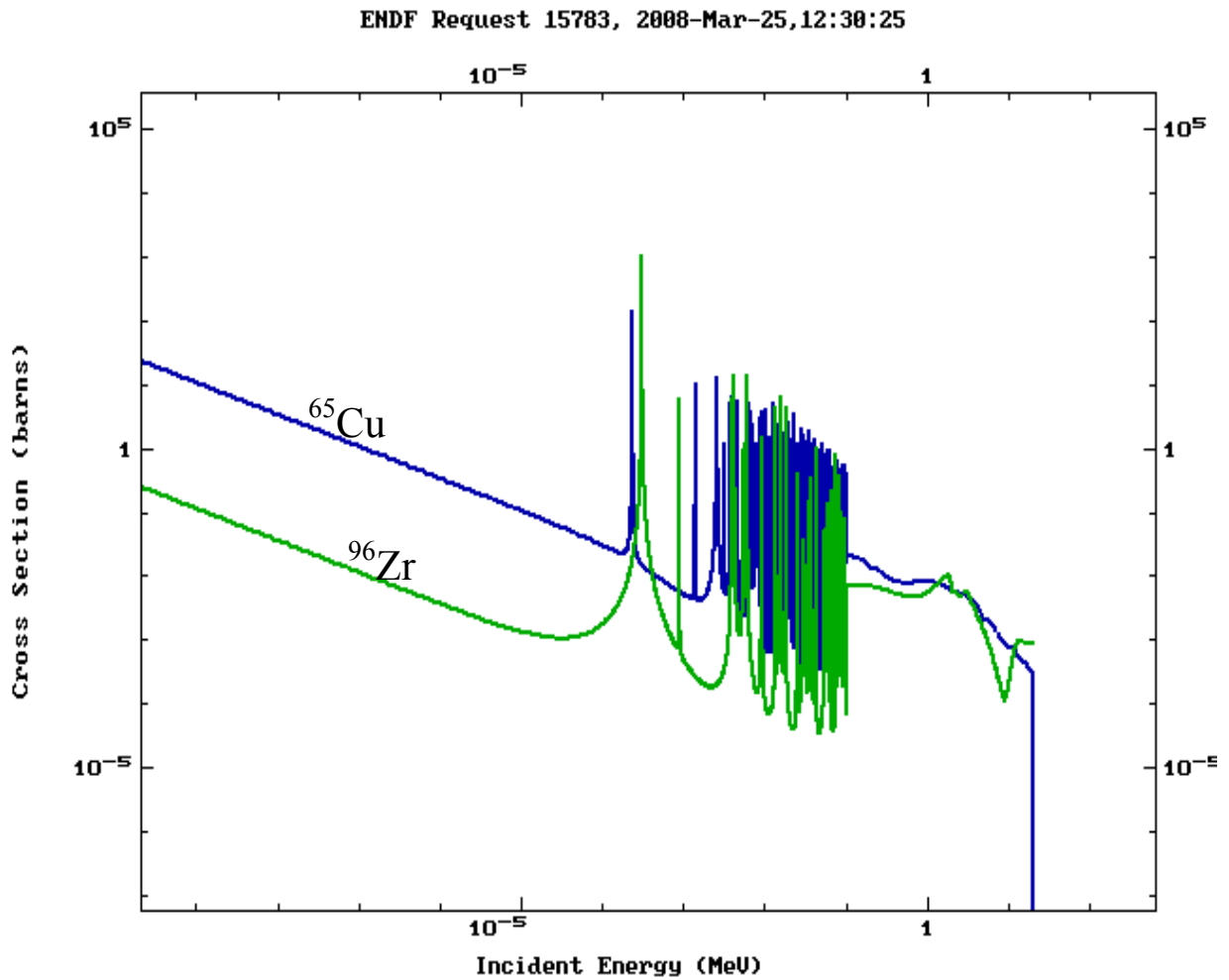
(a)
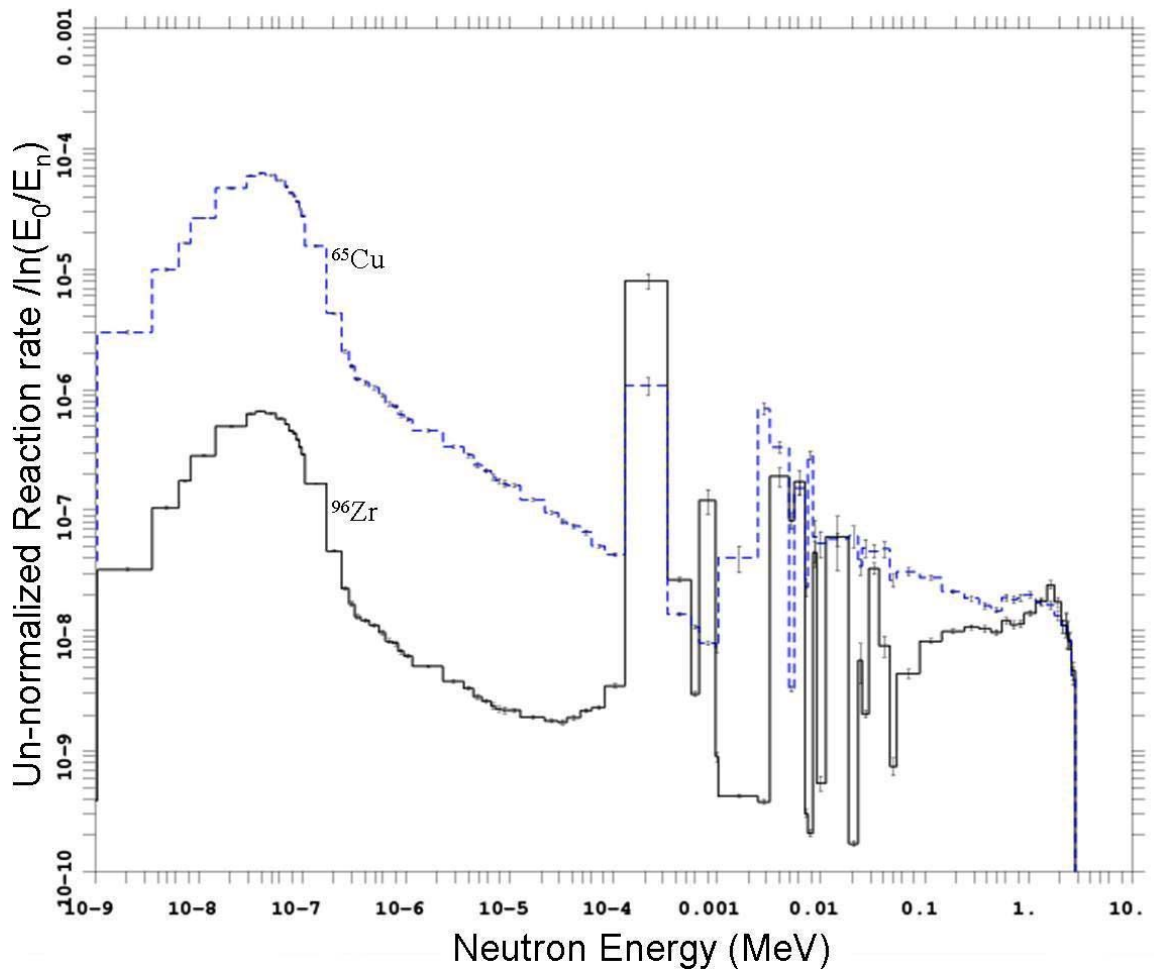
(b)

Fig. 2.7 A plot of the ENDF 6 energy-dependent capture cross-sections for ^{96}Zr and ^{65}Cu are shown in (a), while (b) shows a plot comparing the energy-dependent reaction rates for ^{96}Zr and ^{65}Cu on a lethargy scale in ROW2. Note that the ^{96}Zr the rate is almost entirely dependent on the epithermal activation while that of ^{65}Cu is almost entirely thermal activation.

The model was then used to predict (n, γ) reaction rates in organic and inorganic NIST SRMs. The materials tested were Obsidian rock SRM 278, Coal Fly Ash SRM 1633a, dried tomato leaves SRM 1573 and Bovine liver SRM 1577 [70-73]. The matrix

42

for each of these materials was modeled to contain the appropriate masses of the material's major weight-percent constituents and its boron concentration. Boron-10, in particular, has an extremely large capture cross-section for thermal neutrons (over 10^4 barns) [33, 34]. Therefore, relatively small quantities within the target can perturb the neutron flux within and surrounding a target. In recent studies [74, 75], specific experimental approaches in NAA have been described to characterize matrices with relatively high levels of strong neutron absorbers. This is taken into account by creating a detail model of the target matrix. For each model, the matrix is contained within a 250 mg HDPE vial. Again, the matrix is modeled to compute a realistic flux gradient through the sample. All selected trace elements are defined as dummy materials so that their predicted reaction rates are those calculated from the infinitely dilute capture cross-sections.

2.3 Experimental Approach

To benchmark the MCNP5 model, two sets of activation experiments were performed in the irradiation position of ROW2. In the first set of experiments, the MCNP computed reaction rates were benchmarked by measuring the flux-averaged reaction rates of a set of dilute single-element standards. Since the energy dependent neutron capture cross-sections are well-documented, the measured reaction rates should represent an indirect measurement of the average flux in ROW2 (see equation 2.2). Experimentally, the intrinsic flux-averaged reaction rate can be determined beginning with the relationship for the measured count rate given as

$$R_c = I\,\varepsilon\,A(C_{BR})$$ (2.5)

where the activity,

$$A = n_t\overline{\Phi\sigma_c}(1-e^{-\lambda t_{irr}})(e^{-\lambda t_{decay}})\left[\frac{(1-e^{-\lambda t_{count}})}{\lambda}\right].$$ (2.6)

Here, R_c is the measured count rate in cps; I is the intensity of the gamma line; ε is the efficiency of the detector; n_t is the number of target nuclei; t_{irr}, t_{decay} and t_{count} are the irradiation, decay and counting times, respectively; $\overline{\Phi}$ is the integrated neutron flux; $\overline{\sigma_c}$ is the average capture cross-section; and C_{BR} is a correction for branching decay [13]. Substituting equation 2.6 in equation 2.5, and expressing the intrinsic reaction rate as

$$r_{abs} = \overline{\Phi\sigma_c} = \int_0^\infty \sigma_c(E)\phi(E)dE\,,$$ (2.7)

equation 2.6 can be rearranged to yield r_{abs} as

$$r_{abs} = \frac{R_c}{I\varepsilon n_t(1-e^{-\lambda t_{irr}})(e^{-\lambda t_{decay}})\left[\dfrac{(1-e^{-\lambda t_{count}})}{\lambda}\right]}(C_{BR}).$$ (2.8)

The above expression can be simplified by making substitution for the saturation correction, the decay correction and the counting correction, as S D and C, respectively, where

$$S = (1-e^{-\lambda t_{irr}}),$$ (2.9)

$$D = e^{-\lambda t_{decay}}\quad\text{and}$$ (2.10)

$$C = \frac{(1-e^{-\lambda t_{count}})}{\lambda}$$ (2.11)

In the first set of benchmarking experiments, 14 elements (Au, Zr, Cu, Mg, Mn, Lu, In, Zn, Mo, Sn, Cr, Ti, Br and Na) were selected. These single-element standards were chosen to extract a range of nuclides with specific combinations of Q_0 and effective resonance energy E_{res} values. Their values were selected such that the effective resonance energy for each nuclide maps a unique region of the local flux spectrum. To calculate an external precision for the measured rates, triplicates of each single element standard were prepared. The targets were made from single-element solutions and wire standards. The solution standards were purchased from High Purity Standards at concentrations of 1000 and 10000 ppm. The zinc targets were made from 0.25 mm diameter, 99.9985% pure Zn wire purchased from Alpha Aesar [BN#NM25999]. Because gold is usually used as the conventional standard comparator, it was important for its activity measurements to be as accurate as possible. Therefore, a single sample was prepared from dilute Au-Al (0.1003%) certified flux wire from IRMM Standards [TM] to check the value of the Au solution standards. The mass of each sample was measured on the same Mettler Toledo model AX205 [S/N1122281401] high precision electronic balance. All samples were prepared such that the nuclide of interest did not exceed 100 μg in order to minimize neutron self-shielding. The single-element standards made from solution standards were contained within ¼-dram poly-vials and dried for ~24 hours. The vials were then capped and loaded in a Rabbit for irradiation. A summary of the nuclides used (as flux monitors) in the benchmarking experiments is presented in Table 2.1.

Nuclide	Q_0	E_{res} (eV)	Daughter	Elemental concentration in Matrix
[197]Au	15.1	5.5	[198]Au	1000 (3) ppm, 2% HNO_3
[176]Lu	1.27*	0.158	[177]Lu	1000 (3) ppm, 2% HNO_3
[96]Zr	248	338	[97]Zr	10000 (30) ppm, 4% HNO_3 + 2%HF
[65]Cu	1.034	766	[66]Cu	1000 (3) ppm, 2% HNO_3
[26]Mg	0.64	257000	[27]Mg	1000 (3) ppm, 2% HNO_3
[55]Mn	1.053	468	[56]Mn	1000 (3) ppm, 2% HNO_3
[98]Mo	53.1	241	[99]Mo	1000 (3) ppm, 2% HNO_3 + 0.1%HF
[124]Sn	60.1	74.2	[125m]Sn	1000 (3) ppm, 2% HNO_3 + 0.5%HF
[113]In	24.2	6.41	[114m]In	1000 (3) ppm, 2% HNO_3
[68]Zn	3.19	590	[69m]Zn	99.9985% pure Zn wire
[50]Ti	0.67	63200	[51]Ti	1000 (3) ppm, 2% HNO_3+ 0.1%HF
[50]Cr	0.53	7530	[51]Cr	1000 (3) ppm, 2% HNO_3
[79]Br	11.0	69.3	[80]Br	1000 (3) ppm
[23]Na	0.59	3380	[24]Na	1000 (3) ppm 1% HNO_3

Table 2.1 A list of nuclides selected for initial benchmarking measurements. The Q_0 and E_{res} values listed are taken from Ref. [28, 31]; * denotes the S_0 value defined as

$$S_0 = \left[\sqrt{\frac{T_n}{T_0}} Q_0 \right].$$ The certified values of the concentrations and the standard deviations are given for each single-element standard.

The samples were irradiated sequentially, on the same day for times ranging from 1 – 3 minutes accordingly. Blank ¼-dram polyethylene vials were irradiated for a background correction for those nuclides (Table 2.1) that are also present in the polyethylene vial. The reactor configuration (i.e., the control blades height and beam-port contents) was also recorded at the time of measurement for the model.

To investigate the repeatability of the benchmarking measurements, a repeated set of activation experiments was performed using a set of dilute single-element standards. Targets with relatively short half-lives (i.e., less than three days) were reused. In this case, the daughter nuclide was allowed to decay for more than 10 half-lives. Following

the first-order kinetics of the radioactive decay process after 10 half-lives, 0.1% of the original activity remains. For most nuclides listed in Table 2.1, it was feasible to reuse the original samples without interference from prior activity. However, for long-lived nuclides such as chromium-51 with a half-life of 28 days, new standards were prepared for repeated experiments.

For the next set of experiments, the objective was to benchmark the MCNP5 model's capability to predict the trace-elemental concentrations within realistic sample matrices. Here, a set of standard reference materials (SRM) from NIST were used as the realistic matrices. The set of SRMs include two geological samples, obsidian rock SRM 278 and coal fly ash SRM 1633a, and two organic samples, tomato leaves SRM 1573 and bovine liver SRM 1577. Each SRM was weighed as a two-way split-mass sample each at ~125 mg on a Mettler Toledo AX205 [S/N1122281401] high precision electronic balance. Next, a dry-matter correction was done for each sample. The irradiation targets were prepared in a ¼-dram HDPE vials and heat-sealed to secure the sample during irradiation. For each SRM, two samples were prepared for short and long irradiation times. Groups of short and long irradiation times were selected for nuclides with half-lives less than 20 hours, and long-lived nuclides for half-lives greater than 20 hours. Table 2.2 lists the details of each sample including actual masses, decay and irradiation times. Again, the reactor control blades height and beam-port contents were recorded at the time of irradiation for the model. Blank ¼ -dram polyethylene vials were irradiated accordingly to correct for activation products that are present in the polyethylene vials.

Target Type	NIST Standard	Name	Irradiation Time	Decay Time	Total Mass
SHORT	SRM 1577	Bovine liver	1 min	5 min	256.2 mg
SHORT	SRM 1573	Tomato leaves	1 min	5 min	250.3 mg
LONG	SRM 1633	Coal Fly Ash	1 hour	1 week	251.4 mg
LONG	SRM 278	Obsidian	1 hour	1 week	255.1 mg

Table 2.2 The list of SRM's and their experimental parameters

Ultimately, the intrinsic (n, γ) reaction-rates predicted by the MCNP5 model were used to determined trace-elemental concentrations within each sample. Therefore, to properly assess results of this work, a comparison was made with the results from the k_0 method under similar experimental conditions. In INAA, the k_0-parametric methodology, developed by F. De Corte et al. [27], has been widely implemented and demonstrated to produce reasonable results at many research reactor facilities [30, 76-84]. However, in recent measurements at MURR, the k_0 method has yielded inconsistent results for a number of nuclides. In addition, some reports have already questioned the feasibility of the k_0 method for certain types of nuclides, namely those with high Q_0 values [29, 85]. Again, Q_0 is defined as the ratio of the resonance integral to the thermal portion of the cross-section.

In the k_0 measurements, besides the need for the tabulated k_0 constants [28, 66, 86], the method requires a semi-parameterization of the flux spectrum [25, 30, 77, 87, 88]. Here, the epithermal flux-shaping factor α, and the thermal-to-epithermal flux ratio f must be determined to parameterize the flux spectrum. Therefore, in a separate set of measurements, four types of flux monitor materials were used to determine the k_0 reactor

calibration parameters α and f for the target position in ROW 2. In k_0, measuring α and f requires that the irradiation conditions including target geometry and reactor configuration be analogous to the conditions during irradiation of the analyte for INAA.

In the reactor calibration experiments, four different flux-wires (Au, Mn, Zr and Zn) were used. A total of eight targets, two per monitor were prepared. One set of (n=4) targets was used for bare irradiations while the other set (n=4) was used for epi-cadmium irradiations. Three standard procedures were then used to determine α and f. These procedures include the bare triple-probe (BTP), the cadmium-covered multi-monitor (CCMM) and the cadmium-covered ratio multi-monitor (CRMM) (see Ref. [[29] and references therein]). The Au targets were made from uncertified 0.125% Au in Al Reactor Flux wire from Thermo Corp. These Au targets were validated by using a 0.5 mm diameter 0.1003% certified Au in Al wire from IRMM standards [IRMM 530R]. Manganese targets were made from 2.4% Mn - Al certified wire, 0.768 mm in diameter from Thermo Corporation [Cata.No.634]. Zirconium targets were made from a certified 99.99% pure zirconium wire with a diameter of 0.127 mm from Alpha Aesar [Cata.No.00416, Lot#A14Q07].   Zinc targets were made from 0.25 mm diameter 99.9985% certified pure zinc wire from Alpha Aesar [BN#NM25999].

A set of ten pairs of cadmium covers was purchased from Sheildwerx[TM]. The manufacture specifications report each cadmium cover is 1 mm thick and has a diameter of 11.7 mm. To ensure consistency between all cadmium covers, a thickness variation experiment was done for each pair of covers. In this simple experiment, a set of 10 similar 1.55% certified Au-Cu alloy flux monitors was prepared. Each target was irradiated sequentially under a different pair of cadmium covers. The specific activity for

each flux monitor was calculated and the results were used to determine the variability in the thicknesses for each pair of cadmium covers. The results are presented in Table 2.3.

Cadmium cover	Au flux wire Mass g	Specific Act. dps/g
1	0.01219	1.60E+10
2	0.01263	1.64E+10
3	0.01218	1.57E+10
4	0.01281	1.64E+10
5	0.01512	1.60E+10
6	0.01208	1.68E+10
7	0.00959	1.68E+10
8	0.01132	1.63E+10
9	0.01079	1.60E+10
10	0.01139	1.59E+10

Table 2.3 The results for a set of cadmium cover thickness variation experiments showing the specific activities for 10 Au-Cu wire targets along with their masses.

The specific activity for cadmium cover sets 6 and 7 show significant variations when compared to the others. The RSD for all 10 samples together is 2.28%, after removing samples 6 and 7, the RSD is 1.5%. The Grubb's test for outliers at 95% confidence limit was used to analyze the gold specific activities. For this (n=10) data set, the F-critical value is 2.56. The F-values for cadmium cover sets 6 and 7 are furthest away from the rest at 1.56. However, the Grubb's test indicates that they are not outliers at the 95% confidence level. For the determination of α and f in ROW2, five flux monitors (^{198}Au, ^{55}Mn, ^{68}Zn and $^{94,\ 94}$Zr) were used. The targets were irradiated under the qualified cadmium covers for times ranging from 45 sec to 3 minutes. A different measurement of

α and *f* was made on the same day as each of the MCNP benchmarking experiments in ROW2.

For each target there is a possibility that the neutron flux may be depressed within the sample due to self-shielding or self-absorption [13]. This effect is quantified by the factor *G*, and is expressed as

$$G = \frac{\int_0^\infty \phi^*(E)\sigma_a(E)d(E)}{\int_0^\infty \phi(E)\sigma_a(E)d(E)} \tag{2.12}$$

where $\phi^*(E)$ is the real energy-dependent flux through the target, $\phi(E)$ is the unperturbed energy-dependent flux, and $\sigma_a(E)$ is the energy-dependent absorption cross-section. Neutron self-shielding is a function of sample thickness and its energy-dependent absorption cross-section [68, 69, 89]. The neutron flux will depress significantly for targets with high absorption cross-section and high atom density. Since k_0 is based on a two-group flux model, *G*-factors are calculated separately based on the thermal and epithermal portions of the flux spectrum [90, 91]. This can be done numerically by changing the upper and lower integration limits in equation 2.12 to limits which define the thermal and the epithermal regions. However, if the atom density of the target used corresponds to a mass of less than 10 μg, then the infinitely dilute cross-section is assumed and self-shielding effects are negligible. In the case for Au and Mn, the masses of Au and Mn targets were selected such that their infinitely dilute cross-sections are used. For the pure zirconium and zinc wires, thermal and epithermal *G*-factors were

computed using the MCNP5 model (see Appendix 1). The thermal G-factors were both 1.00 while the epithermal G-factors are 0.96 and 0.91 for Zr and Zn, respectively.

2.4 Counting and Detector Efficiency Calibration

After irradiation of the samples, delayed gamma ray spectroscopy [92, 93] was used to analyze all activated targets. All counting was done on two similar high-purity germanium HPGe detector systems. In the data acquisition, the energy of each characteristic gamma ray is resolved by an interactive peak-fitting program. For each resolved gamma line, the background-subtracted peak area, the FWHM, the count rate and the uncertainty are output. There are slight differences in the electronics of the two data acquisition systems. For loss-free counting (i.e., count rates that may vary over the course of time) one system (DETECTOR 2) utilizes a Westphal dead-time correction method [94] where calibrated amounts of events are added to the gamma-ray spectrum to account for the total dead time. The loss-free counting allows for accurate corrections over large changes in dead-time or short-lived activities. The other system (REAR 4) for lower count rates utilizes a Live-time correction method [95] where the preset count time is adjusted according to total dead-time period.

For the counting configuration on DETECTOR 2, a rotating sample holder was placed at distances of 8 cm (position 3) and 12 cm (position 5) from the surface of the detector. DETECTOR 2 was used for counting samples with short half-lives. Figure 2.8 shows a picture of a sample in a rotating counting position for DETECTOR 2. These positions were chosen to minimize counting geometrical effects, as well as to reduce

acquisition dead time and summing effects [13, 92, 93]. Dead times on DETECTOR 2 were less than 5% in the chosen counting positions. The count time for each sample was adjusted so that the uncertainty on counting statistics was ~ 1% or less for the peaks of interest. Although there is significant lead shielding around DETECTOR 2, for counting times greater than 5 minutes, background spectra were recorded for counting corrections.
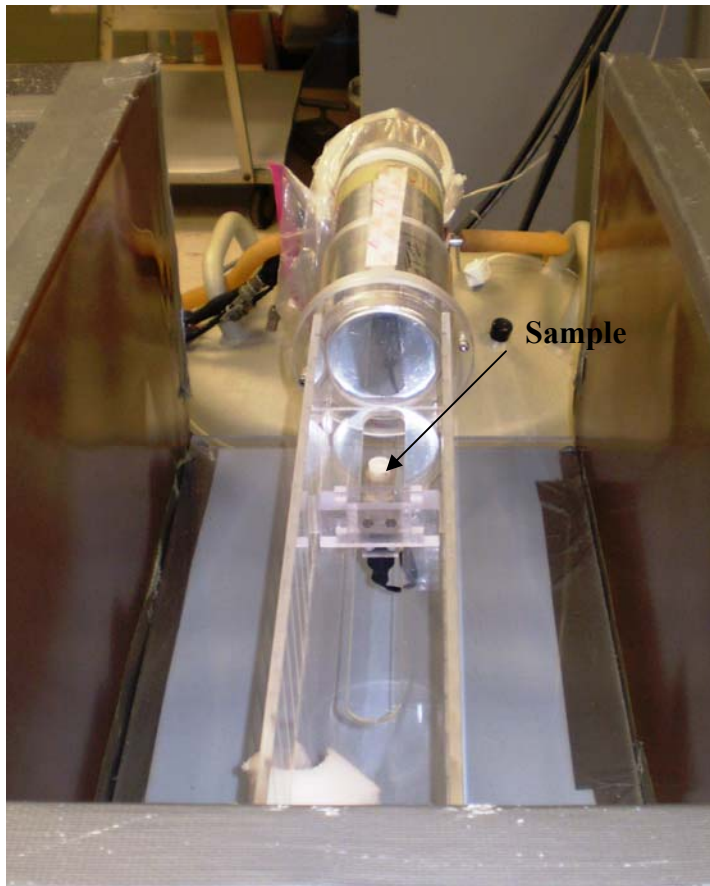
Fig. 2.8 A photograph of the HPGe setup for DETECTOR 2 showing a sample in a ¼ - dram poly vial on the rotating sample holder.

On the REAR4 system, the samples were fixed on a card sample holder and positioned 12 cm from the surface of the detector. This detector was mainly used for counting targets with long half-lives. A photo of a sample on a card holder is shown in Figure 2.9(a). Again, this position was chosen to minimize the geometrical effects of the sample while counting, as well as to reduce acquisition dead time and summing effects [13, 92, 93]. Figure 2.9(b) shows a picture of a sample in a counting position of REAR4. This photograph also reveals ample lead-shielding surrounding REAR4 to reduce background. Nonetheless, a background spectrum was recorded for possible counting corrections for samples with counting times longer than an hour. Dead times on REAR4 were less than 2%.
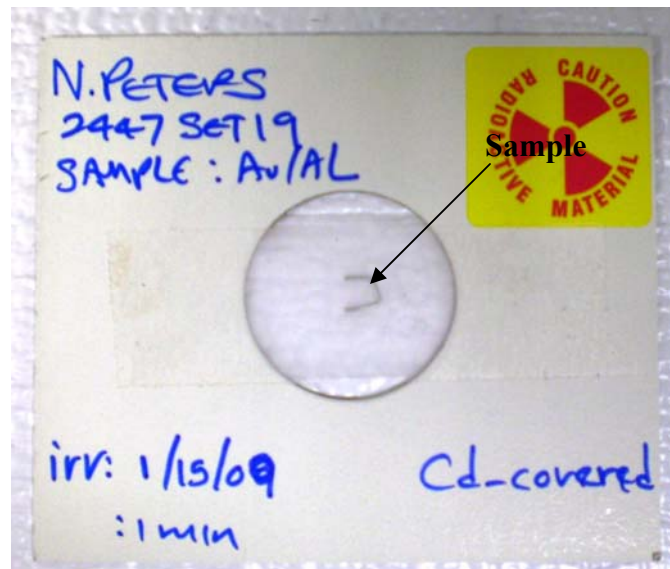
Fig. 2.9(a) A photograph of a sample source (flux wire) fixed on a card holder.

Fig. 2.9(b) A photograph of a fixed card-source holder on the REAR4 HPGe setup

The detector efficiency curves were determined separately for DETECTOR 2 and for REAR4. For this work, all efficiency curves properly calibrate gamma energies between 180 keV and 1800 keV. For DEECTOR 2, the rotating counting positions labeled 3 and 5 were calibrated using an in-house europium-152 calibration source. The geometry of the ^{152}Eu source was made similar to samples to reduce errors in the efficiency calibration. The activity of an Eu-152 point-source was checked against a calibrated ANALYTICS ^{TM} Standard Radionuclide Source [Ref.No.75645-156] point source. The difference in efficiency between the two point sources was ~ 0.6%. Figure

2.10 shows the efficiency curve of the ^{152}Eu poly vial source for the rotating position 5 on DETECTOR 2.
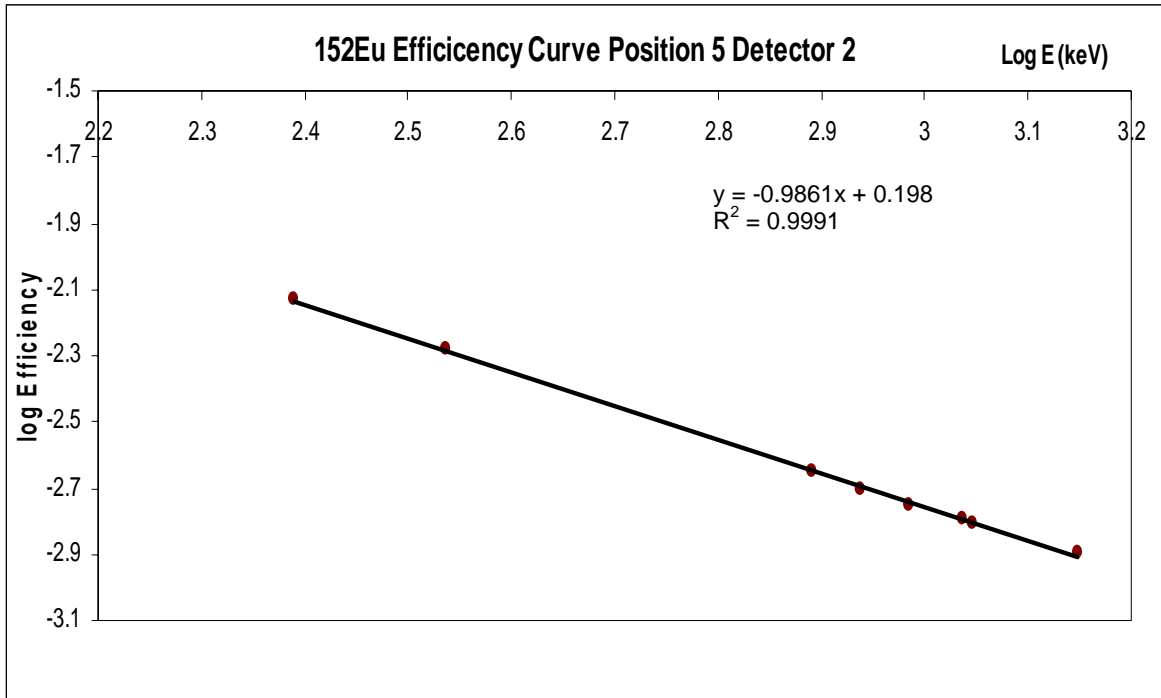
Fig. 2.10 A plot of the efficiency curve for rotating counting position 5 on DETECTOR 2 using an in-house built ^{152}Eu source.

A regression analysis was done with EXCEL for the DETECTOR 2 efficiency curve. The analysis reports a standard error on the x-variable of 1.4%

For REAR4, an efficiency calibration curve was created for counting position 5 using an ANALYTICS ^{TM} certified Standard Radionuclide point source Ref. [No.75645-156]. All samples were counted in a similar geometry. Figure 2.11 shows the efficiency calibration curve for REAR4 position 5.
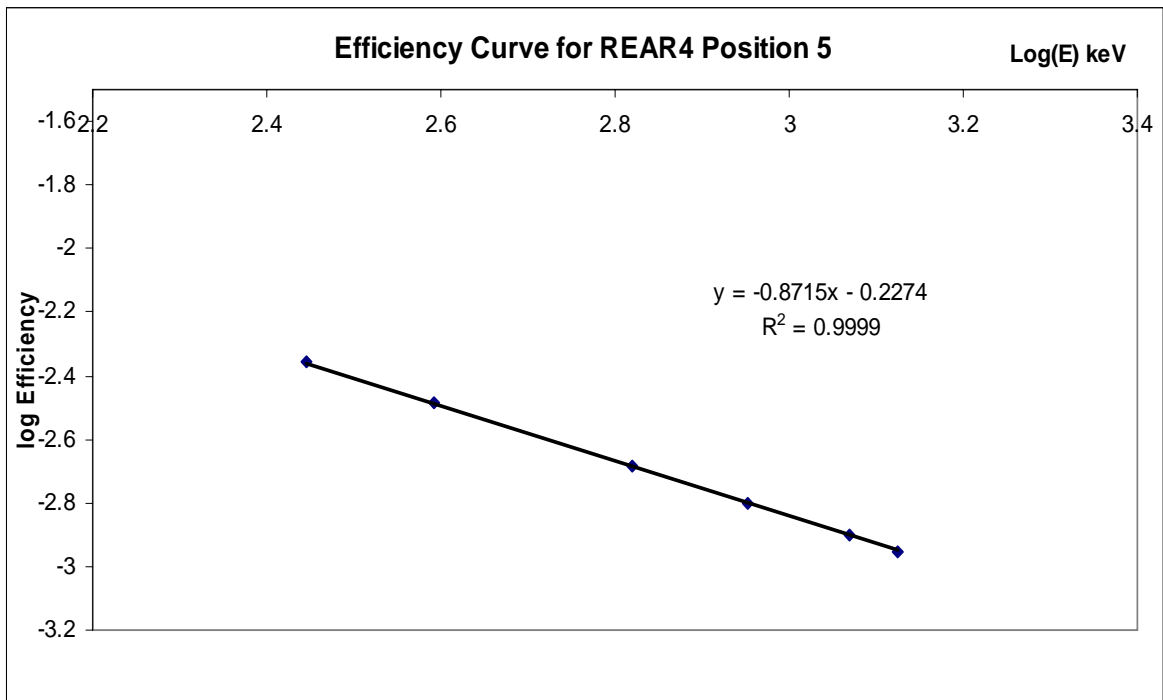
Fig. 2.11 A plot of the efficiency curve for fixed card-source position 5 on REAR4 using an ANALYTICS ^{TM} standard radionuclide source.

Similarly, a regression analysis using EXCEL for the efficiency curve in Figure 2.11 reported a standard error on the x-variable of 0.5%.

Chapter 3 MURR Core Model Benchmarking Results

3.1 Measured Reaction Rates in ROW2

In this section, the results of the intrinsic (n, γ) neutron reaction rates are presented for a set of nuclides (single-element standards) whose measurements were made in ROW2.

Nuclide	Effective resonance energy (eV)	Epithermal Sensitivity Q_0
^{197}Au	5.5	15.7
^{55}Mn	468	1.053
^{96}Zr	338	248
^{176}Lu*	0.158	1.67
^{68}Zn	590	3.19
^{65}Cu	766	1.06
^{23}Na	3380	0.59
^{26}Mg	257000	0.64
^{124}Sn	74.2	60.1
^{41}K	2960	0.97
^{98}Mo	241	53.1
^{50}Cr	7530	0.53
^{50}Ti	63200	0.67
^{113}In	6.41	24.2
^{79}Br	69.3	11

Table 3.1 Parent nuclides for which reaction rates were measured in irradiation position ROW2 for different targets. Their effective resonance energies (in eV) and Q_0 values are also listed. * denotes that there is a Westcott correction for the Q_0 value based on the temperature of the sample.

Equation 2.8 was used to deduce the reaction rates for the nuclides listed in Table 3.1 irradiated in ROW2. The mean reaction rates for the set of nuclides from the single-

element standards are presented in Table 3.2. These two sets of data represent a two-week experiment, where the reproducibility of the reaction rates determined from each single-element standard was examined.

Activated nuclide	Week 1 Measured intrinsic Reaction rate s^{-1}	RSD (n=3)	Week 2 Measured intrinsic reaction rate s^{-1}	RSD (n=3)	P-Values for Student t-test at 95% CL
^{198}Au	7.48E-09	1.61%	7.48E-09	0.49%	
^{56}Mn	7.52E-10	0.34%	7.32E-10	0.31%	0.02
^{97}Zr	7.56E-12	0.27%	7.95E-12	0.69%	
^{177}Lu	2.21E-07	1.74%	2.43E-07	0.47%	0.01
^{69m}Zn	3.67E-12	3.85%	3.84E-12	0.86%	
^{66}Cu	1.21E-10	0.52%	1.10E-10	1.07%	
^{24}Na	2.78E-11	3.59%	2.71E-11	2.81%	
^{27}Mg	2.04E-12	2.99%	2.05E-12	1.40%	
^{125m}Sn	1.82E-11	1.39%	1.77E-11	1.00%	
^{99}Mo	1.54E-11	1.74%	1.47E-11	5.82%	0.008
^{51}Cr	n/a	n/a	8.73E-10	0.88%	
^{51}Ti	n/a	n/a	9.89E-12	0.31%	
^{114m}In	7.78E-10	3.57%	8.28E-10	0.15%	
^{80}Br	5.38E-10	1.11%	5.12E-10	0.36%	0.015

Table 3.2 Week 1 (3/08/08) and week 2 (7/31/08) results of the measured reaction rates from single-element standards done on the same day of each fuel cycle. Irradiation times ranged from 1-3 mins for each sample. The calculated P-values are provided for two-sided, unequal variance student t-tests at the 95 % confidence limit that show significant differences between the two weeks.

Generally, good consistency between the two-week reaction-rate measurements is reported. This was demonstrated by a student t-test at the 95% confidence limit (EXCEL). The t-test suggests that the mean n=3 reactions rates measured in week 1 are significantly different from the mean n=3 reaction rates measured in week 2 for some nuclides (^{56}Mn, ^{24}Na, ^{79}Br and ^{177}Lu). The differences between the two-week reaction

rates could be related to the fact that the precision of the measurement is much better in the second data set. However, since each nuclide has a unique sensitivity to different regions of the flux spectrum, these differences may indicate that there are some slight variations in different regions of the local flux distribution between the two weeks. However, the largest RSD for the mean reaction rates between the two-week measurements of 6.73% observed for [66]Cu is still relatively small. Therefore, any variation in the local flux is likely to be small (i.e., within 10%). A detailed discussion on daily and weekly variations in the flux is presented in Chapter 5. In the next two sections the capability of the modified two-group and the MCNP continuous-energy flux models to predict intrinsic reaction rates are demonstrated. Here, the overall weaknesses in the two-group flux and exceptional strengths of the MCNP continuous-energy flux to predict absolute reaction rates accurately are highlighted.

3.2 Modified Two-Group Flux Model Reaction Rates in ROW2

To demonstrate the inadequacy of the modified two-group flux model that is used as a part of the k_0-parametric INAA methodology (described in Chapter 1 Section 2) at MURR, the intrinsic neutron capture reaction rates were determined using its described formulation. The basic two-group capture reaction-rate approximation is written as the expression

$$r_{abs} = \overline{[\phi\sigma_c]}_{thermal} + \overline{[\phi\sigma_c]}_{epithermal}$$
(3.1)

where r_{abs} is the intrinsic reaction rate; the second term is the integrated thermal neutron capture reaction rate and the third term is the integrated epithermal reaction rate [13]. Replacing the epithermal capture cross-section with the resonance integral I, equation 3.1 can be rewritten as

$$r_{abs} = \overline{[\phi\sigma_c]}_{thermal} + \overline{[\phi]}_{epithermal}I$$ (3.2)

The resonance integral is an average of the epithermal capture cross-sections derived from the single-level Breit-Wigner formula and is based on an ideal $1/E$ epithermal flux [13, 31]. However, for a particular irradiation site and geometry where the epithermal flux spectrum is not ideal, the value of I is modified by the flux shaping factor α in the Breit-Wigner formulation [29, 31, 76]. Rearranging equation 3.2 to include the measured flux ratio f and the epithermal flux-shaping factor α, and accounting for neutron self-shielding effects, equation 3.2 yields

$$r_{abs} = \overline{[\sigma]}_{thermal}\overline{[\phi]}_{epithermal}(G_{th}f + G_{epi}Q(\alpha))$$ (3.3)

where $Q(\alpha)$ is ratio of $I(\alpha)$ to $\overline{[\sigma_c]}_{thermal}$ (the integrated thermal capture cross-section) and G_{th} and G_{epi} are corrections for thermal and epithermal neutron self-shielding, respectively. Values for G_{th} and G_{epi} are assumed to be 1.0 (i.e., no self-shielding) for the single-element solution standards used since the target matrices are transparent to neutrons (i.e., small effective capture cross-section). For the pure single-element wire standards used, namely zinc and zirconium, the values for G_{th} and G_{epi} determined from

MCNP calculations are 0.90 for zinc and 0.96 for zirconium (see Table A1 in Appendix 1).

For nuclides with strong resonance peaks below the thermal flux region (i.e., below the cut-off energy of 0.5 eV) the modified-Westcott formalism [77, 96] is used to predict the reaction rates. The Westcott correction in k_0 accounts for nuclides where Doppler broadening of the resonance peaks in the thermal region occurs. Here, the intrinsic reaction rate using the modified Westcott method is expressed as

$$r_{abs}(Westcott) = \overline{\Phi}\,\overline{[\sigma]}_{thermal}\,(g(T_n) + \frac{1}{4f}\sqrt{\pi\mu}S_0(\alpha)) \tag{3.4}$$

$$where \quad S_0(\alpha) = \left[\sqrt{\frac{T_n}{T_0}}Q_0(\alpha)\right] \tag{3.4b}$$

Here, $\overline{\Phi}$ is the integrated thermal flux, $\overline{[\sigma]}_{thermal}$ is the integrated thermal neutron capture cross-section, $g(T_n)$ is the Westcott correction factor as a function of the neutron temperature T_n, T_0 is the reference temperature at 2200 ms^{-1}, f is the flux ratio, μ is a constant equal to 3.681 from the Westcott convention and $S_0(\alpha)$ is the Q_0 term modified by the spectral index of the neutron temperature and α [77, 96, 97].

Using the results of the bare and cadmium covered measurements for Au, Mn, Zn, and Zr flux monitor measurements, f and α were determined for the three different weeks by the three numerical methods [[29] and references therein]. The results for f and α in the irradiation position of ROW2 are presented in Table 3.3.

Exp week	BTP		CRMM		CCMM	
	f	Alpha	f	Alpha	f (gold)	Alpha
Wk1(3/08/08)	25 (0.9)	0.058 (0.01)	31.6(0.5)	0.042(0.003)	32.1(0.3)	0.048(0.003)
Wk2(7/31/08)	24 (1.1)	0.066 (0.01)	31.4(0.5)	0.024(0.003)	33(0.4)	0.036(0.002)
Wk3(1/09/09)	21 (0.8)	0.109(0.01)	33.4(0.6)	0.018(0.003)	35(0.5)	0.041(0.003)
RSD	8.9%	35.3%	3.4%	40.9%	4.4%	14.5%

Table 3.3   The three-week results for the reactor calibration parameters f and α in ROW2 using three different methods. CCMM only determines the value of α and a value for f is determined separately using the gold flux monitor only.

The RSD on the flux ratio determined by each method shows that there is small variation from week-to-week. The largest RSD at 8.9% for the mean value of f is seen for the BTP method. However, this result is consistent with previous studies [[29] and references therein] that suggest the BTP method is the least accurate of the methods. Nonetheless, the overall result for f suggests consistency in the flux spectrum for the irradiation position of ROW2. Although the values for f determined using the gold flux-monitor are slightly higher than f determined by CRMM, the values and the RSD between weeks are generally consistent. However, f does not relate to any changes in absolute flux intensity. Changes in the flux intensity are reflected in the intrinsic reaction rates. While the uncertainties that are reported for alpha are reasonable (less than 10%) the RSD for the weekly mean value of α is relatively large (i.e., between 14% - 40%). This apparent random behavior for alpha is consistent with previous measurements at MURR [29]. The results for f appear to be most consistent with cadmium-ratio multi-monitor method CRMM, which is also consistent with previous reports [[29] and

references therein]. Therefore the values f and α determined by the CRMM are used to modify the two-group flux and predict the corresponding reaction rates.

To obtain the values of $\overline{[\phi]}_{epithermal}$ and $\overline{\Phi}$, equation 2.13 is used to determined the bare and epi-cadmium intrinsic reaction rates (r_{abs}) for the flux monitors Au, Mn and Zn used in the reactor calibration (i.e., f and α) experiments. The values of r_{abs}(bare) and r_{abs}(epi-cadmium) are used to deduce the average thermal reaction rate by taking their differences expressed as

$$r_{abs}[thermal] = r_{abs}[bare] - r_{abs}[epicadmium]. \tag{3.5}$$

Using the (n, γ) cross-sections at 2200 m/s from reference [31, 98] for the various flux monitors and $r_{abs}[thermal]$, the average thermal flux can be determined from the expression

$$\overline{[\phi]}_{thermal} = \frac{r_{abs}[thermal]}{\overline{[\sigma_c]}_{thermal}} \tag{3.6}$$

Finally, the average epithermal flux is deduced by:

$$\overline{[\phi]}_{epi} = \frac{\overline{[\phi]}_{thermal}}{f} . \tag{3.7}$$

Summing equations 3.6 and 3.7, the average flux is expressed as,

$$\overline{\Phi} = \overline{[\phi]}_{epi} + \overline{[\phi]}_{thermal} \tag{3.8}$$

The values for $Q(\alpha)$ were determined from the formulation described in references [29, 31, 76]. Substituting the values of $[\overline{\phi}]_{epithermal}$, f, $[\overline{\sigma_c}]_{thermal}$ and $Q(\alpha)$ into equation 3.3, the two-group reaction rates corresponding to selected sets of nuclides from single-element standards were predicted with the exception of ^{176}Lu. For ^{176}Lu, the Westcott method was used since the effective resonance energy for ^{176}Lu is below the thermal energy cut-off (0.5 eV) at 0.158 eV. However, measuring the sample temperature during irradiation to select the appropriate Westcott g-factor is an extremely tedious task; therefore, g at 294K was chosen for the single-element standards. The values of $g(T_n = 294K)$ were taken from Ref. [96]. Next the values of $\overline{\Phi}$, $g(T_n)$, f, μ and $S_0(\alpha)$ were substituted into equation 3.4 to determine the reaction rates for ^{176}Lu.

The results in Table 3.4(a) and Table 3.4(b) correspond to reaction rates of nuclides in the set of dilute single-element standards using the values of f and α from week 1 and week 2, respectively. To better correct for the variations in the total flux distribution (power conditioning) in k_0, the *Au/x* reaction rate ratio of the two-group reaction rates is used, where *x* represents a nuclide whose reaction rate is determined. Based on the two-group flux model, the reaction rate ratio can be written as

$$\left[\frac{Au}{x}\right] = \frac{([\overline{\sigma}]_{th}(G_{th}f + G_{epi}Q(\alpha)))_{Au}}{([\overline{\sigma}]_{th}(G_{th}f + G_{epi}Q(\alpha)))_x} \tag{3.9}$$

For ^{176}Lu, the *Au/x* reaction rate ratio is expressed as

$$\left[\frac{Au}{x}\right](Westcott) = \frac{([\overline{\sigma}]_{thermal}(g(T_n) + \frac{1}{4f}\sqrt{\pi\mu}S_0(\alpha)))_{Au}}{([\overline{\sigma}]_{thermal}(g(T_n) + \frac{1}{4f}\sqrt{\pi\mu}S_0(\alpha)))_x} \qquad (3.10)$$

Activated nuclide	Two-group flux activation rate s^{-1}	Rate Ratio to gold *Au/x*	% Deviation from Measured *Au/x*
^{198}Au*	7.31E-09	1	
^{56}Mn	6.86E-10	1.06E+01	-6.7%
^{97}Zr	4.45E-12	1.64E+03	-40%
^{177}Lu	2.11E-07	3.65E-02	8.0%
^{69m}Zn	3.82E-12	1.91E+03	6.5%
^{66}Cu	5.51E-11	1.33E+02	-53%
^{24}Na	2.63E-11	2.78E+02	-3.1%
^{27}Mg	2.00E-12	3.64E+03	8.9%
^{125m}Sn	1.52E-11	4.81E+02	-10.5%
^{99}Mo	1.55E-11	4.72E+02	2.8%
^{51}Cr	7.65E-10	n/a	n/a
^{51}Ti	8.95E-12	n/a	n/a
^{114m}In	7.27E-10	8.16E+02	-4.3%
^{80}Br	5.10E-10	1.00E+01	-3.0%

Table 3.4(a) Week 1 (3/08/08) results for the reaction rates determined by the modified two-group flux model for the single element standards. A comparison to the measured rates is presented as a ratio to gold.

Activated Nuclide	Two-group flux activation rate s^{-1}	Rate Ratio to gold Au/x	% Deviation from Measured Au/x
^{198}Au*	7.25E-09	1	
^{56}Mn	6.75E-10	1.08E+01	-5.0%
^{97}Zr	4.80E-12	1.51E+03	-37.7%
^{177}Lu	2.11E-07	3.64E-02	18.2%
^{69m}Zn	3.78E-12	1.92E+03	1.6%
^{66}Cu	5.42E-11	1.34E+02	-49.0%
^{24}Na	2.58E-11	2.81E+02	-1.7%
^{27}Mg	1.97E-12	3.68E+03	1.6%
^{125m}Sn	1.57E-11	4.62E+02	-8.6%
^{99}Mo	1.61E-11	4.49E+02	13.2%
^{51}Cr	7.51E-10	9.66E+00	-11.2%
^{51}Ti	8.80E-12	8.25E+02	-8.3%
^{114m}In	7.26E-10	1.00E+01	-9.7%
^{80}Br	5.10E-10	1.42E+01	2.6%

Table 3.4(b) Week 2 (7/31/08) results for the reaction rates determined by the modified two-group flux model for the single element standards. The Au/x ratio is also listed.

While many of the modified two-group flux reaction rates show reasonable agreement for some single-element standards after taking the ratio to gold (i.e., within 10%), a number of nuclides repeatedly show a significantly large (i.e., greater than 20%) deviation from the measurements. The set of nuclides for which their production rates deviate from the measurements includes ^{66}Cu, ^{97}Zr and ^{177}Lu. The reasons for the deviations of ^{66}Cu and ^{97}Zr are not well understood. However, there are studies that report difficulties in determining consistent Q_0 values for their parent isotopes [33, 85, 99, 100]. For Lu-176, even with the Westcott correction, the two-group reaction rates still show generally large deviations from the measured rates. Poor agreement is observed for the ^{176}Lu reaction rates in the single-element target (~15%) measurements. Problems for the non-1/v nuclides may be associated with knowing the Boltzmann temperature of the neutrons in the target during irradiation. In an early study, which was done to determine

67

the neutron temperature within a lutetium target during irradiation, Lomakin et al. [101] showed that the uncertainty on the measured neutron temperature is 15 °C. In a more recent approach [102], the temperature of non-1/v nuclides was estimated by monitoring the temperature of the moderator surrounding the irradiation position. However, the temperature of the targets is still unknown.

Differences between the two-group reaction rates predicted for week 1 and week 2 are expected to be associated with the weekly variations in the values for α and f. A two-sided student t-test at the 95% confidence limit and a one-way ANOVA test (alpha '*ANOVA*' = 0.05) was done (in EXCEL) to determine whether there is a significant statistical difference between the two-group reaction rates for α and f measured in week 1 and week 2. Scores from both statistical tests suggest that there is no significant difference between the two-group reaction rates of each data set. Therefore, the large variations for the values of α between weeks appear to have no significant impact on the two-group reaction rates. Overall, the modified two-group flux approach is very complicated and it offers no resolution for many problematic nuclides even as a relative method.

3.3 Continuous-Energy Flux Model Reaction Rates in ROW2

The power of the MCNP model to predict absolute neutron-capture reaction rates with high accuracy is demonstrated in this section. The MCNP5 predictions of the intrinsic reaction rates for nuclides in the dilute single-element standards are presented in this section. Here, MCNP5 was used to create a detailed equilibrium model of the MURR core for a particular reactor configuration. The modeled configuration is consistent with the physical reactor configuration at the time of measurement. Using the criticality calculation mode, the flux distribution at the target position in ROW2 was computed. The value of P (the reactor power factor in equation 2.4c) for MURR is determined from a ratio of the mean (n=3) measured gold reaction rate to the un-normalized MCNP-computed gold reaction rate, and is equal to 7.6×10^{-7}. This value was used for all subsequent MCNP reaction-rate predictions. The intrinsic reaction-rates were then predicted by coupling the power-normalized local flux to detailed neutron capture cross-sections from ENDF-B/VII.0 and JEFF 3.1 activation libraries [33, 34], (see equation 2.3). The capture cross-sections were used at 300K for the single-element targets. The MCNP5 computed reaction rates, the mean and the RSD of the measured reaction rates over week 1 and week 2, and the relative deviation of the computed rates from the measurements are presented in Table 3.5. The RSD are not listed for ^{51}Cr and ^{51}Ti, since no data was reported for these two nuclides in week1.

Activated nuclide	MCNP5 Predicted reaction rate s^{-1}	Average 2-week measured reaction rate s^{-1} (%RSD)	Relative deviation from measurement
^{198}Au*	7.55E-09	7.48E-09(0)	0.94%
^{56}Mn	7.20E-10	7.42E-10(1.9)	-2.96%
^{97}Zr	7.93E-12	8.21E-12(4.5)	-3.41%
^{177}Lu	2.35E-07	2.32E-07(6.7)	1.29%
^{69m}Zn	3.89E-12	3.76E-12(3.2)	3.60%
^{66}Cu	1.15E-10	1.16E-10(6.7)	-0.43%
^{24}Na	2.83E-11	2.75E-11(1.8)	3.10%
^{27}Mg	2.04E-12	2.05E-12(4.0)	-0.49%
^{125m}Sn	1.79E-11	1.76E-11(1.2)	1.82%
^{99}Mo	1.51E-11	1.51E-11(3.3)	0.33%
^{51}Cr	8.47E-10	8.73E-10	-2.98%
^{51}Ti	9.84E-12	9.89E-12	-0.55%
^{114m}In	9.14E-10	8.03E-10(4.4)	11.3%
^{80}Br	6.97E-10	5.25E-10(3.5)	32.8%

Table 3.5 Results for the MCNP5 predicted reaction rates in ROW2. The computed rates are compared to the two-week average of the measured reaction rates for the set of nuclides from the dilute single-element standards.

A comparison between the MCNP5 predicted reaction rates and the mean two-week measured rates is shown in Fig 3.1. The plot shows the relative deviation of the predictions from the measured values.
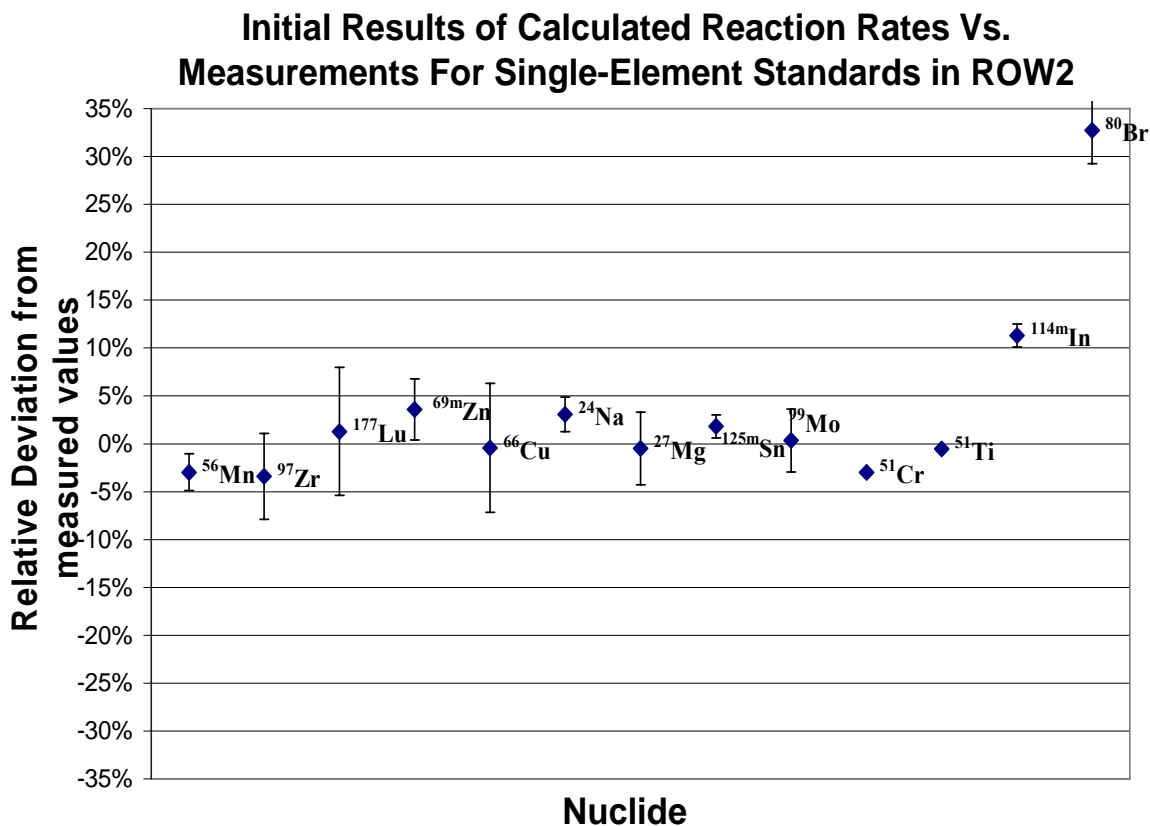
Fig. 3.1 Initial results of the comparison between the MCNP5 predicted reaction rates and the two-week average values from measured reaction rates for the single-element standards. The error bars shows the RSD for the mean of the measured reaction rates between two weeks.

With the exception of ^{114m}In and ^{80}Br, the MCNP5 predictions show excellent agreement with the measurements (i.e., within 5%). The large deviations in reaction rates for indium-113 and bromine-79 are likely to be associated with large discrepancies in the capture cross-section data. For instance, the thermal neutron capture cross-section (at 2200m/s) alone for ^{113}In from ENDF-B/VII.0 is 12.07 barns while the value used in ref. [96] is 8.42 barns. For the neutron capture reaction of ^{79}Br to ^{80}Br the thermal cross-

71

section is 11.0 barns from ENDF-B/VII.0 while the value from ref. [98] is 7.8 barns. Both discrepancies show about a 30% deviation.

The effects of important interference reactions including (n, p) and (n, α) [13, 103] on the (n, γ) reaction rates for NAA were considered. In particular, interference reactions were examined for manganese, chromium, sodium, magnesium and titanium. An approach similar to ref. [65] was employed where MCNP5 was use to calculate various interference reaction rates. The results of these calculations show that reaction rates for the interference reactions are at least two order of magnitude less than the (n, γ) rates, therefore their impact on the measurements were concluded to be negligible. In the next chapter, the reaction rates predicted from the modified two-group and the continuous-energy (MCNP5) flux models will be used separately to determine trace-elemental concentrations in the NIST SRMs from the k_0-parametric INAA and the MCNP parametric INAA, respectively.

Chapter 4 Trace-Elemental Concentration Analysis

4.1 Mass Formulas for Trace-Elemental Concentration Analysis

The respective mass formulas were used in the MCNP5 parametric method and the k_0-parametric method to determine trace-elemental concentrations for a number of elements in NIST SRMs. In this work, the predicted intrinsic (n, γ) reaction rates for a number of nuclides by each method (i.e., the MCNP parametric and k_0) involve the use of the conventional standard comparator, gold as single-comparator for INAA. For the MCNP parametric method, the mass formula can be derived beginning with the (MCNP5) predicted intrinsic reaction-rate equation (see equations 2.1 and 2.4a). The predicted reaction rate of each nuclide is ratioed to gold to yield the parameter π_{Theo} where

$$\pi_{Theo} = \frac{\displaystyle\int_{E1}^{E2} \sigma_{c(^{197}Au)}(E)\phi(E)dE}{\displaystyle\int_{E1}^{E2} \sigma_{c(analyte)}(E)\phi(E)dE} \,. \tag{4.1}$$

Using the corrected measured activities A_{meas} for gold and the element of interest, where A_{meas} is

$$A_{meas} = \frac{R_c}{I_\gamma \varepsilon SDC} \tag{4.2}$$

(see Chapter 2 Section 2.5) , the isotopic mass m_{iso} in micrograms is expressed as

$$m_{iso}(\mu g) = m_{Au} \frac{MM_{analyte} A_{meas}[analyte]}{MM_{197Au} A_{meas}[Au]} \pi_{Theo} 10^6 \tag{4.3}$$

where, m_{Au} is the mass in grams of gold in the comparator standard, $MM_{analyte}$ is the molar isotopic mass of the analyte (isotope) and MM_{Au} is the molar mass of gold.

For k_0, the (n, γ) reaction rates are based on predictions by the modified two-group flux model. Here, the flux parameters (f and α) are determined by the established cadmium ratio multi-monitor method CRMM [29] and references therein]. However, it has been shown (in Chapter 3, Section 2) that many of the (n, γ) reaction-rates predicted by the modified two-group flux model are not accurate. Even when normalized to gold the predicted rates still deviate from the measured values. Therefore, a k_0 constant whose value was determined experimentally is substituted into the k_0 mass formula to correct for the shortcomings of the flux model. For each nuclide usable in INAA, its k_0 constant(s) combines the nuclear constants (i.e., the molar mass, gamma ray intensity, isotopic abundance and thermal (n, γ) cross-section). The k_0 constant was introduced and compiled by De Corte et al. in references [86, 104] for many nuclides. There are also compilations for the theoretical values of the k_0 constants. However, there are a number of cases where the calculated k_0 values vary significantly (i.e., greater than 10%) from the measurements. Therefore, it has been recommended that the measured k_0 constants must be used for best results. Recently, Ahmed et al. (ref. [99]) reported about a number of variations in many nuclear data compilations. In particular, Ahmed et al. [99] reported that the major inconsistencies have been related to the measurements of the thermal (n, γ) cross-sections, the isotopic abundances and the gamma ray intensities for the capturing isotopes. Because of the reported inconsistencies associated with these measurements, the k_0 values compiled by De Corte et al [86, 104] are subject to variability.

Using the basic k_0 parametric approach, which is used for most nuclides, the (isotopic) mass in micrograms, is determined from the expression

$$m(\mu g) = \frac{A_{sp,analyte}}{A_{sp,Au}} \frac{1}{k_{0,Au(analyte)}} \frac{[G_{th}f + G_{epi}Q_0(\alpha)]_{Au}}{[G_{th}f + G_{epi}Q_0(\alpha)]_{analyte}} m(analyte)10^6 \qquad (4.4a)$$

where, $A_{sp,analyte}$ is the specific activity of analyte, $A_{sp,Au}$ is the specific activity of gold in the sample, $k_{0,Au(analyte)}$ is a tabulated measured constant taken from references [86, 104], G_{th} and G_{epi} are corrections for thermal and epithermal neutron self-shielding, respectively, f is the flux ratio, $Q_0(\alpha)$ is the epithermal sensitivity modified by the epithermal flux shaping factor α and $m(analyte)$ is the mass of the analyte. For elements such as Eu and Lu whose elemental concentrations are usually determined from their non-1/v nuclides ^{152}Eu and ^{176}Lu, the basic k_0 formulation is inadequate. The nuclides ^{152}Eu and ^{176}Lu both have capture cross-sections that vary significantly from 1/v in the thermal energy range ($E_n < 0.5$ eV). Therefore, equation 4.4a is modified to include the Westcott formalism [96], which is necessary for better predictions. The mass predicted using the modified Westcott method is expressed as

$$m(\mu g) = \frac{A_{sp,analyte}}{A_{sp,Au}} \frac{1}{k_{0,Au(analyte)}} \frac{[g(T_n) + 1/(4f)\sqrt{\pi\mu}S_0(\alpha)]_{Au}}{[g(T_n) + 1/(4f)\sqrt{\pi\mu}S_0(\alpha)]_{analyte}} m(analyte)10^6, \qquad (4.4b)$$

75

where, $g(T_n)$ is the Westcott correction factor as a function of the neutron temperature, f is the flux ratio, μ is a constant equal to 3.681 from the Westcott convention [96] and $S_0(\alpha)$ is the Q_0 term modified by the spectral index of the neutron temperature and α. Since no measurement of the sample temperature was taken after irradiation, the value of $g(T_n)$ at 314K is used from ref. [96]. This value was chosen to be consistent with the evaluation temperature for the ENDF-B/VII.0 and JEFF 3.1 activation cross-section used for the MCNP predictions.

For the MCNP5 parametric method, equation 4.3 is rearranged so that the elemental concentration in the sample is expressed as

$$c_{analyte}(\mu g / g) = m_{Au} \frac{MM_{analyte\ nuclide} A_{meas}[analyte]}{MM_{197\ Au} A_{meas}[Au]} \frac{1}{m_{analyte\ sample} \theta_{analyte}} \pi_{MCNP} 10^6 , \qquad (4.5)$$

where $c_{analyte}$ is concentration of the analyte (element) in the sample in ppm, $\theta_{analyte}$ is the isotopic abundance of the analyte nuclide and $m_{analyte\ sample}$ is the mass of the sample containing the analyte in grams. In the k_0-parametric method, equations 4.4a and 4.4b are modified so that elemental concentration in the sample in ppm is expressed as

$$c_{analyte}(\mu g / g) = \frac{A_{sp,analyte}}{A_{sp,Au}} \frac{1}{k_{0,Au(analyte)}} \frac{[G_{th} f + G_{epi} Q_0(\alpha)]_{Au}}{[G_{th} f + G_{epi} Q_0(\alpha)]_{analyte}} 10^6 , \qquad (4.6a)$$

and

$$c_{analyte}(\mu g / g) = \frac{A_{sp,analyte}}{A_{sp,Au}} \frac{1}{k_{0,Au(analyte)}} \frac{[g(T_n)+1/(4f)\sqrt{\pi\mu}S_0(\alpha)]_{Au}}{[g(T_n)+1/(4f)\sqrt{\pi\mu}S_0(\alpha)]_{analyte}} 10^6 \qquad (4.6b)$$

using the modified-Westcott formalism [96].

4.2 Trace-Elemental Concentrations in SRM Targets

The results of the trace-element concentration analysis for the three NIST SRM Bovine liver SRM1577 [71], Coal fly ash SRM1633 and Obsidian SRM278, using MCNP5 parametric and k_0-parametric NAA are presented. Due to large dead-times associated with the measurements of dried Tomato leaves SRM1573, no elemental concentrations were reported for this SRM. Equations 4.5, 4.6a and 4.6b were used to predict the elemental concentrations for the various NAA methods. For the non-1/v nuclides of Eu and Lu, both the standard k_0 and modified Westcott formalism were used to determine their concentrations. The standard deviations (SD) are also listed. The mean and the SD of the predicted values of the concentrations are based on the n=2 split-mass measurements of each SRM. No internal precision was calculated for either of the NAA methods. The standard deviations are based on measurements of the analyte's measured activity for each method. Therefore, a rigorous comparison cannot be done between the two NAA methods since their SD are identical. However, an indirect comparison is done by plotting the relative deviation of mean concentration determined by each, from the certified values. Table 4.1(a) lists the results for SRM278. Both methods generally show good agreement between the predicted concentrations and the certified values. The

standard deviation for the predicted concentration shows good precision between the split-mass measurements.

Nuclide	Certified conc. Mean /SD ppm	MCNP5 conc. Mean /SD ppm	Relative Deviation %	k_0 conc. Mean /SD ppm	Relative Deviation %
Lu	0.77(0.12)	0.73(0.08)	-5.4%	0.86(0.08)	11.6%
*Lu			n/a	1.65 (0.08)	115%
Yb	4.6(0.6)	4.39(0.10)	-4.6%	4.87(0.10)	5.9%
La	32(4)	32.09(0.10)	0.3%	30.42(0.10)	-4.9%
Hf	8.5(0.4)	8.56(0.15)	0.7%	8.34(0.15)	-1.9%
Sb	1.79(0.21)	1.84(0.05)	2.9%	1.69(0.05)	-3.5%
Cs	5.2(0.2)	5.26(0.10)	1.2%	5.01(0.10)	-3.6%
Tb	1.06(0.14)	1.03(0.04)	-2.7%	0.96(0.04)	-9.3%
Sc	4.8(0.8)	4.90(0.13)	2.1%	4.91(0.13)	5.0%
Ta	1.29(0.08)	1.25(0.06)	-3.5%	1.27(0.06)	-3.3%
Eu	0.78(0.03)	0.81(0.40)	3.5%	0.60(0.4)	-22.7%
*Eu			n/a	0.57(0.4)	-27%
Rb	133(6)	133.54(4)	0.4%	127.32(4)	-6.7%

Table 4.1(a) List of certified and predicted concentrations (using k_0 and MCNP) in ppm for SRM278. The standard deviation is also provided as error bars. The relative deviations from the certified values for each method are given as a percentage. * denotes the results from the non-1/v nuclides using k_0 without the Westcott correction.

A plot of the relative deviation of the predicted concentrations from the certified values is presented in Figure 4.1(a). The mean deviation of the MCNP5 predicted concentration is shown as the solid blue diamonds, while the mean deviation for the k_0 methods is shown as the green dots. The RSD for the certified values are shown as the red error bars. The magnitude of the RSD on the predicted values is shown as the black error bars. The MCNP5 parametric method shows that for all of the elements reported, the mean of the predicted concentration is well within ~5% of certified values including

the predictions from non-1/v nuclides. The reported values are well within the standard deviations of the certified values. Reasonable results (i.e., within ~10%) are observed for the trace-elemental concentrations predicted by k_0 with the exception of Eu and Lu. Even with the modified Westcott method, k_0 results for Eu and Lu still largely deviate from the certified values. For this SRM, the MCNP method shows better agreement with the certified values for a greater number of elements in comparison to the k_0 method.

Relative Deviation of predicted elemental concentrations from the certified values for NIST SRM278 Obsidian Rock
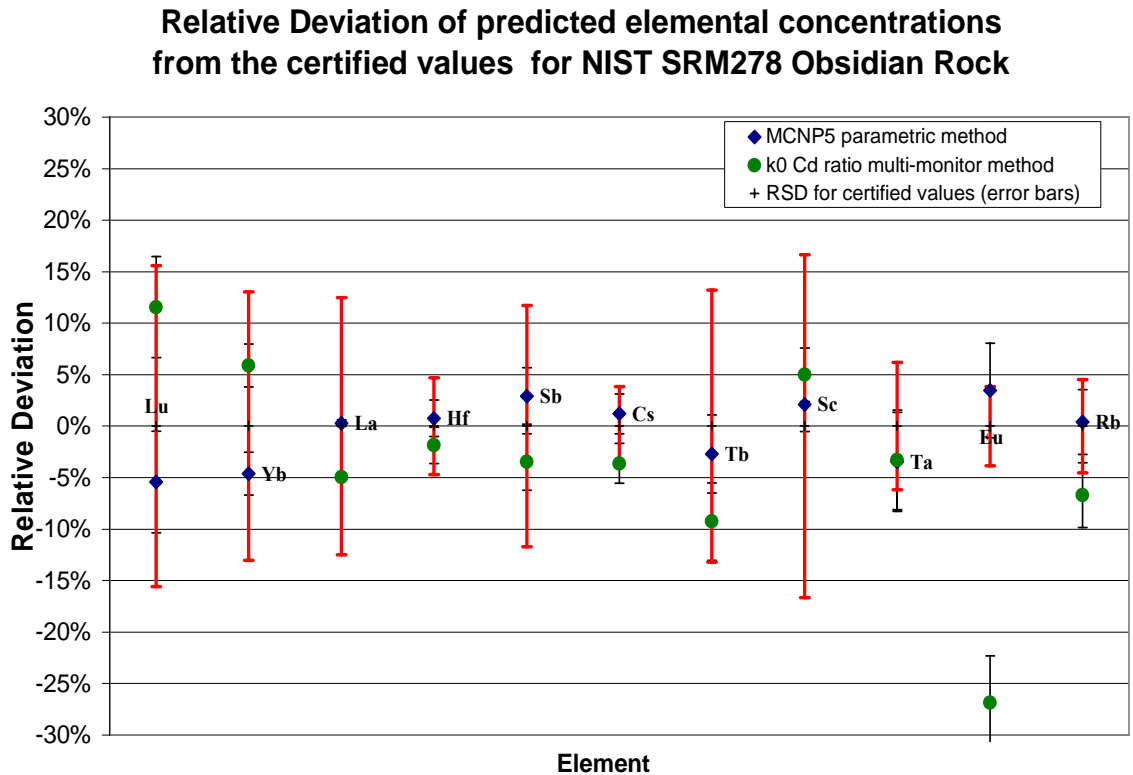
Fig. 4.1(a) A plot showing the deviation of the elemental concentrations predicted by the k_0 method (full circles) and the MCNP5 parametric method (diamonds) from the certified values for SRM278 with error bars. The crosses with errors bars (about 0 %) are the RSD for the certified values.

Results for the certified and predicted mean elemental concentrations in SRM1633 are listed in Table 4.1(b) along with their standard deviations. The list of elements is similar to those of SRM278 with the addition of Ba and Cr. The standard deviations for the predicted concentrations indicate reasonably good precision for the mean n=2 (split-mass) measurements.

Element	Certified conc. Mean /SD ppm	MCNP5 conc. Mean /SD ppm	Relative Deviation %	k_0 conc. Mean /SD ppm	Relative Deviation %
Lu	1.075(0.013)	0.73(0.08)	8.2%	0.86(0.08)	27.7%
*Lu			n/a	2.64 (0.08)	128%
Cr	196(6)	185.11(2.4)	-5.6%	201.70(2.4)	2.9%
Ba	1320(40)	1326.37(8.8)	0.5%	1430.62(8.8)	8.4%
Yb	7.5(0.13)	7.01(0.07)	-6.6%	7.78(0.07)	3.7%
La	79.1(0.8)	80.86(1.7)	2.2%	76.64(1.7)	-3.1%
Hf	7.29(0.22)	7.23(0.1)	-0.8%	7.05(0.1)	-3.3%
Sb	6.8(0.4)	6.96(0.18)	2.3%	6.36(0.18)	-6.5%
Cs	10.42(0.23)	9.97(0.51)	-4.3%	9.49(0.51)	-8.9%
Tb	2.53(0.04)	2.57(0.15)	1.8%	2.63(0.15)	4.0%
Sc	38.6(1.1)	36.42(1.4)	-5.6%	37.46(1.4)	-2.9%
Ta	1.93(0.07)	1.78(0.09)	-7.8%	1.76(0.09)	-8.7%
Eu	3.58(0.07)	3.44(0.02)	-3.9%	2.57(0.02)	-28.2%
*Eu			n/a	2.44 (0.02)	-32%
Rb	131(2)	137.27(3.8)	4.8%	127.53(3.8)	-2.6%

Table 4.1(b) List of certified and predicted concentrations (using k_0 and MCNP) in ppm for SRM1633. The standard deviation is also provided as error bars. The relative deviations from the certified values for each method are given as a percentage. * denotes the results from the non-1/v nuclides using k_0 without the Westcott correction.

A plot of the relative deviation between the certified values and predicted values for SRM278 for each method is shown in Figure 4.1(b). Results of both methods are generally consistent with the certified values for most elements. In particular, the MCNP5

method shows agreement with mean relative deviation of ~5% from the certified values for the reported elements. In comparison to the k_0 method, the MCNP parametric method shows better agreement with the certified values for a greater number of elements. For the k_0 predictions, the two problematic elements are again Lu and Eu, with relative deviations of 15% and 20%, respectively using the modified Westcott formalism.
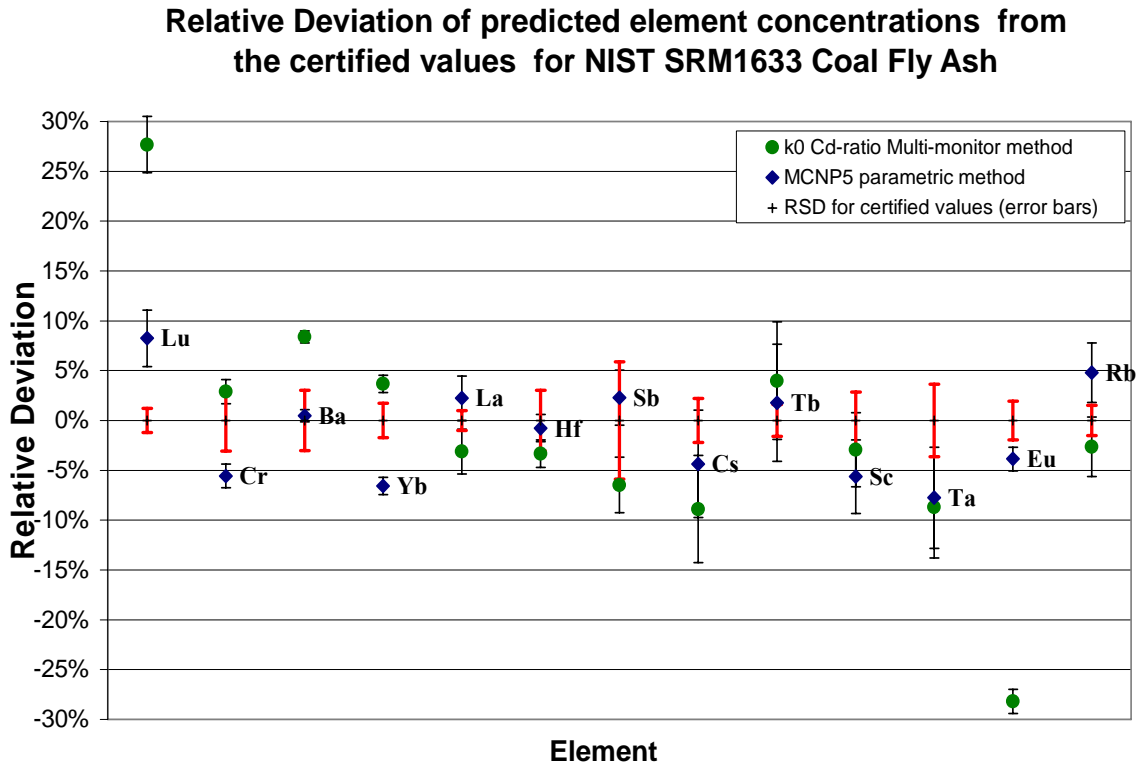
Fig. 4.1(b) A plot showing the deviation of the elemental concentrations predicted by the k_0 method (full circles) and the MCNP5 parametric method (diamonds) from the certified values for SRM1633 Coal Fly Ash, with error bars. The crosses with errors bars (about zero %) are the RSD for the certified values.

Although the actual temperatures of the Eu and Lu samples were not known during irradiation, the value of $g(T_n)$ was selected for a neutron temperature of 313.6K from reference [96]. Therefore, it is seemingly reasonable to relate the large deviation of Eu and Lu to lack of an accurate temperature reading for the SRM targets. However, for consistency in the MCNP5 predictions, the capture cross-sections for ^{176}Lu and ^{151}Eu taken from the JEFF 3.1 activation library were reconstructed with NJOY 99 at 313.6 K. The concentration predictions are still significantly better using the MCNP5 method.

Results for SRM1577 are listed in Table 4.1(c). Again, the standard deviations for the mean predicted concentrations for both methods indicate good precision for the mean n=2 split-mass measurement of SRM1577. The listed predictions from both methods indicate good agreement with the certified values.

Element	Certified conc. Mean /SD ppm	MCNP5 conc. Mean /SD ppm	Relative Deviation %	k_0 conc. Mean /SD ppm	Relative Deviation %
Mn	10.3(1)	9.5(0.1)	-8.2%	9.5(0.1)	-7.4%
Mg	604(9)	627(17)	3.9%	601(17)	-0.6%
Cu	193(10)	203.5(4)	5.5%	183.5(4)	-4.9%
Cl	2680(140)	2851(17)	6.7%	2829(17)	5.6%
Na	2430(130)	2395(8)	-1.5%	2458(8)	1.1%
K	9700(600)	9476(73)	-2.3%	9492(73)	-2.1%

Table 4.1(c) List of certified and predicted concentrations (using k_0 and MCNP) in ppm for SRM1577.   The standard deviation is also provided as error bars. The relative deviations from the certified values for each method are given as a percentage.

A plot of the relative deviation of the predictions from the certified values is presented in Figure 4.1(c). For the elements reported, both methods show good

82

agreement (i.e., within 8% of the certified concentrations). In addition, the mean of the predicted elemental concentrations and the RSD lie within the reported uncertainty (shown as the red error bars centered at zero) for the various certified concentrations. The importance of introducing a measured k_0 constant in k_0 methodology is seen for Cu. Here, the predicted k_0 concentrations for Cu, which is based on the largely deviated two-group (n, γ) reaction rate for ^{66}Cu (see Table 3.4 (a) and (b)), now appears within the SD of the certified value (i.e., within 5%). On the other hand, in the MCNP parametric methodology factors such as k_0 are not needed to predict the Cu concentration accurately.
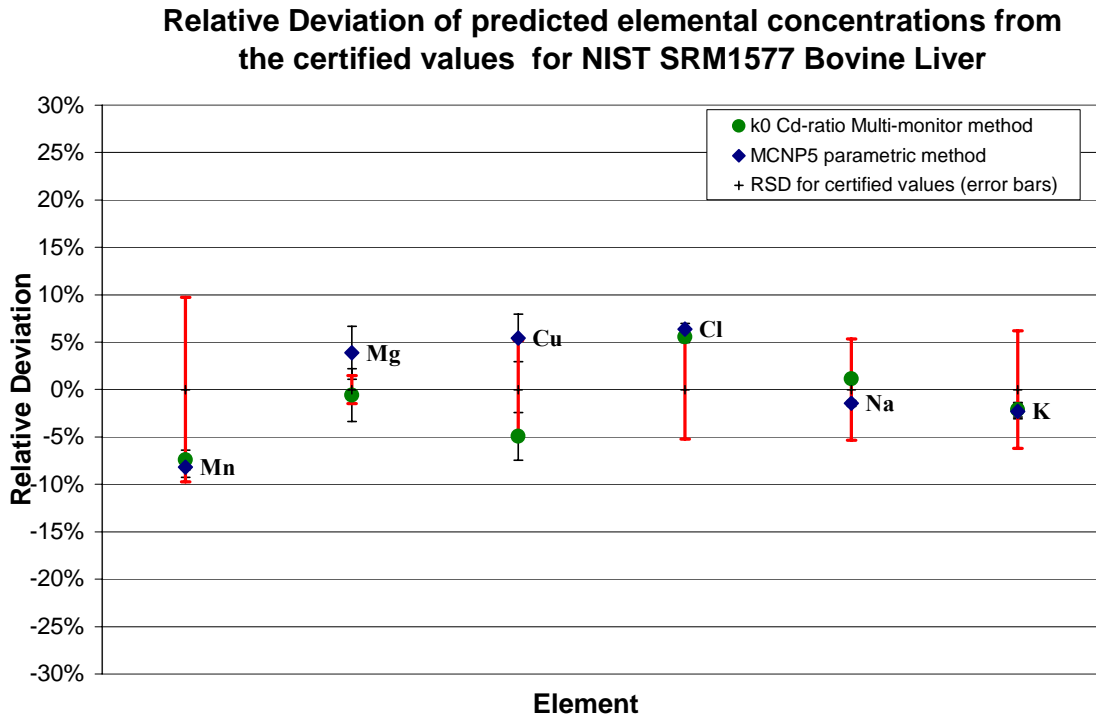
Fig. 4.1(c) A plot showing the deviation of the elemental concentrations predicted by the k_0 method (full circles) and the MCNP5 parametric method (diamonds) from the certified values for SRM1577 Bovine liver, with error bars. The crosses with errors bars (about zero %) are the RSD for the certified values.

83

Overall, both MCNP and k_0 show generally good agreement (i.e., within ~10%) in comparison to the certified values for 1/v nuclides. However, there is a large discrepancy between the relative deviation from the true values for k_0's (two-group) reaction rates and its concentrations some elements such as Cu and Zr. So far, these discrepancies can only be attributed to the measured k_0 constant used. The results presented for three NIST SRMs show that the MCNP parametric method is capable of determining trace-elemental concentrations with accuracy that is at least equal to, and for a greater number of elements, better than predictions using the k_0 parametric methodology. Most elemental concentrations predicted by the MCNP parametric methods are within 5% of certified values. The k_0 method consistently shows much poorer predictions from the non-1/v nuclides even with addition of the Westcott correction. The MCNP predictions for non-1/v nuclides are generally within 5% of certified values with its relatively simple formalism.

Chapter 5 Flux Stability Studies at MURR

5.1 Flux Stability Studies at MURR for Parametric NAA at MURR

The MCNP5 computed flux and reaction rates previously presented were benchmarked for a specific steady-state configuration of MURR core, which was repeated over three weeks. Therefore, the effects of periodic variations in the local flux distribution on the results were not explicitly examined. Since reaction rates are used to determine elemental concentrations, it is clear that variations in the spectrum can alter the predictions. More importantly, in order to extended the MCNP5 parametric methodology beyond measurements on a specific day, a careful study of the flux stability during and between fuel cycles was performed. Since the reactor's physical dimensions are relatively constant, any change in the flux distribution is initially assumed to be related to the changes in the fuel's effective absorption cross-section or changes in nearby targets. In this section, two different flux stability investigations are presented and discussed in detail. In the first study, a set of flux monitors including Au, Zr, Mg and Ti were used to monitor the changes in thermal and epithermal flux distribution between fuel cycles over a seven-week period. In the second study, a similar set of flux monitors was used to monitor the changes in the thermal and epithermal fluxes during a fuel cycle.

The intrinsic reaction rates of the pure 1/v nuclides ^{50}Ti and ^{26}Mg were measured to examine the changes in the thermal region of the spectrum. Similarly, the intrinsic reaction rates of the nuclides ^{197}Au, ^{96}Zr and ^{94}Zr were measured under cadmium covers to examine changes in the epithermal flux regions. The nuclides ^{197}Au, ^{96}Zr and ^{94}Zr act

as ideal resonance monitors when irradiated under a thermal neutron absorber since each has its largest resonance capture peaks at energies near 5.5 eV, 338 eV and 6062 eV, respectively. Figure 5.1(a) shows the ENDF-B/VII.0 neutron capture cross-sections for nuclides ^{197}Au, ^{96}Zr and ^{94}Zr. For these measurements, 1 mm thick cadmium covers were used as the thermal neutron filter. At this thickness of Cd, the transmission of epithermal neutrons is 99% and the transmission of thermal neutrons is ~ 1% [[29] and references therein]. Although there is a 1/v contribution to the epithermal cross-section for each greater than the cadmium cut-off energy of ~ 0.44 eV [[29, 31] and references therein], the neutron capture due to this 1/v portion is relatively small in comparison to capture due to the resonance peaks. Therefore, measuring the cadmium covered reaction rates for ^{197}Au, ^{96}Zr and ^{94}Zr essentially maps three very unique energy regions of the epithermal flux spectrum above the cadmium cut-off energy. These regions are depicted by monitors' effective resonance energies.

For the thermal portion of the flux spectrum, two pure 1/v nuclides were selected for this measurement because their total reaction rates are dominated by thermal neutrons. Figure 5.1 (b) shows the ENDF-B/VII.0 capture cross-sections for nuclides ^{50}Ti and ^{26}Mg. Although there is some activation due to resonance neutron capture, these contributions are small since the effective resonance energies are at relatively high energies.
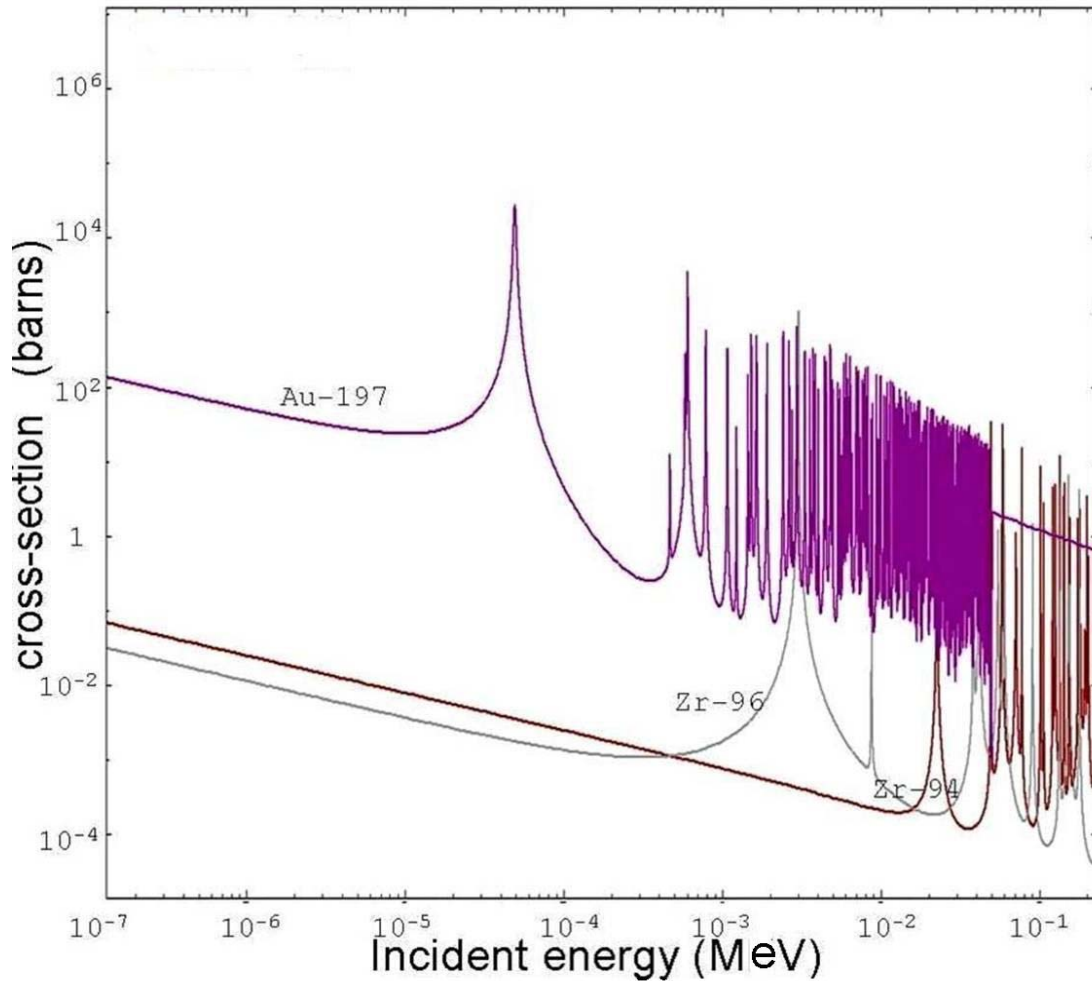
Fig. 5.1 (a) Plots of the ENDF-B/VII.0 capture cross-sections for ^{197}Au (purple), ^{96}Zr (grey) and ^{94}Zr (red) show their major resonance peaks.

For consistency with the preliminary benchmarking data, the reaction rates for this study were measured in ROW2. The resonance monitors were made from dilute (0.128%) Au in Al wire Reactor Flux wires, which were calibrated against a 0.1003% certified Au in Al wire from IRMM standards and 99.95% pure zirconium wire from Alpha Aesar. The thermal monitors were made from dilute single-element solution standards from high

purity standards. These thermal monitors were prepared similarly to those in the solution

standards reaction rate measurements (see Chapter 2). Table 5.1 lists a summary of the

nuclear properties used in this study taken from references [31].
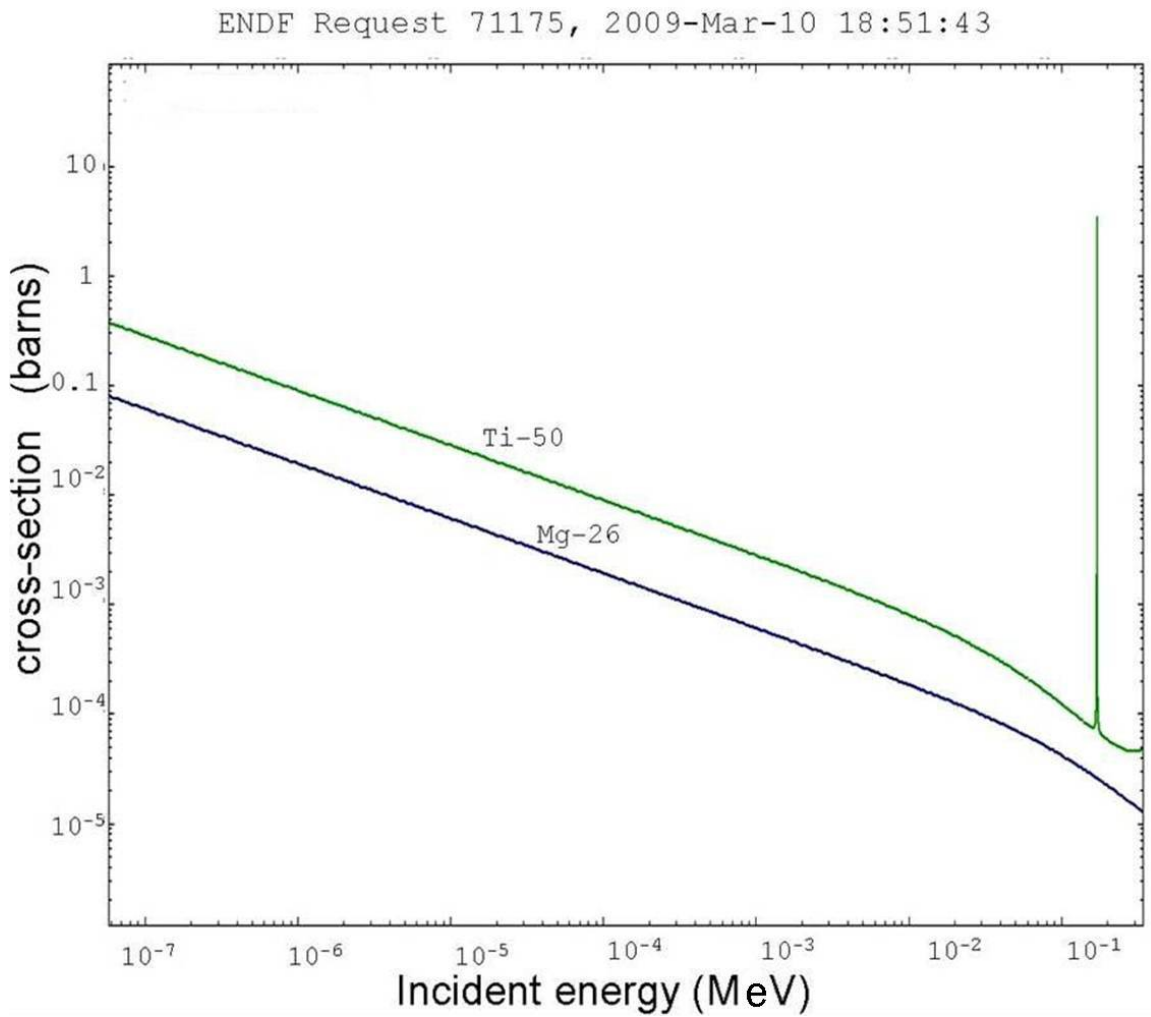
Fig. 5.1 (b) Plots of the ENDF7 neutron capture cross-sections for (*1/v*) nuclides ^{50}Ti and

^{26}Mg.

Nuclide	Monitor type	$E_{(res)}$ eV	σ(thermal) barns	Resonance Integral barns	Q_0
^{26}Mg	thermal	257000	0.038	0.019	0.64
^{50}Ti	thermal	63200	0.18	0.088	0.67
^{197}Au	resonance	5.5	98.7	1569.35	15.7
^{96}Zr	resonance	338	0.023	5.32	248
^{94}Zr	resonance	6260	0.050	0.321	5.05

Table 5.1 Summary of properties for the different nuclides used in the study. The thermal capture cross-section and resonance integral are taken from Ref. [66].

5.2 Flux Stability between Fuel Cycles

The MURR facility operates on a weekly cycle (150 hours), and refueling is done in one day. Therefore, the irradiation of a set of thermal (1/v) and resonance monitors was repeated on the same day (or reactor configuration) of the week for seven weeks. This way, any the effects that refueling the core may have on the flux distribution in ROW2 can be examined. Measurements of the thermal 1/v monitors were done in quintuplet whereas the resonance monitors were done in triplicate. The 1/v targets were counted on DECTECTOR 2 in an identical configuration, and the resonance monitors were counted on REAR4. Results are presented separately for thermal and resonance monitors. Table 5.2 lists the results of the mean reaction rate measurements for the thermal monitors along with the RSD for each measurement. Figure 5.2 shows a plot of the reaction rates for the thermal monitors ^{50}Ti and ^{26}Mg over the seven week period.

Exp. Date	Mean (n=5) ^{50}Ti reaction rate s^{-1}	^{50}Ti RSD	Mean (n=5) ^{26}Mg reaction rate s^{-1}	^{26}Mg RSD
19-Sep-08	9.77E-12	0.71%	2.04E-12	2.99%
26-Sep-08	9.69E-12	1.03%	2.00E-12	1.89%
10-Oct-08	9.86E-12	0.73%	2.01E-12	0.74%
17-Oct-08	9.95E-12	1.06%	2.05E-12	1.40%
24-Oct-08	9.97E-12	0.56%	2.07E-12	1.37%
31-Oct-08	1.00E-11	0.81%	2.08E-12	0.67%
7-Nov-08	1.02E-11	1.27%	2.06E-12	0.87%
Average /RSD	9.92E-12	1.68%	2.04E-12	1.54%

Table 5.2 The list of results of the mean reaction rate measurements for the thermal monitors along with the RSD for each measurement.

Thermal (1/v) Actiavtion Rate Stabilities for ^{50}Ti and ^{26}Mg
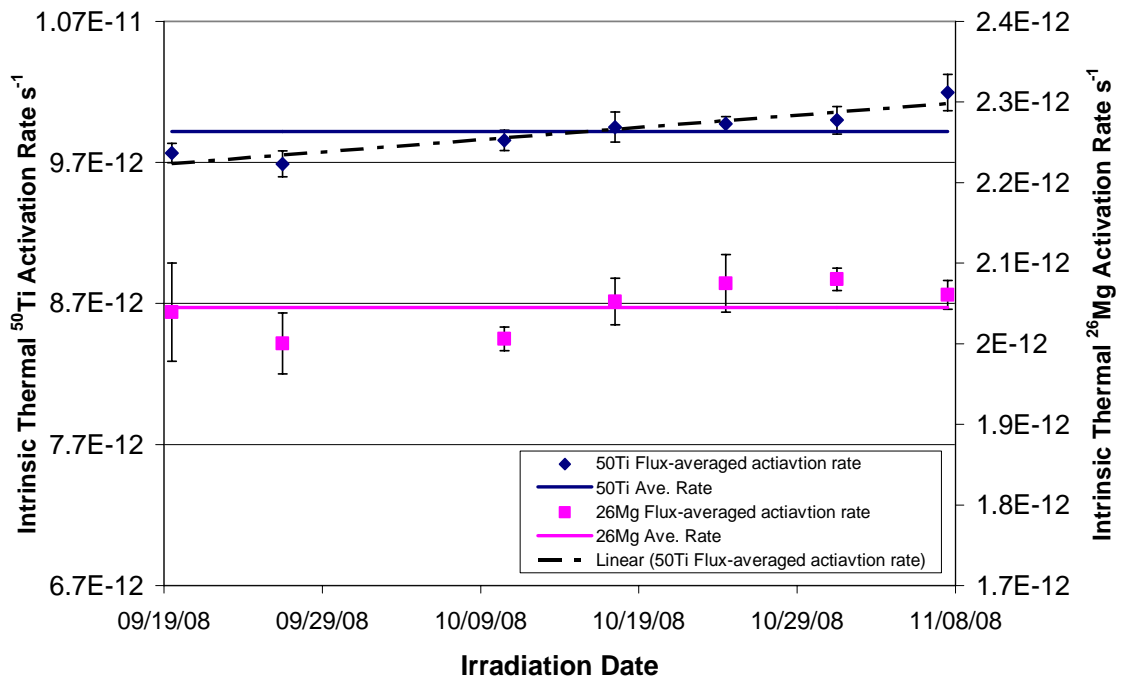
Fig. 5.2 A plot of the flux-averaged reaction rates for ^{50}Ti (diamonds) and ^{26}Mg (squares) over seven weeks. The solid line through each set of data points represents the average reaction-rate. The standard deviation for each measurement is shown as the errors bars. A linear regression fit is shown for the ^{50}Ti data.

The RSD for the mean n=5 measurements of the thermal monitors indicates excellent external precision. The RSD for each n=5 reaction rate measurement is ~1% for each monitor. The RSD for the mean n=7 ^{50}Ti reaction rate over the period of the experiment is 1.68% while that for the ^{26}Mg is 1.54%. As depicted in Figure 5.2, the data generally indicate a stable thermal flux over the two months period. The solid line through each data set is the overall average value for the measured reaction rates. However, a closer analysis of the data set reveals that there maybe a trend in the data sets over time.

A single-factor ANOVA statistical test was done over all reaction rate data for Ti-50 and Mg-26 (in EXCEL) at the 99% confidence limit. For the Ti-50 data, the calculated *F*-value is larger than the critical *F*-value suggesting the (reaction-rate) means are not normally distributed [105]. This is also true for a reported *P*-value less than the *P*-value at the confidence limit. The ANOVA results for the Mg-26 data suggest the mean reaction rates are normally distributed since the calculated values of *F* and *P* allow the null hypothesis. A summary of the ANOVA test for Ti-50 and Mg-26 is presented in Table 5.3 (a).

ANOVA	N(data points)	F	F-critical	P-value	P-value at Confidence Limit
Ti-50	35	13.05426	3.811725	3.84E-06	0.01
Mg-26	35	0.832506	3.527559	0.555047	0.01

Table 5.3 (a) The results of ANOVA tests in EXCEL@ showing the calculated *F* and *P* values for the n=35 Ti-50 and Mg-26 reaction rate data set. The values for the Ti-50 data set suggest the reaction rates are not of a normal distribution while those from Mg-26 reaction rate data set are.

A linear regression analysis (represented by the dashed line in Figure 5.2) shows that the data for ^{50}Ti has a slight increase over the seven week period (see Table 5.3 (b)).

Linear	Coefficients	Standard Error	P-value
Intercept	9.7E-12	4.28E-14	3.19E-11
X Variable	1.05E-14	1.7E-15	0.0016
ANOVA		F	Significance F
Regression		38.366	0.0016

Table 5.3 (b) A summary of a linear regression done (in EXCEL) for the reaction rates of ^{50}Ti. The results of ANOVA show that the F-value is larger than the value of significance (the critical value), which suggests that the n=5 mean Ti rates are not from a normal distribution.

For the resonance monitors, each target was irradiated under cadmium and the epi-cadmium reaction rates were determined. Table 5.4 lists the results of the mean epi-cadmium reaction rates for the resonance monitors along with the RSD for each measurement. Figures 5.3 (a) and (b) show the plots of the epi-cadmium reaction rates for the monitors ^{197}Au and ^{96}Zr, and ^{94}Zr over the seven weeks, respectively.

Exp. Date	Mean (n=3) ^{197}Au reaction rate s-1	^{197}Au RSD	Mean (n=3) ^{96}Zr reaction rate s-1	^{96}Zr RSD	Mean (n=3) ^{94}Zr reaction rate s-1	^{94}Zr RSD
19-Sep-08	2.44E-09	1.59%	6.81E-12	0.90%	3.62E-13	5.14%
26-Sep-08	2.391E-09	0.74%	6.93E-12	0.84%	3.28E-13	1.56%
10-Oct-08	2.38E-09	0.75%	6.69E-12	0.51%	3.36E-13	2.58%
17-Oct-08	2.31E-09	0.73%	6.23E-12	1.29%	3.06E-13	0.87%
24-Oct-08	2.22E-09	0.11%	5.35E-12	1.09%	2.91E-13	1.97%
31-Oct-08	2.33E-09	0.96%	6.27E-12	0.29%	3.10E-13	0.40%
7-Nov-08	2.32E-09	1.08%	6.37E-12	1.16%	3.02E-13	1.37%
Average/RSD	2.34E-09	3.03%	6.38E-12	8.31%	3.19E-13	7.53%

Table 5.4 The list of results of the mean reaction rate measurements for the resonance monitors along with the RSD for each measurement.

The RSD for the mean n=3 reaction rate for ^{197}Au and ^{96}Zr show good precision of ~1 %, which essentially reflects the uncertainty on counting statistics for each ^{197}Au and ^{96}Zr measurement. The RSD for the mean n=3 reaction rates for ^{94}Zr over seven weeks is larger than those for ^{197}Au and ^{96}Zr. However the counting statistics for ^{94}Zr are closer to 3%.

The epi-cadmium reaction rates reported for ^{197}Au, ^{96}Zr and ^{94}Zr show the variation for three different regions of the epithermal flux over seven fuel cycles. Plots of the epi-cadmium reaction rates in Figure 5.4 generally show a slight decrease with the exception of a significant drop in week five. Although this trend is consistent for all resonance monitors, the largest drop is observed for ^{96}Zr. The RSD for the mean of the ^{96}Zr activation over all fuel cycles is 8.3%. Here, most of the variance is due to the large drop during fuel cycle 5. The largest deviation between the maximum and minimum measured reaction rate is observed for ^{96}Zr (~20%). This is not surprising since ^{96}Zr is the most sensitive nuclide to epithermal activation (i.e., Q_0 =248).

(a)

Zr 94 Epi-Cadmium Actiavtion Rate
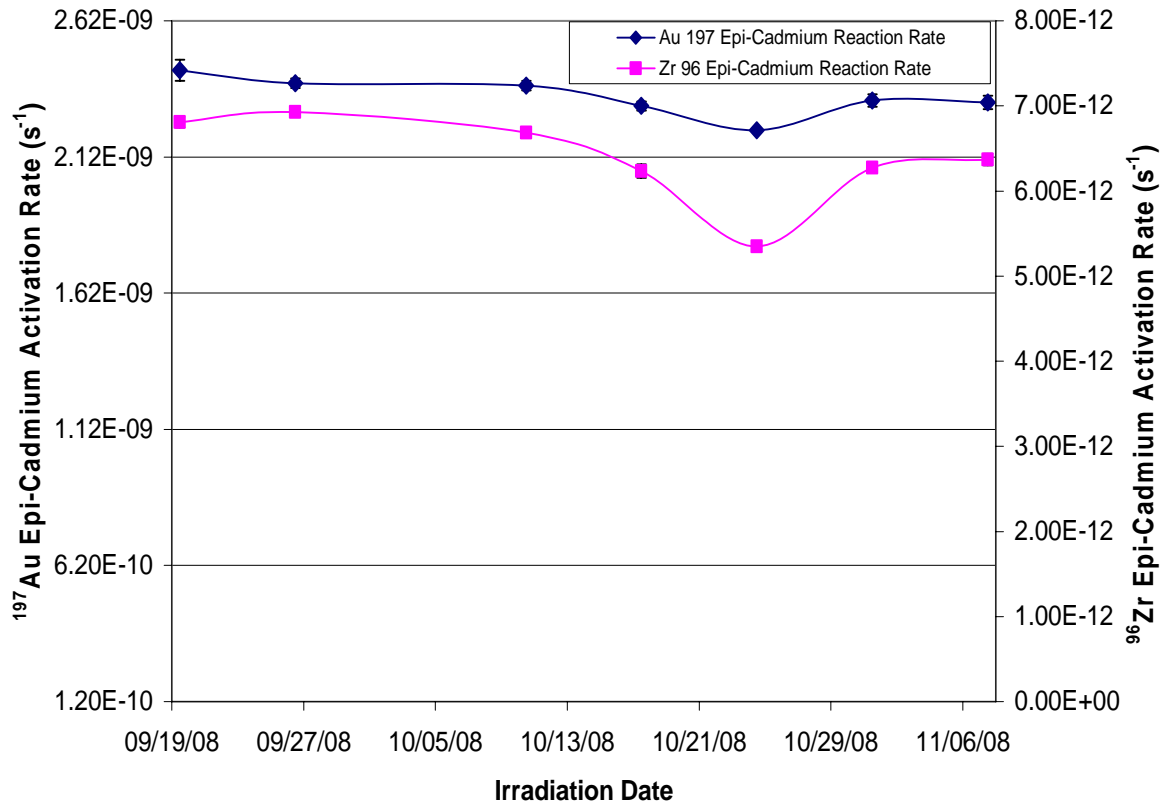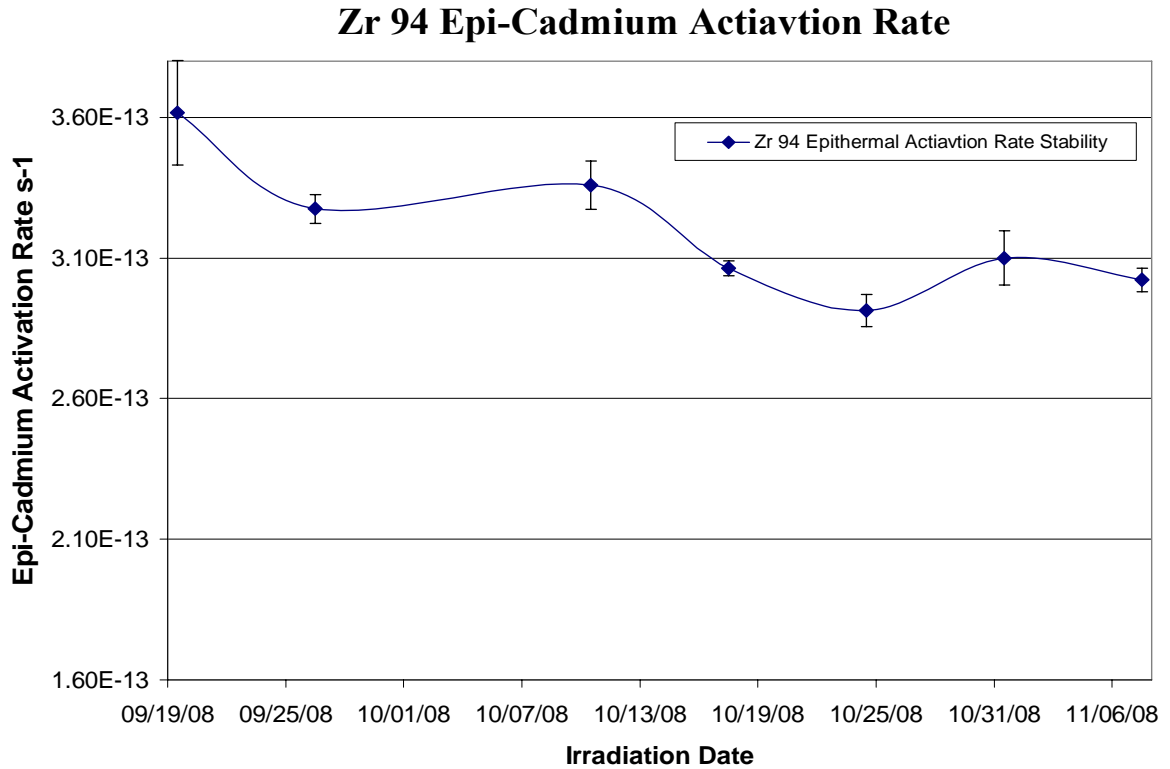
(b)

Fig. 5.3 Plots of the epi-cadmium reaction rates for resonance monitors [197]Au, [96]Zr and [94]Zr are depicted in panels (a) and (b), respectively. The uncertainty for each measurement is shown as the error bar. A large drop in the epi-cadmium reaction rates is consistent for all three monitors in week 5.

To confirm whether the dip in the epithermal flux in week 5 is a real effect due to fuel reloading, the MURR fuel status maps for four fuel cycles, including the week five fuel loading, were carefully examined. The panels in Figure 5.5 show the entry fuel status maps for measurements made on the 26th September 2008 to 24th October 2008. The fuel element label and its age in terms of megawatt-days (MWD) for each are shown. The fuel

95

elements with similar MWD are arranged in pairs opposite to each other. The two pairs with the least MWD are positioned orthogonal to each other. This arrangement is consistent for every refueling so that the steady-state core always has a symmetric flux distribution. The position of ROW2 is indicated in reference to the fuel arrangement for each status map.

Start up fuel load: 09/22/08

MURR Fuel Status Map

ROW2
Relative
Position

MO-729 (F5)
(9) MWD

MO-711 (F4)
(121) MWD

MO-717 (F6)
(105) MWD

MO-721 (F3)
(68) MWD

Flux
Trap

MO-720 (F7)
(68) MWD

MO-716 (F2)
(105) MWD

MO-715 (F8)
(121) MWD

MO-728 (F1)
(9) MWD
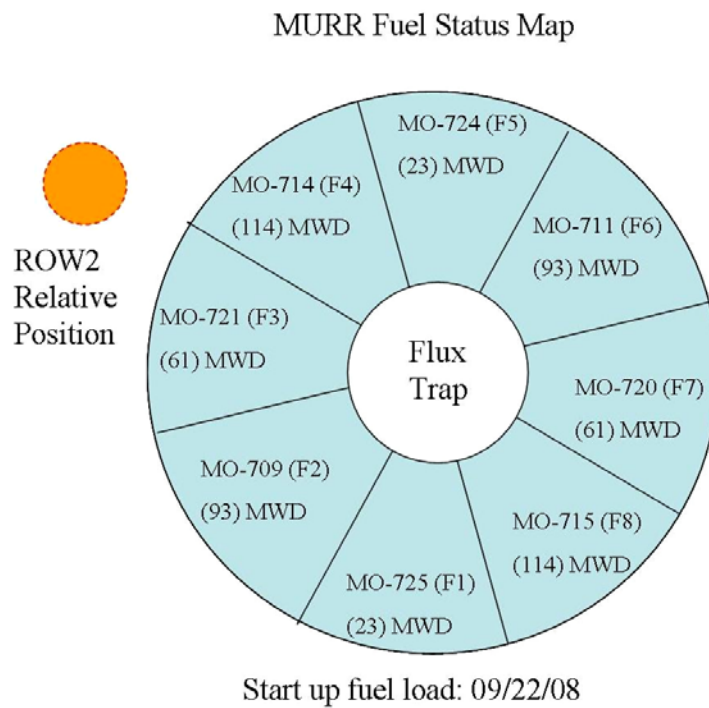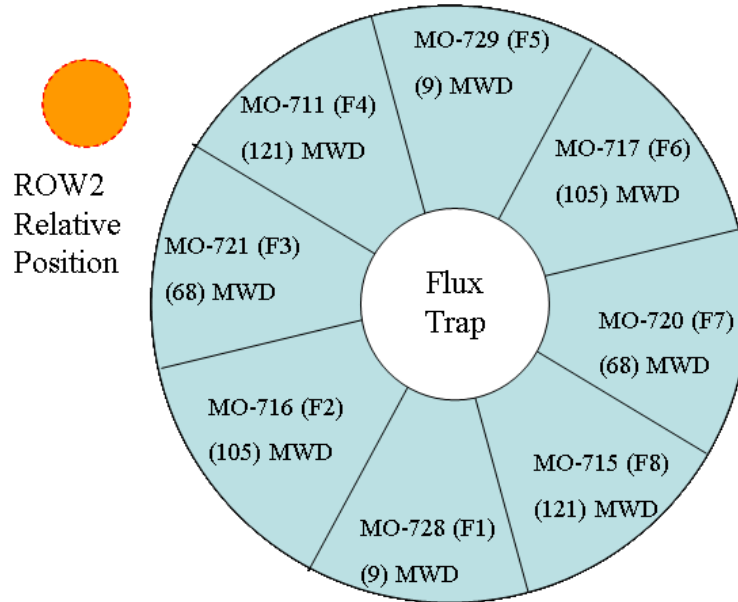
Start up fuel load: 10/06/08

MURR Fuel Status Map

ROW2
Relative
Position

MO-731 (F5)
(9) MWD

MO-711 (F4)
(101) MWD

MO-713 (F6)
(135) MWD

MO-722 (F3)
(51) MWD

Flux
Trap

MO-723 (F7)
(51) MWD

MO-712 (F2)
(135) MWD

MO-709 (F8)
(101) MWD

MO-730 (F1)
(9) MWD

Start up fuel load: 10/13/08

MURR Fuel Status Map
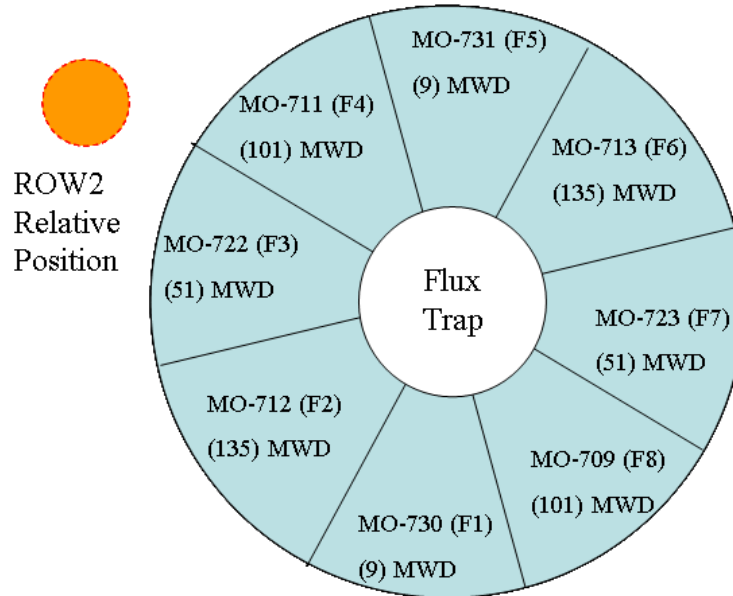
Start up fuel load: 10/20/08
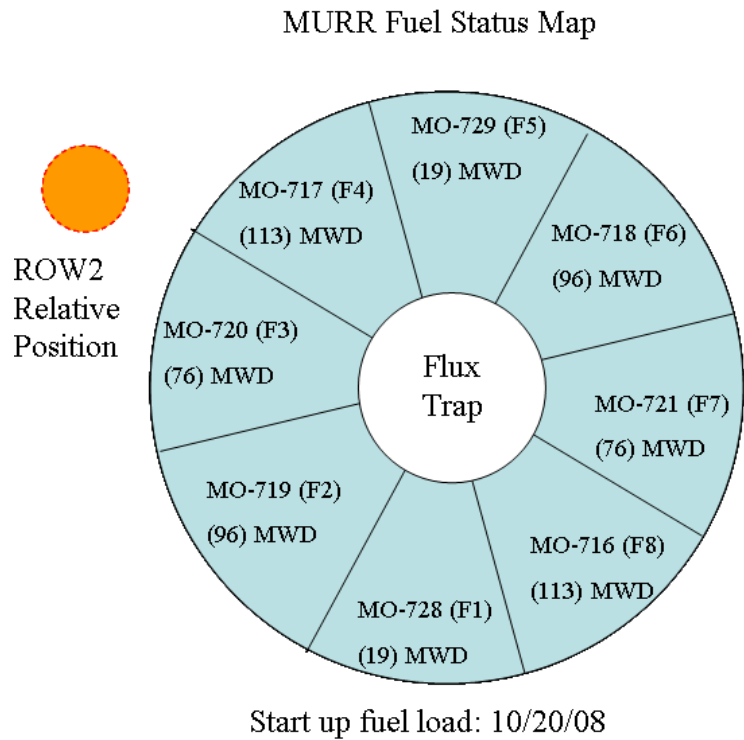
Fig. 5.4 MURR fuel status maps showing the entry fuel loads for 4 fuel cycles.

Considering the half-section of the core that is adjacent to ROW2, for these four separate fuel loadings, the total MWD is not very different. For instance, in the half core adjacent to ROW2, the total MWD for the 22nd September 2008 is ~5% less than that for the fuel load for the week of the 20th October 2008. However, a 5% increase in the MWD is not sufficient to explain the large drop in the epi-cadmium reaction rates measured during that fuel cycle. Therefore, a set of MCNP5 calculations was done to simulate the epithermal and thermal fluxes in ROW2 based on each fuel loading shown in Figure 5.4.

If the fluxes vary due to refueling the core, then this suggests that the total material composition of the fuel is different each time the fuel assembly is replaced. When ^{235}U undergoes neutron-induced fission (mostly from thermal neutrons), the asymmetric mass

split creates a large variety of fission products [26] with various half-lives. In particular, the fission product-poisons ^{135}Xe and ^{151}Sm are created with relatively high cumulative mass yields (i.e., ~6%) [26]. Since the steady–state conditions in a reactor require stable (neutron-induced) fission chain-reactions, the quantities of ^{135}Xe and ^{151}Sm must be monitored. These two fission-products, ^{135}Xe and ^{151}Sm in particular, have extremely large thermal neutron capture cross-sections of 2,647,600 and 151,670 barns, respectively [31, 33]. However, ^{135}Xe has a half-life of 9.14 hours; therefore this poison is not expected to be present in the start-up fuel load. On the hand, ^{151}Sm has a half life of 90.0 years and various quantities are expected to be present in the start-up fuel load at MURR.

Using the previously established detailed MCNP model of MURR, four unique models were created differing only by their fuel material definitions. Here, each model reflects each of the four start-up fuel loadings shown in Figure 5.4. Since ^{151}Sm is expected to be present in the spent fuel elements of the start-up core, an estimation based on the age of each fuel element is supplied to correct the start-up fuel definitions. This was done by a simple ratio using the MURR engineering specification that 1.5 grams of ^{235}U is utilized per every 10 MWD in each fuel element, the cumulative mass yield of ^{151}Sm for the fission of ^{235}U and the MWD on the particular fuel element.

Next, the complex burnup simulation code MONTEBURNS 2.0 [106] was used to couple the MCNP5 models to the isotope depletion/production code ORIGEN 2.2 [107]. This was done to account for changes in fuel material during each fuel cycle. Here, each MONTEBURNS calculation was set to simultaneously model the burnup of each fuel element in the assembly during normal operation. The simulation period extends from the reactor startup until the end of the measurement for the resonance flux monitors (i.e., ~4

days). MONTEBURNS continually creates an updated definition for the material being burnt (or transformed by nuclear processes) until the end of the burnup simulation. Here, the final MONTEBURNS fuel definitions (including all fission products in correct proportions) for each fuel load were substituted into the respective MCNP model. Next, static MCNP5 kcode calculations were performed to examine the epi-cadmium and (1/v) reaction rates in ROW2 for each fuel cycle.

For the reaction rate calculations done in MCNP5, ^{96}Zr is used for the resonance monitor, while ^{50}Ti is used for the (1/v) thermal monitor. The JEFF 3.1 Activation library was used to predict the reaction rates. The rates are tallied in two energy bins, where the upper energy cut-off energy for thermal bin is set to 0.44 eV and 10 MeV for the epithermal bin. Figure 5.5 (a) shows a plot of the MCNP predicted epi-cadmium reaction rates for ^{96}Zr (full circles) during the fuel cycle in comparison to the measured reaction rates (full squares) from weeks 9/22/08 to 10/20/08,

MCNP Cal. Zr 96 Epi-cadmium Activation Rate
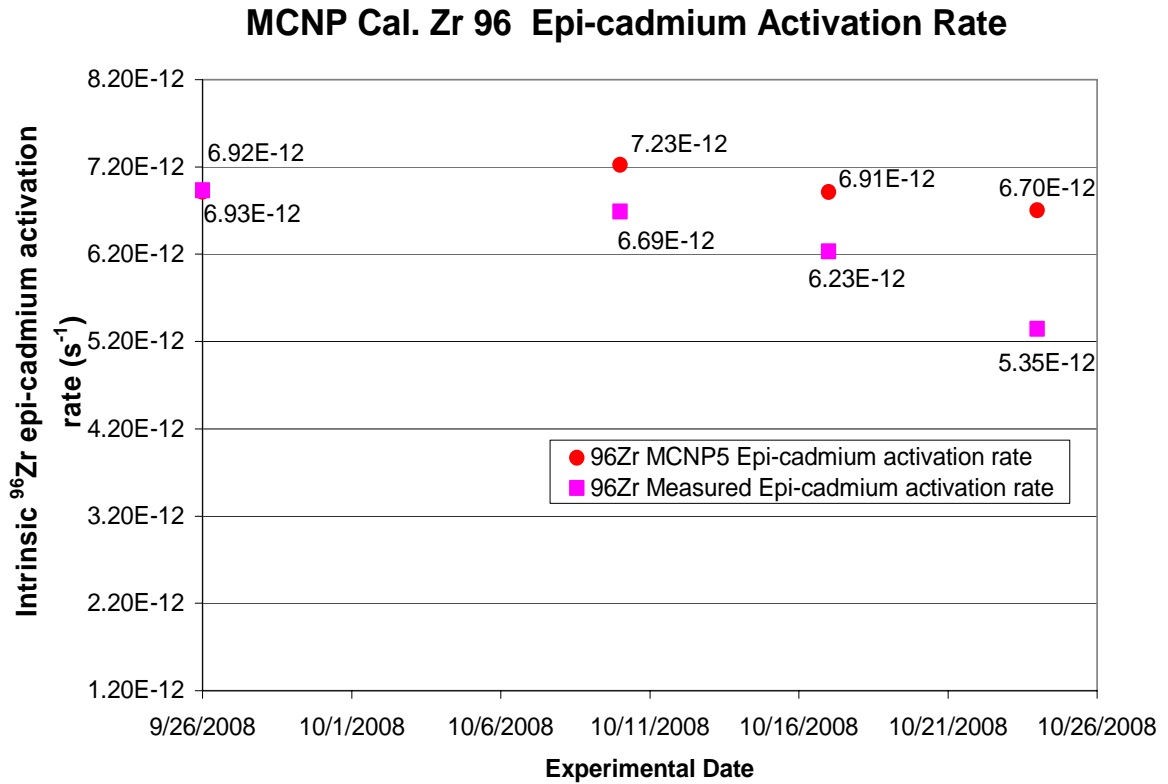
Fig. 5.5(a)   A plot of the MCNP5 predicted epi-cadmium reaction rates for ^{96}Zr in ROW2 for the fuel cycles beginning the week of 9/22/08 to the week of 10/20/08.

Although the epi-cadmium reaction rate for the second fuel cycle shown here is slightly higher than expected, the trend is clearly not consistent with the observed trend in the measurements. The results suggest that there is no correlation between the trends in epi-cadmium rates (or epithermal flux) and weekly fuel loading. The RSD for the mean of the MCNP5 predictions is ~3%, which is significantly smaller than RSD = 8.3% for the measurements. This supports the idea that most of the variance in Figure 5.4(c) is due to the measurements on 10/20/08. Figure 5.5(b) shows a similar plot for the computed and measured thermal (flux-averaged) reaction rate for ^{50}Ti over the same fuel cycles.

101

The RSD for the mean of the MCNP predicted ^{50}Ti reaction rates over n=4 fuel cycles is 0.33%. This even further suggests that there is no correlation between refueling and the trends observed in the measurements.
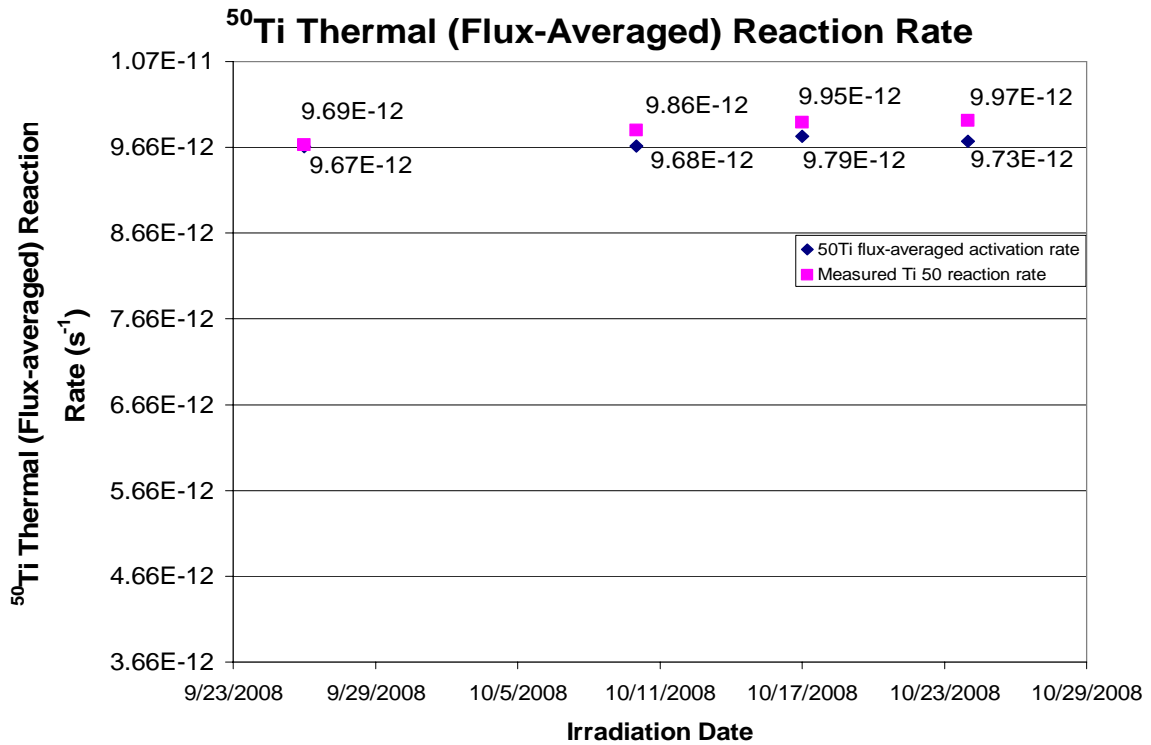
Fig. 5.5 (b) A plot of the MCNP5 predicted flux-averaged reaction rates for ^{50}Ti in ROW2 for the fuel cycles beginning the week of 9/22/08 to the week of 10/20/08.

The burnup simulations involving MONTEBURNS 2.0, MCNP5 and ORIGEN 2 fueling loadings at MURR indicate that there is no correlation between refueling and thermal or epithermal flux stability. However, the data from the thermal flux monitors indicates a slight increase in the thermal flux over the seven week period. The resonance monitors

suggest a slight decrease in the epithermal flux overall, but a significant drop is observed for measurements made during the fuel week of 10/20/08.

The opposite trends observed in the measured thermal and epi-cadmium reaction rates leads one to speculate that the observed changes may be related to a neutron moderation effect. Since all neutrons created in the core under steady state conditions must be accounted for, a decrease in epithermal flux must be accompanied by an increase in the thermal flux. Two intrinsic properties of a moderator that can be altered to yield variations in the flux are its effective elastic scattering cross-section and its atom density. Because MURR is a light-water moderated reactor where the core is submerged in 20,000 gallons of recycling DI water, changes in the macroscopic elastic scattering cross-section can occur due to changes the atom density of water. One physical property that can change the atom density is the temperature of the water.

A very preliminary investigation was carried out by plotting the daytime high and average temperatures for the area, over the length of the measurements. Figure 5.6 shows a plot of the average and maximum daytime temperature for the area for the days of the flux monitor measurements. The temperature data was taken from the National Weather Service at NOAA.
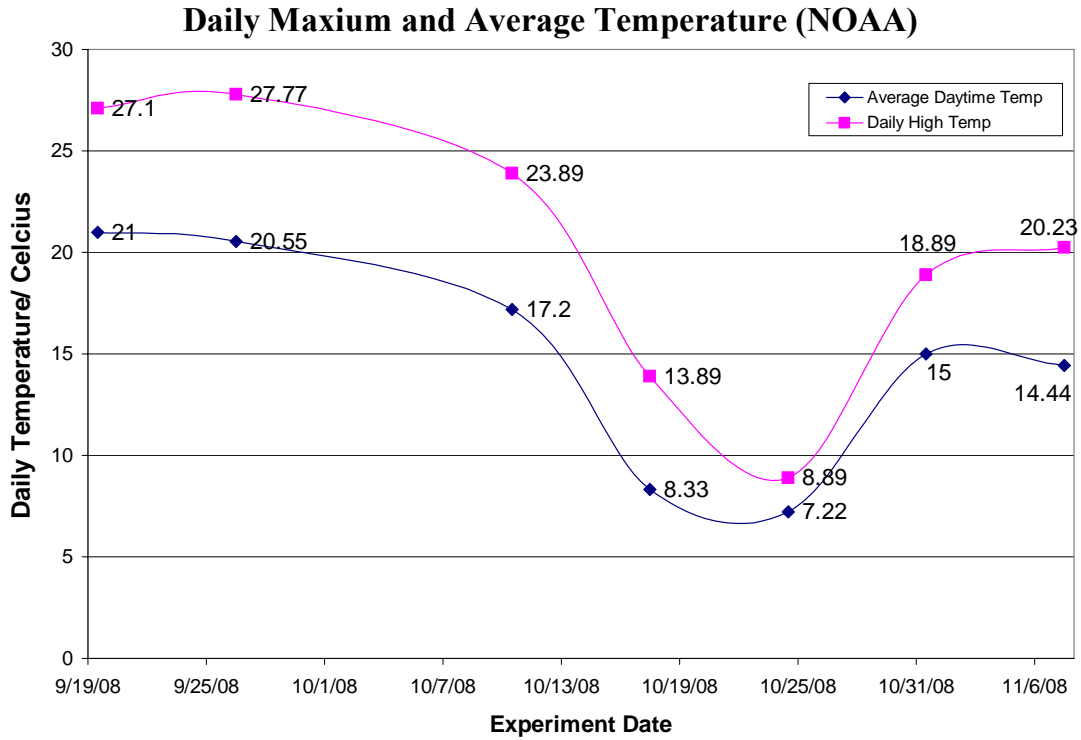
Fig. 5.6 A plot of the daytime average outside temperature for Columbia, MO for the experimental dates. The large drop in temperature appears to correlate to the depression in the epithermal flux indicated by epi-cadmium reaction rates the resonance monitors ^{197}Au and ^{94,96}Zr.

The trend in the daily outside temperature appears to correlate with the observed trend in the measured epi-cadmium reaction rate data. Considering that the system (the core) is not completely isolated from the outside, it can be assumed that the outside temperature does influence the water surrounding the reactor core. The observed changes in the trends in the epithermal flux could be rationalized as follows. A decrease in the moderator (water) temperature under normal atmospheric pressure will cause the atom

density to increase. The increase in atom density will increase the collision probability (i.e., the macroscopic elastic scattering cross-section) for neutrons traversing the moderator, hence enhancing its moderating power [18, 19]. The result would be a softer neutron flux spectrum, which in effect, increases the number density of thermal neutrons while decreasing the epithermal neutrons as the trends in the reaction rate measurement suggest. However, it is important to understand that the measured reaction rates do not directly reflect the magnitude of the thermal or epithermal fluxes since each nuclide has a unique sensitivity to the thermal and epithermal fluxes. Small changes in the epithermal flux can result in much larger changes in the epithermal reaction rates because of the presence of resonances at particular energies. This is specially the case for nuclides that are very sensitive to epithermal activation. Nonetheless, the trend in the reaction rates will be reflected in the local flux distribution.

In order for this temperature effect to be conclusive, actual temperature measurements of the pool water closest to ROW2 on the irradiation dates are absolutely necessary. Unfortunately, there are no such temperature measurements. A temperature measurement of the water that flows through the secondary loop is only made at the far away heat-exchange point, where the inlet and outlet temperature is recorded. It is still uncertain whether the temperatures at these two points accurately reflect the true temperature of the pool water surrounding the irradiation channels. However, an indirect temperature effect on the fluxes is still inconclusive and further detailed investigation is needed. In any case, this study has shown that thermal and epithermal reaction rates are not expected to vary greater than 2% and 10%, respectively, between fuel cycles.

5.3 Flux Stability during a Fuel Cycle

A set of measurements was made to determine the stability of the thermal and epithermal flux during a given fuel cycle. Single targets made from Ti, Au and Zr standards were irradiated sequentially on the same day to measure the flux-averaged and the epi-cadmium reaction rates. The measurement was repeated daily for the duration of the fuel cycle in ROW2. In this experiment, the set of Ti monitors used in the previous measurements were reused and an identical set of resonance monitors was made for every irradiation. Reusing the Ti monitors did not constitute an activity problem since the half-life of the activation species ^{51}Ti, is only 5.76 minutes. Since this is not the case for the resonance monitors, similar targets were made from the exact stocks as the previous measurements. Using the effective resonance energies of the monitors, the flux spectrum is essentially reduced to a four group energy structure. All thermal monitors were counted in an identical geometry on DETECTOR 2 while all resonance monitors were counted in an identical geometry on REAR4.

Results for the intrinsic reaction rate of ^{50}Ti and the epi-cadmium reaction rates for resonance monitors ^{197}Au, ^{94}Zr and ^{96}Zr are presented in Table 5.5. Plots of the daily reaction rates are presented in Figure 5.7 (a) for thermal monitor ^{50}Ti (diamonds) and for resonance monitors ^{197}Au (squares) and ^{96}Zr (triangles), while results for the epi-cadmium reaction for ^{94}Zr are presented in Figure 5.7 (b).

106

Exp. Date	^{50}Ti reaction rate s-1	^{197}Au reaction rate s-1	^{96}Zr reaction rate s-1	^{94}Zr reaction rate s-1
1/13/09	9.78E-12	2.17E-09	6.09E-12	2.80E-13
1/14/09	1.00E-11	2.28E-09	6.62E-12	3.02E-13
1/15/09	1.02E-11	1.96E-09	6.30E-12	3.07E-13
1/16/09	9.83E-12	2.38E-09	6.60E-12	3.10E-13
1/17/09	1.00E-11	2.39E-09	6.56E-12	3.12E-13
1/18/09	9.96E-12	2.46E-09	6.63E-12	3.14E-13
Average	9.97E-12	2.27E-09	6.47E-12	3.04E-13
RSD	1.58%	8.07%	3.45%	4.07%

Table 5.5 Results for the n=1 daily reaction rate measurements for the thermal and resonance monitors along with the RSD for each measurement

Reaction Rates for Thermal Monitor Ti 50 and Epi-cadmium Monitors Au 197 and Zr 96

(a)

Zr 94 Epi-cadmium Reaction Rate
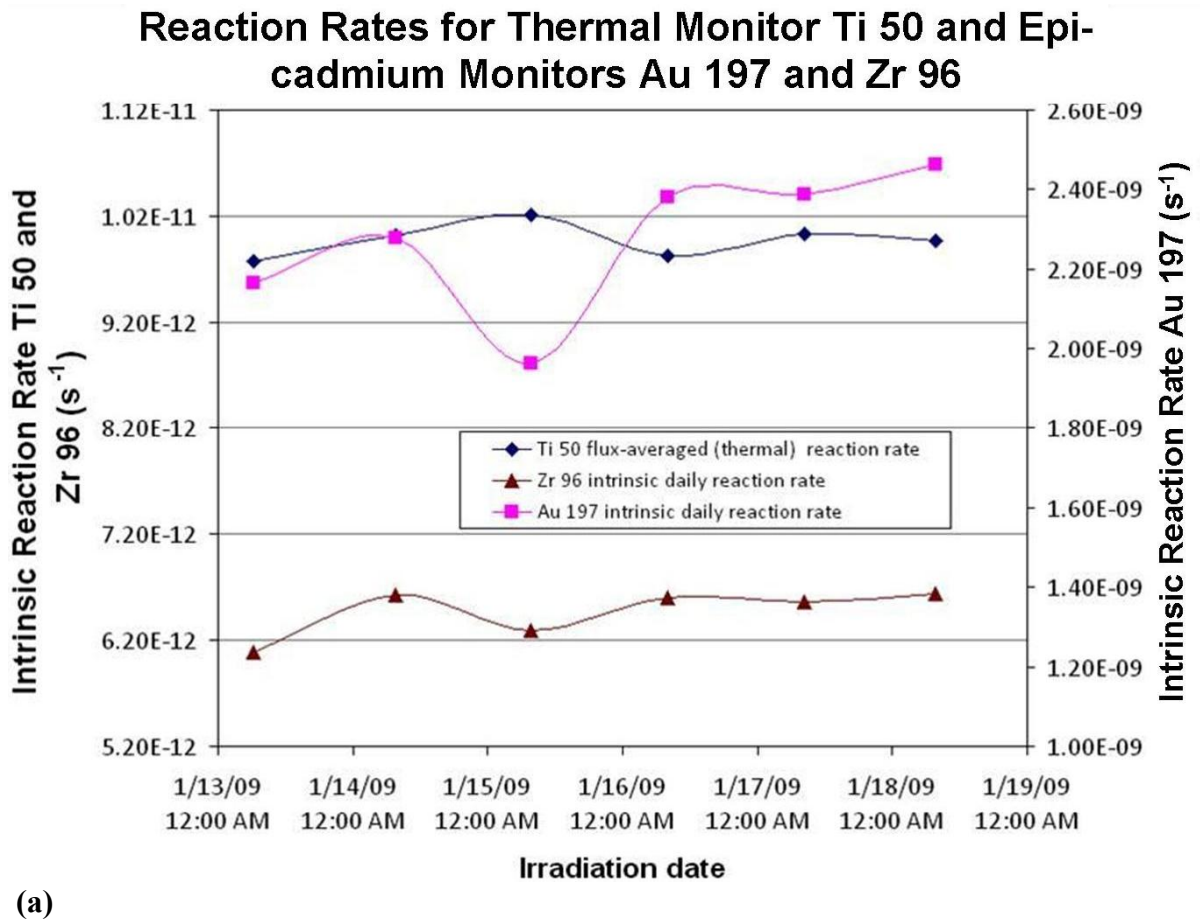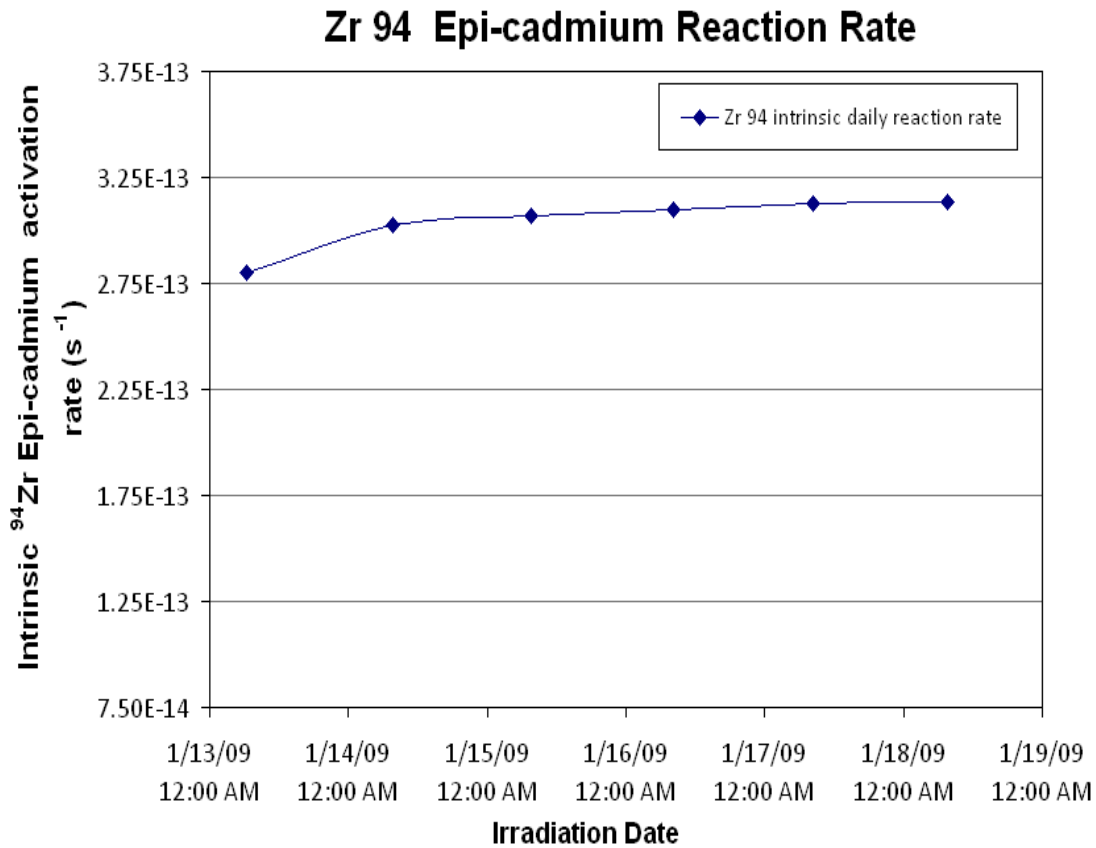
(b)

Fig. 5.7 Panel (a) shows plots of the flux-averaged reaction rate for the thermal monitor [50]Ti and the epi-cadmium reaction rates for [197]Au and [96]Zr. Panel (b) shows the epi-cadmium reaction rate for [94]Zr. Except for [94]Zr, the reaction rates show an observable variation on 1/15/09.

The results of all the data show a noticeable increase in the reaction rates between the first and second day, after the reactor is at full power. Since the first point is measured shortly after the reactor is brought to full power, this can be explained by the movement of the boral control blades in reference to the irradiation position in ROW2. Boron is a very strong absorber of thermal neutrons and it is used in the control blades to control the

108

fission rate within the fuel. In which case, if the height of the control blades is closer to the height of the target in its irradiation position, the total flux experienced by the target is lowered. Therefore, the general increase in the reaction rates at the second point is consistent with the movement of the control blades further way from the target. Therefore, the reaction rates are expected to gradually plateau.

Although the rates generally appear to plateau after the second point, there appears to be a significant variation in the reaction rates for ^{50}Ti, ^{197}Au and ^{96}Zr on the third measurement. The variation is largest for the ^{197}Au epi-cadmium reaction rate. More interestingly, the trends appear to vary in opposite directions for the thermal monitor verses the resonance monitors. That is, the thermal monitor shows an increase in the flux-averaged reaction rate (indicative of the thermal flux), while the resonance monitors show a decrease in the epi-cadmium reaction rates (indicative of the epithermal flux). However, no such depression was observed for the ^{94}Zr epi-cadmium reaction rates in this measurement. Overall, the RSD for reaction rates for ^{50}Ti, ^{197}Au, ^{96}Zr and ^{94}Zr of 1.6%, 8%, 3% and 4%, respectively, tend to indicate reasonable stability in thermal and epithermal fluxes during the fuel cycle. No statistical tests were done here since n=1 measurement of each flux monitor was done for each day during the fuel cycle.

Nonetheless, the apparent trends in this data set are similar to those of the previous measurements, once again suggesting a neutron moderation effect. Therefore, the daily average temperature over the course of the measurement was plotted and is shown in Figure 5.8.
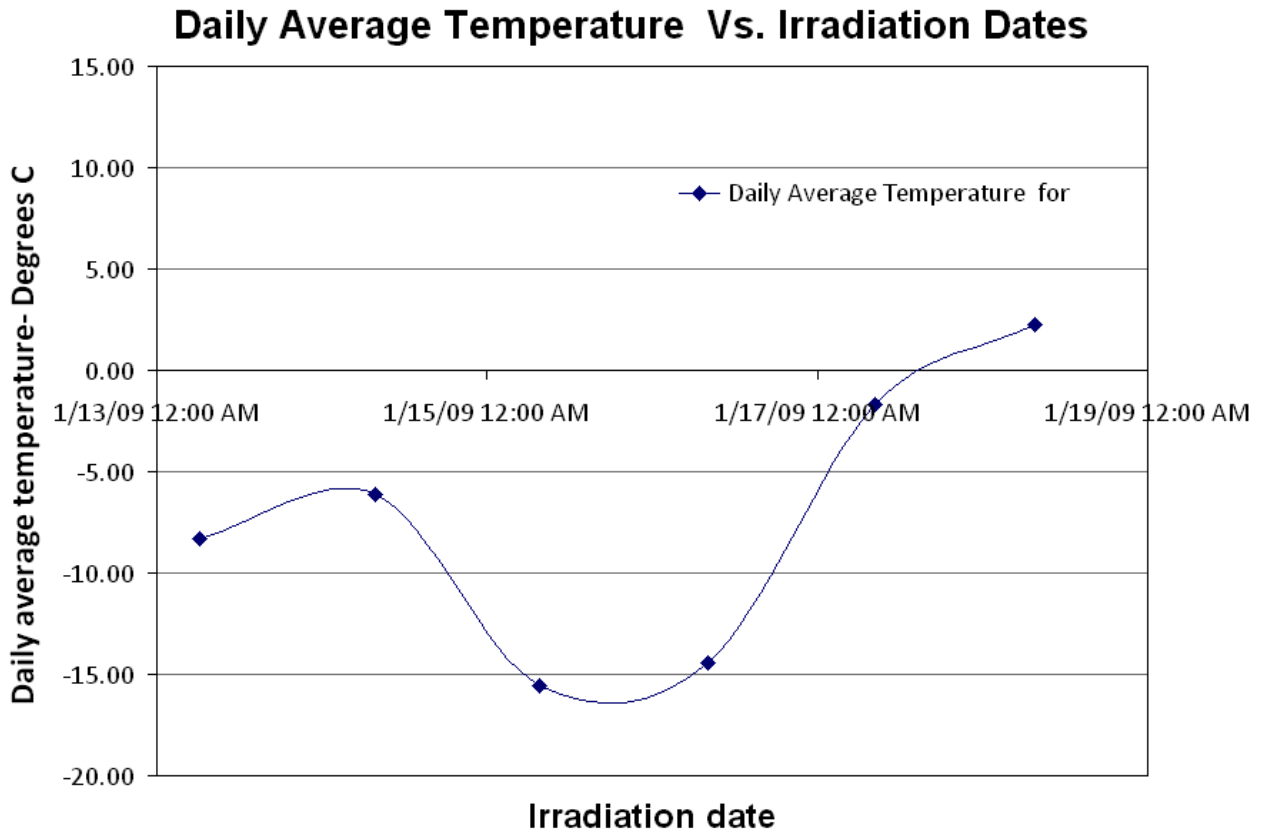
Fig. 5.8 A plot of the daytime average outside temperature for Columbia, MO from 1/13/09 through 1/18/09. The large drop in temperature appears to correlate to the depression in the epithermal flux indicated by epi-cadmium reaction rates for the resonance monitors ^{197}Au and ^{96}Zr.

The large drop in temperature on 1/15/09 appears to correlate to the depression in the epithermal flux indicated by the measured epi-cadmium reaction rates for ^{197}Au and ^{96}Zr on that day. Further investigation was done by analyzing the inlet and outlet temperature of the pool water at the approximate times of each measurement. The irradiation of the flux monitors were done between 7:30 AM and 8:15 AM each day. The outlet and inlet pool water temperatures at MURR are recorded in two-hour intervals, beginning at 12:00

110

AM. Therefore, the inlet and outlet temperatures at 8:00 AM each morning were used to estimate the pool water temperature. A plot of the inlet and outlet temperatures as a function of irradiation date is shown in Figure 5.9.
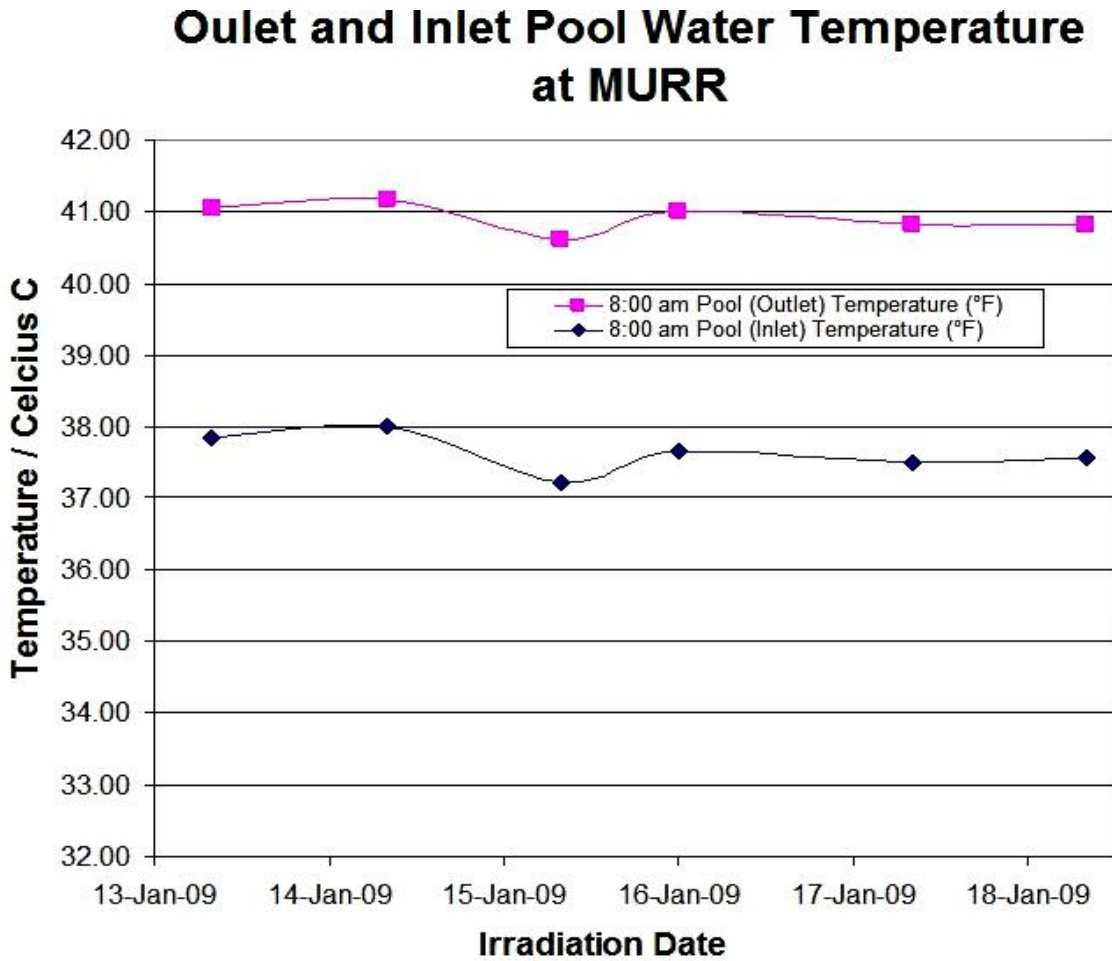
Fig. 5.9 A plot of the inlet and outlet temperatures as a function of irradiation date. The inlet and outlet temperatures reveal a significant drop in the temperature of pool water on 1/15/09 of ~0.7 °C.

Both inlet and outlet temperatures reveal a drop in the temperature of the pool water on the 1/15/09 of ~1°C. Although the change is relatively small, this gives further evidence of a direct correlation between the moderator temperature and the measured reaction rates. However, it is unclear at the moment whether the magnitude of the change in the water temperature can result in the changes observed in the reaction rates for a system the size of MURR. To answer this question, more data is needed from further detailed investigations. In any case, this study has shown that thermal and epithermal reaction rates are not expected to vary more than 2% and 10%, respectively over a given fuel cycle.

Chapter 6 Summary

A novel approach to parametric neutron activation analysis at MURR using state-of-the-art, Monte Carlo *n*-particle transport code MCNP version 5 has been established. In particular, a detailed MCNP5 model of a specific MURR equilibrium core configuration was developed. The model, which was based on precise engineering specifications and continuous-energy neutron data files from ENDF7 and JEFF 3.1, was used to compute the local neutron flux distribution. By coupling the local computed flux distribution to the energy-dependent capture cross-section of a range of interesting nuclides, their intrinsic reaction rates were predicted in irradiation channel ROW2. The MCNP5 MURR core model was benchmarked by measuring the intrinsic (n, γ) reaction rates for a similar set of nuclides in ROW2 using single-element standards.

Results for a set of (n, γ) reaction-rate measurements used in a new approach to INAA at MURR using an MCNP5 model were presented. Intrinsic reaction-rates were obtained from a specific set of dilute single-element standards and were used to benchmark the flux spectrum in a detailed MCNP5 model of the MURR core ROW2 irradiation channel. The measured rates were reproduced on a selected day for two fuel cycles. Comparing the mean (n=3) two-week measured reaction rates to the MCNP5 computed reaction rates shows good agreement, well with within ±5%. In particular, agreement within ±5% is observed for many nuclides with high epithermal sensitivity (e.g., Au-197 and Zr-96) and non-1/v nuclides such as Lu-176 which are otherwise poorly determined by the two-group flux model. The exceptions were the reaction rates for ^{113}In (n, γ) ^{114m}In and ^{79}Br (n, γ) ^{80}Br, where the reaction rates show larger positive

deviations of ~10% and ~20%, respectively, using the latest cross-section data. However, it was concluded that there were discrepancies in the neutron capture cross-section library used since the older cross-section data produce significantly different reaction rate values for ^{113}In (n, γ) ^{114m}In and ^{79}Br (n, γ) ^{80}Br.

The MCNP5 predicted reaction rates were characterized as the universal parameter π_{Theo}, which is defined as a *Au/x* reaction rate ratio for nuclides irradiated in ROW2. The parameter π_{Theo} was used to determine the trace-elemental concentrations for three SRM including bovine liver, coal fly ash and obsidian rock. The results of the MCNP5 predicted trace-elemental concentrations compared to certified concentrations, were consistent with the reaction rate comparisons mostly within ±5%. For comparison, the established k_0-paramteric approach using the modified two–group flux was implemented for the same set samples. For the k_0-paramteric approach, the local flux spectrum was modified by f and α, determined from the cadmium ratio multi-monitor method. Although the predictions of both methods are generally consistent with the elemental concentration and certified concentrations, the MCNP5 shows better agreement for a greater number of elements. In particular, the MCNP5 parametric method proves to be very effective at predicting elemental concentrations for elements such as europium and lutetium, based on the reaction rates of their non-1/v isotopes ^{151}Eu and ^{176}Lu, respectively. These elements are otherwise very difficult to predict with the k_0-paramteric approach.

Chapter 7 MCNP5 Coupled ORIGEN Calculations for Mo-99 Production at MURR

7.1 Molybdenum-99 Production at MURR

Technetium-99m ($t_{1/2}$ = 6 h) is used as an imaging agent in over two-thirds of the nuclear medicine procedures performed in the United States each year. According to a recent National Academy of Sciences report, over 92,000 Mo-99/Tc-99m generators were sold in the U.S. in 2005 supplying 22.9 million doses of Tc-99m [108]. The same report estimates that demand for Mo-99/Tc-99m is likely to grow at 0% to 5% per year over the next five years with the major driver for growth being an increased demand for diagnostic imaging as the U.S. population ages. Yet, while Tc-99m is a critical tool for modern medicine as an imaging agent for numerous diseases including cancer, heart disease, and renal disease, the U.S. has no domestic source for its parent isotope, Mo-99. Because the half-life of Mo-99 is 66 hours, the generators cannot be stockpiled and the generator systems must be replaced on a weekly basis.

Nearly all of the world's supply of Mo-99 comes from five nuclear reactors: NRU in Canada, HFR in The Netherlands, BR-2 in Belgium, OSIRIS in France and SAFARI-1 in South Africa. Until recently, production and worldwide distribution of Mo-99 were reliable. However, a series of events in the industry have recently highlighted the fragile nature of the Mo-99 supply and raised concerns over isotope availability in the U.S. Since January 2007 there have been two serious disruptions to the supply of Mo-99/Tc-99m: a

month-long outage at NRU to fix a back-up system and a six-month shutdown of the HFR when corroded pipes were discovered in the primary cooling circuit.

The recent supply disruptions and the charge in the U.S. Energy Policy Act of 2005 to determine the feasibility of producing Mo-99 without the use of highly-enriched uranium has led us to investigate the feasibility of producing commercial quantities of Mo-99 from low-enriched uranium (LEU) foil targets at the University of Missouri Research Reactor (MURR). The MURR facility was an early producer of Mo-99 throughout the 1970's, into the early 1980's. The isotope Mo-99 was produced through the neutron capture nuclear reaction of Mo-98 in Mo targets. However, the thermal neutron capture cross-section of ^{98}Mo is only 0.13 barns [33] and although MURR has a flux ratio of ~ 30, the total production of Mo-99 through neutron capture is relatively small to meet the present domestic demand. However, the isotope Mo-99 has a six percent (6%) mass yield from the fission of U-235, where U-235 has a thermal-neutron fission cross-section of 587 barns [33].

The Korean HANARO test facility studied the feasibility of using both HEU and LEU targets as primary material for commercial production of Mo-99 [109]. In their report, they acknowledge that HEU is better suited for Mo-99 production based on several findings. In comparison to HEU, it was stated that LEU targets must contain at least five times as much uranium as HEU targets to produce the equivalent amount of Mo-99 [109]. The authors outlined that higher uranium content will also yield larger quantities of waste products since LEU targets contain about 4 times more U-238 than HEU. Consequently, this may cause a problem of Pu-239 contamination in the Mo-99 yield. However, results from the chemical processing of irradiated LEU metal foils at

116

Argonne National Laboratory concluded that Pu-239 contamination of Mo-99 is likely not an issue [110]. However, to comply with the nuclear non-proliferation act the choice of using LEU targets for commercial production of Mo-99 was designated. In this respect, rigorous testing of LEU targets as the primary material for Mo-99 production must be completed before MURR can be a major domestic supplier of ^{99}Mo.

In this study, the feasibility of producing Mo-99 from LEU metal foil targets at MURR was investigated. In particular, neutronic calculations were performed to predict the Mo-99 end of irradiation (EOI) activities from several different irradiation geometries in the graphite reflector region at MURR. A detailed Monte Carlo N-particle transport code (MCNP5) [24] model of the MURR was developed and the ability of the model to accurately predict isotope production rates in the graphite reflector region was verified by comparing measured and calculated neutron-capture activation rates for numerous isotopes. In addition to thermal (1/v) monitors, the benchmarking included a number of isotopes whose activation rates are very sensitive to the epithermal portion of the neutron spectrum. Using the most recent neutron libraries (ENDF/B-VII.0) and JEFF 3.1 [24, 33, 34], the model was able to predict the measured reaction rates to within ±5%. The MCNP5 model was then combined with ORIGEN 2.2 [107] via MONTEBURNS 2.0 [106], to calculate production of Mo-99 from LEU metal foils. The MONTEBURNS simulations were also benchmarked against a 5-gram annular LEU target irradiated for 140 hours.

7.2 LEU Target Designs

Nickel Foil
Thickness = 15 microns (0.0006 in)
(Outer red)

LEU Foil
Thickness = 125 microns
(Inner orange)

A

A

Inner Tube (Type 3003 Al)
O.D. = 27.99 mm (1.102 in)
I.D. = 26.42 mm (1.040 in)

Outer Tube (Type 3003 Al)
O.D. = 30.15 mm (1.187 in)
I.D. = 28.22 mm (1.111 in)

Foil Gap
~ 11.4 mm
(~ 0.45 in)

Section A - A

mm
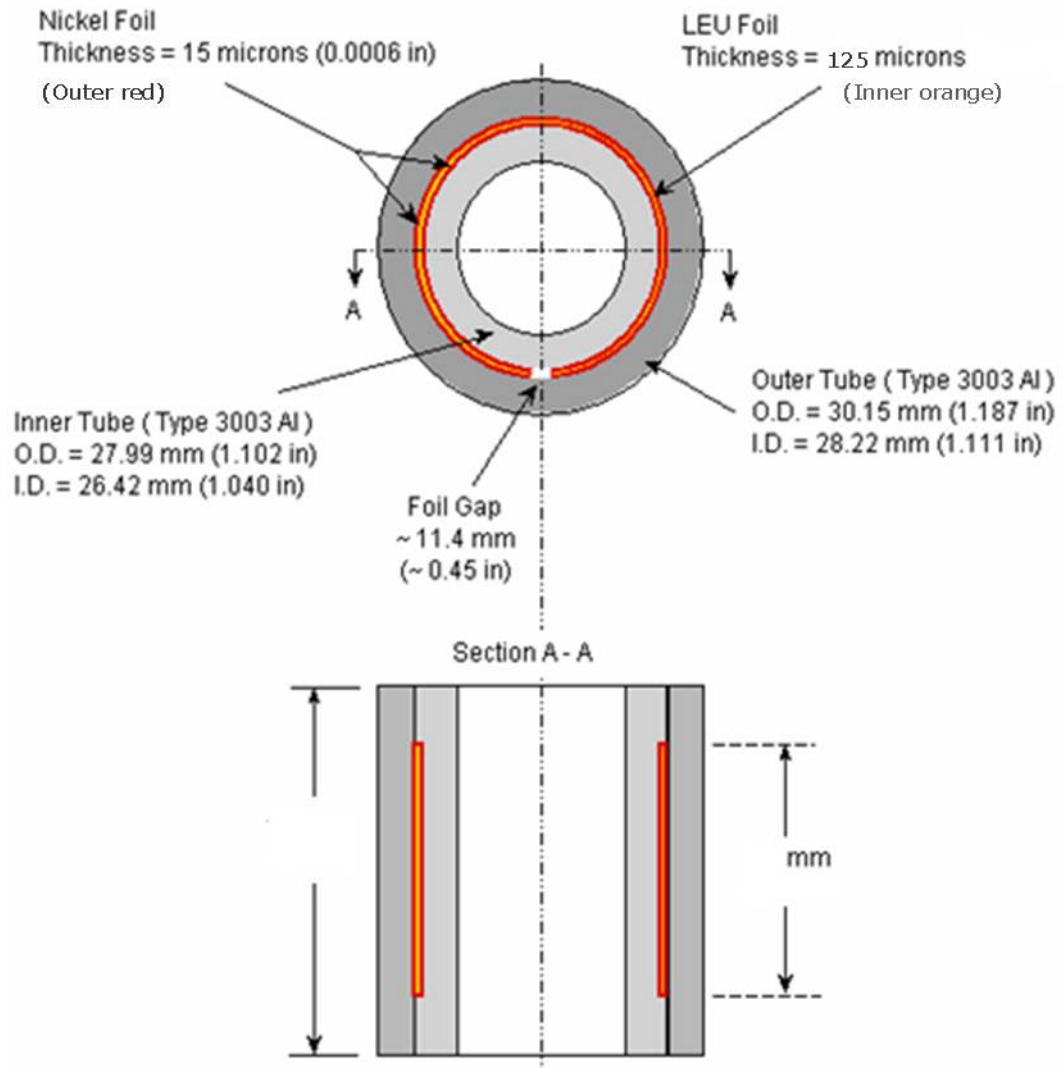
(Not Drawn to Scale)

Fig. 7.1 (a) A design schematic of LEU annular target geometry from LEU-modified Cintichem process [111].

118
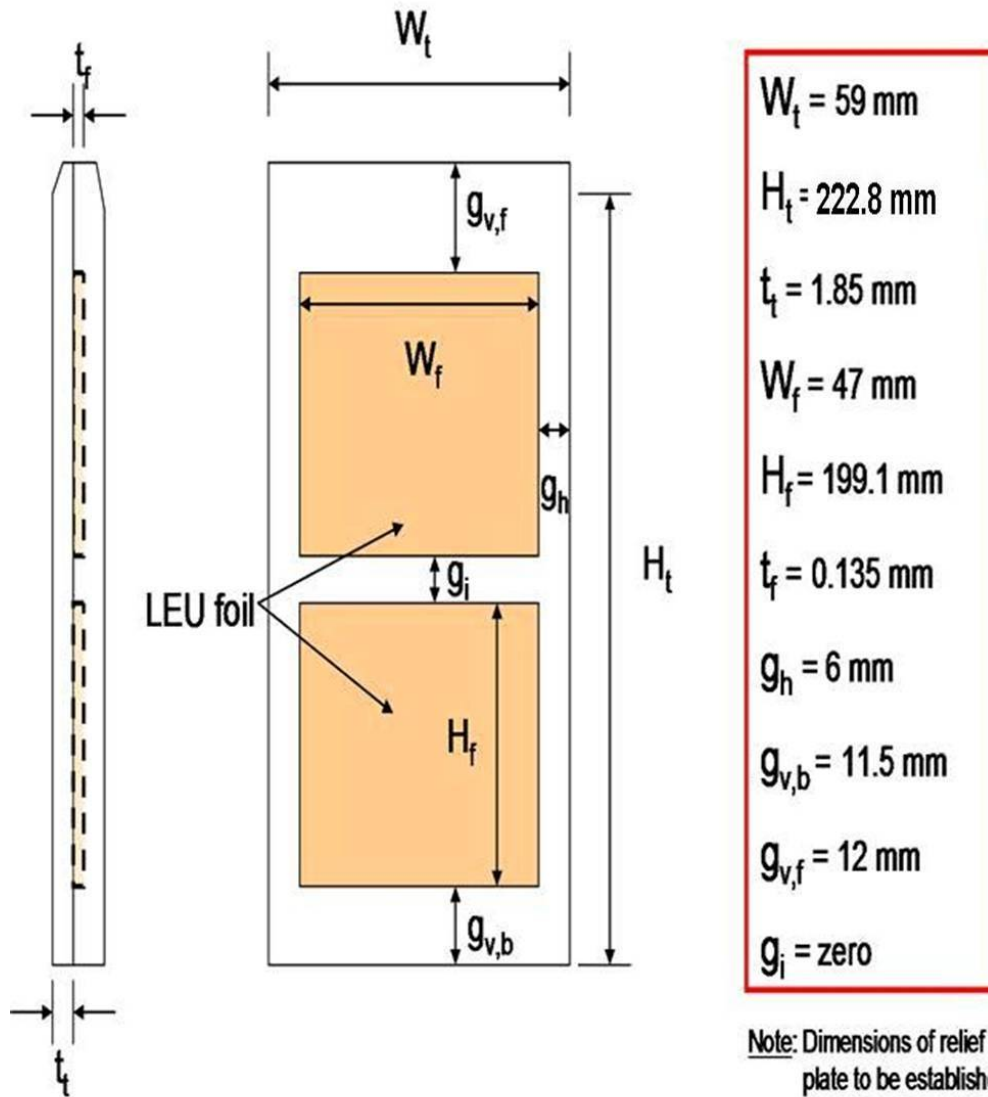
Plate geometry

Fig. 7.1(b) A design schematic of the LEU target plate (plate) geometry from a MURR conceptual design.

Two LEU target geometries were modeled (Figure 7.1). In the annular geometry, which is based on the LEU-modified Cintichem design [111], the LEU foil is sandwiched

between two 15 μm thick nickel fission-fragment retention foils. The nickel-uranium sandwich is held between an inner and outer 3003-series aluminum tube. In the flat plate geometry, the nickel-uranium sandwich is held between two aluminum plates. The annular LEU foil is 125 μm thick and contains 30 grams of uranium whereas the flat plate LEU foil is 135 microns thick and contains 24 grams of uranium.

7.3 The MCNP5 Models

7.3.1 MCNP5 Models for Multiple LEU Target Geometries

Based on the previous benchmarking validations the MCNP5 model was used as the foundation to predict the Mo-99 production from LEU targets. The model was modified so that the N1 graphite wedge is used as a site for irradiating LEU targets (see Figure 2.1). To optimize the total Mo-99 production from one graphite wedge, a number of irradiation geometries were studied in the N1 graphite wedge. The annular geometry has a total of three different irradiation arrangements, where each arrangement has six individual LEU targets. The plate geometry has two different irradiation arrangements, each having eight individual LEU targets. The panels in Figure 7.2 illustrate the various arrangements for annular targets and plate targets in the N1 graphite wedge position. Individual annular and plate LEU targets were modeled in detail. Figure 7.3 shows a close-up model of an annular target in its irradiation position. The annular targets are situated in rows of irradiation channels on radii of 28 cm, 34 cm and 38 cm from the center of the core (see Figure 7.2). The plate targets are stacked in one of two orthogonal arrangements in a rectangular irradiation channel. The center of each of the rectangular

channels is located about 32 cm from the center of the core. The flux distribution for each target was studied to understand the shadowing effect in the different irradiation geometries.

Annular Geometry 1
Water channel OD: 3.4 cm
First row: 28 cm *Radius*
Second row: 34 cm *Radius*
Six targets, **1 per channel**
30 g LEU per Target

Annular Geometry 2
Water channel OD: 3.4 cm
First row: 28 cm *Radius*
Second row: 34 cm *Radius*
Third row: 38 cm *Radius*
six targets, **1 per channel**
30 g LEU per Target

Annular Geometry 3
Water channel OD: 3.4 cm
First row: 28 cm *Radius*
Six targets, **2 per channel**
30 g LEU per Target

Plate Geometry 1
Water gap 0.635 cm (1/4 inch)
First Plate: 28 cm (*from origin*)
Last Plate: 35 cm (*from origin*)
8 targets, 24 g LEU per Target

Plate Geometry 2
Water gap 0.635 cm (1/4 inch)
All Plates: ~30 cm (*from origin*)
8 targets, 24 g LEU per Target
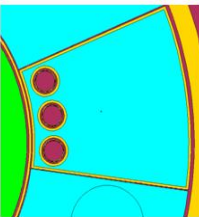
Total LEU mass in Annular Geometry: 180 g

Total LEU mass in Plate Geometry: 192 g

Fig. 7.2 Panels showing the different irradiation geometries for the annular and plate irradiation geometries in the N1 graphite wedge

15 μm thick
Nickel fission-product retention barrier

Modeled annular target in water channel

Close-up showing the LEU foil (white) /air (orange) interface sandwiched between the aluminum-alloy clad (yellow)
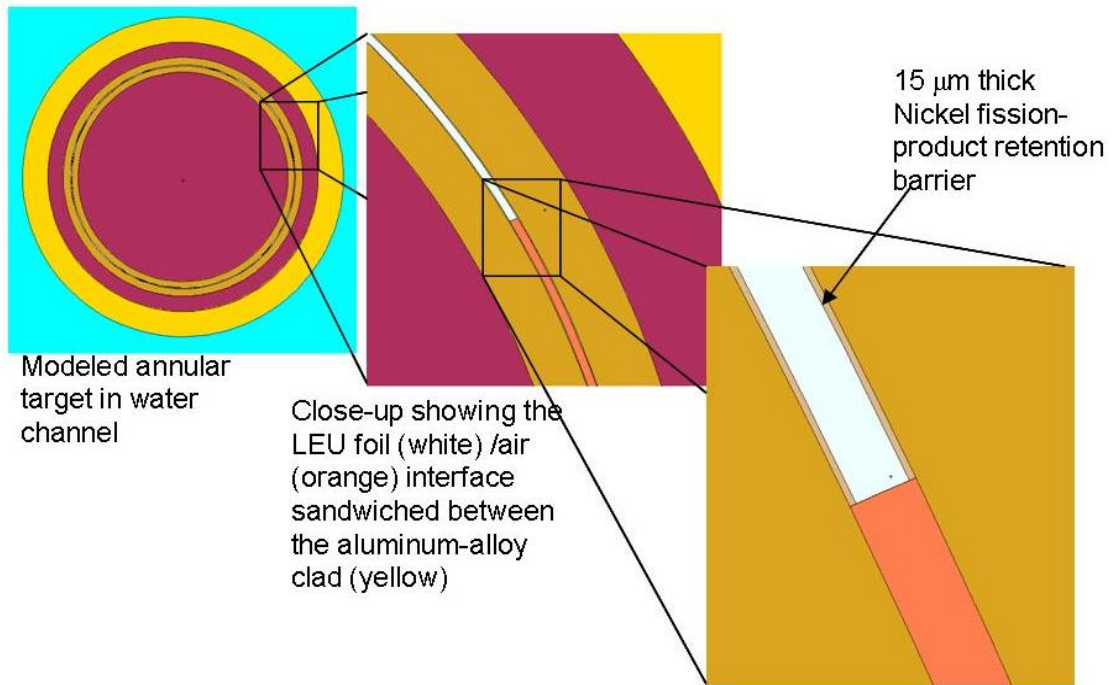
Fig. 7.3 This figure shows the detail modeling of an annular LEU target in its irradiation position.

7.3.3 Static MCNP5 Flux Calculations

To examine the neutron fluxes within the LEU targets, kcode calculation were performed for each irradiation geometry using equilibrium-core configurations. The kcode input parameters were set at 50,000 particles per cycle, for 1000 active cycles for each calculation.

Thermal Flux $E_n < 0.5$ eV
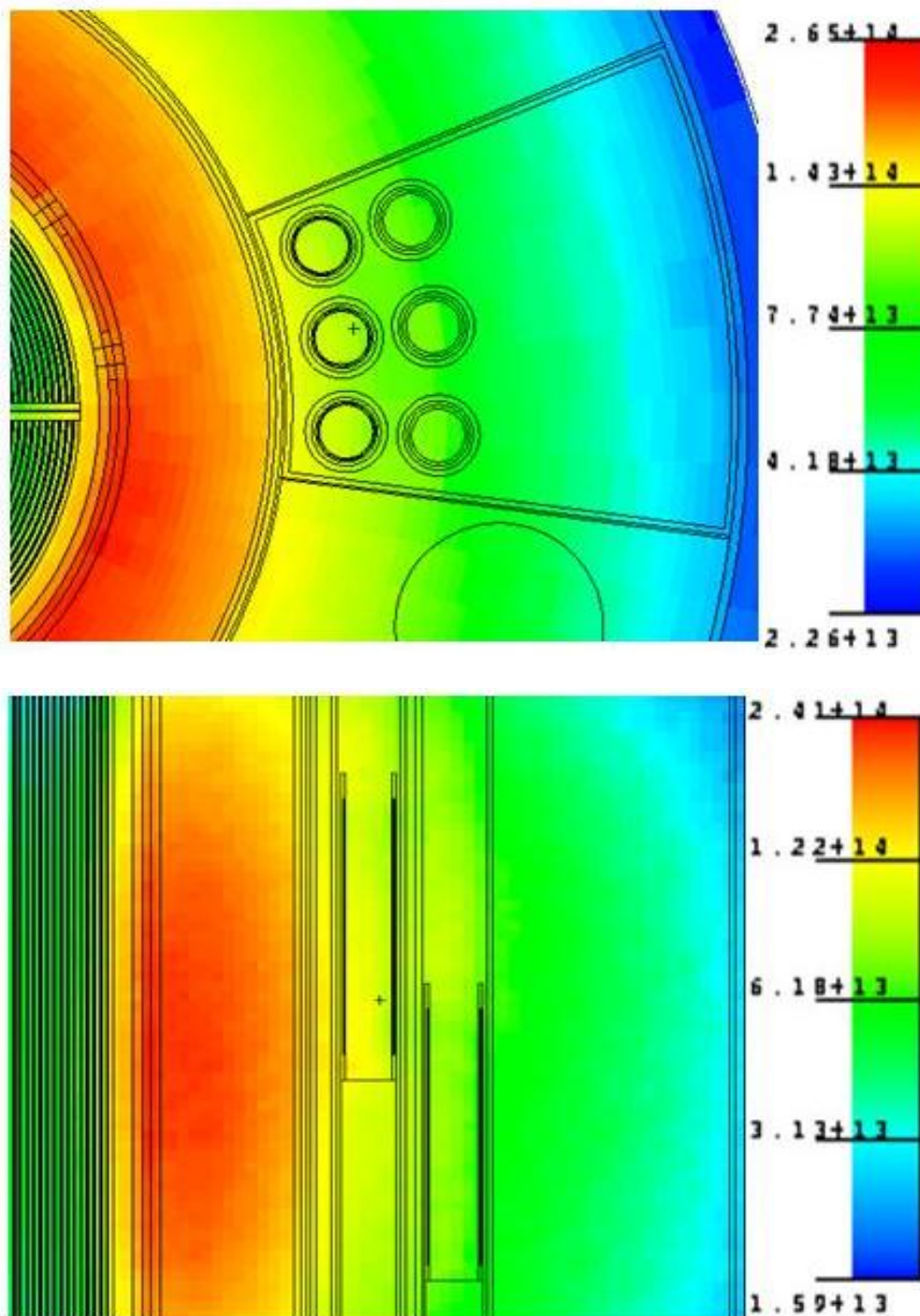
Fig. 7.4 (a) Panels showing the radial and vertical thermal flux profiles in annular geometry 1.

The color-enhanced contour plots in the panels of Figure 7.4(a) reveal the vertical and radial calculated thermal flux profiles for annular geometry 1. The colored key on the right of each panel indicates the absolute flux intensities. The top panel shows the radial profile while the bottom panel describes the vertical profile.

The flux spectrum, which is plotted on a unit lethargy scale for each target in annular geometry 1, is presented in Figure 7.4 (b). The peak-thermal flux is highlighted for each row of targets and the different colors represent the flux spectrum for individual targets. A distinct reduction in the total flux is observed for the targets in the second row. This is likely to be due to the radial drop off in the total flux. To minimize flux suppression (shadowing) in the second row due to the targets in the first row, the second row is vertically staggered lower than the first row. The fast-neutrons produced from fission in the targets are seen as the enhanced peak on the high-energy end of the spectra. Enhancement in the thermal flux is possible; these thermal neutrons must originate from a neighboring target since the slowing distances to thermal energies for neutrons is ~6 cm in water and 18 cm in graphite [18]. Based on this, the first row of targets may experience a slight enhancement in the thermal flux due to neutrons originating from the second row. Figures 7.5(a) and 7.5(b) through 7.8(a) and 7.8(b) present similar MCNP5 fluxes profiles and spectra for annular geometry 2, annular geometry 3, plate geometry 1 and plate geometry 2.

Flux shadowing is more likely to impact the second and third row targets in annular geometry 3 and, even more so for plate geometry 1 where the targets are stacked directly behind each other. The flux-shadowing effects are observed in their radial and vertical flux profiles. The arrangement with the least flux shadowing effects is observed in

annular geometry 3 (see Figure 7.6(b)). In this arrangement targets are stacked directly above each other, for each irradiation channel to minimize flux shielding due to other targets. However, the peak thermal flux is slightly less than peak thermal fluxes in both annular geometries 1 and 2 for the same irradiation position.   This supports the speculation that the inner targets gain an enhancement in the thermal flux due to the outer targets.
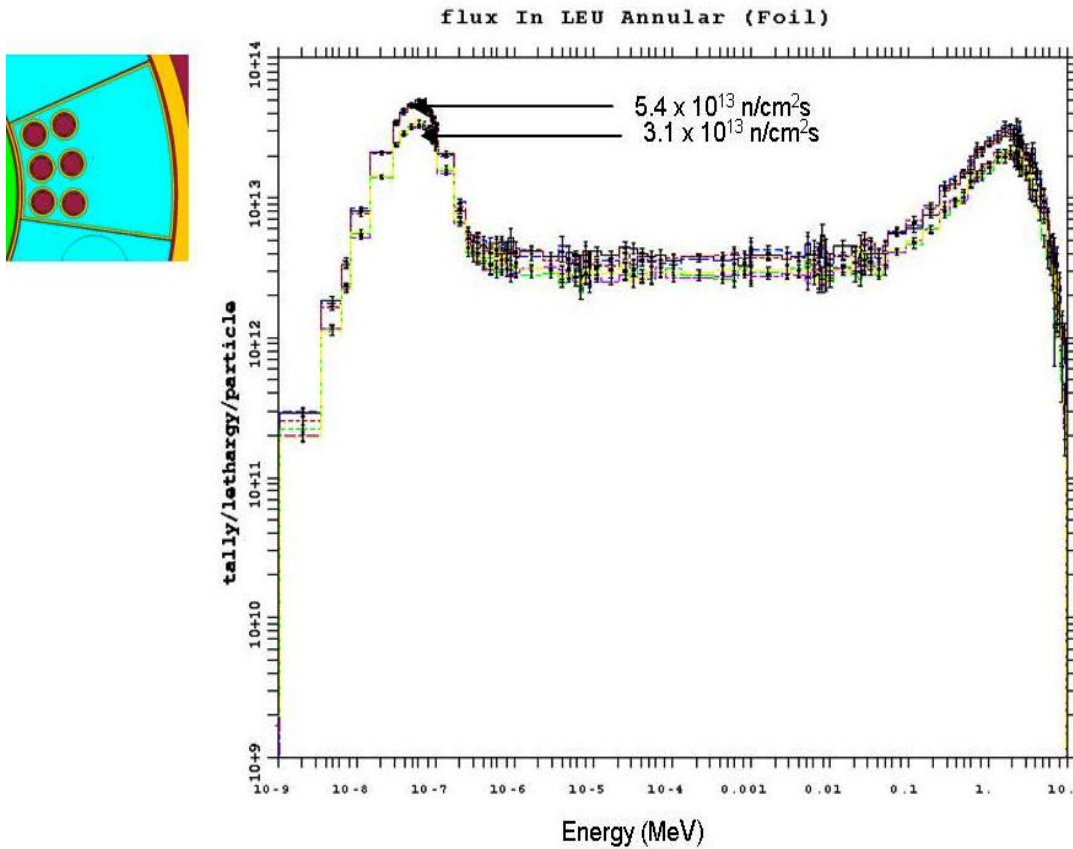
Fig. 7.4(b) Flux spectra for the targets of annular geometry 1 represented by different colors.

Thermal Flux $E_n < 0.5$ eV
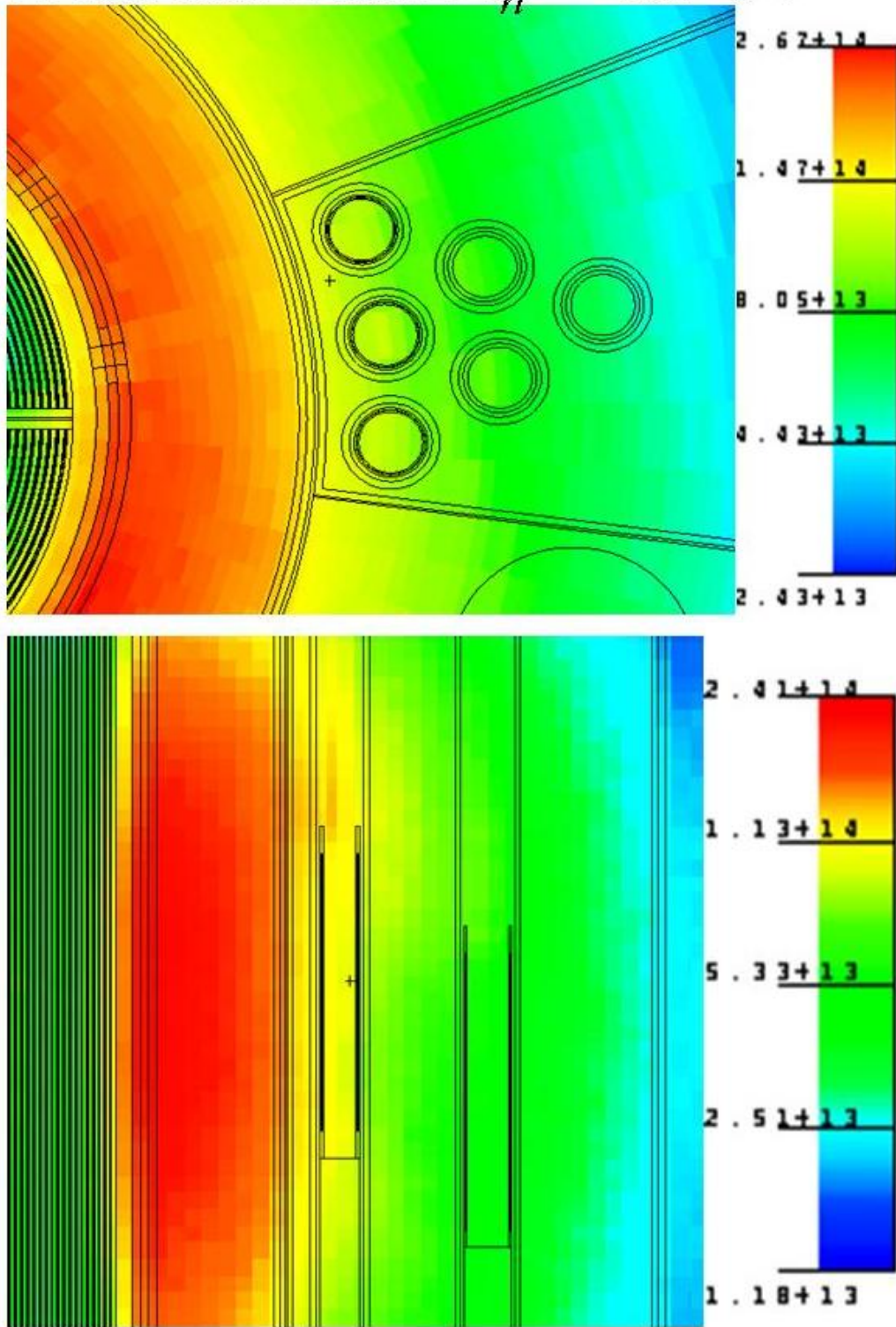
Fig. 7. 5(a) Radial and vertical thermal flux profile for annular geometry 2
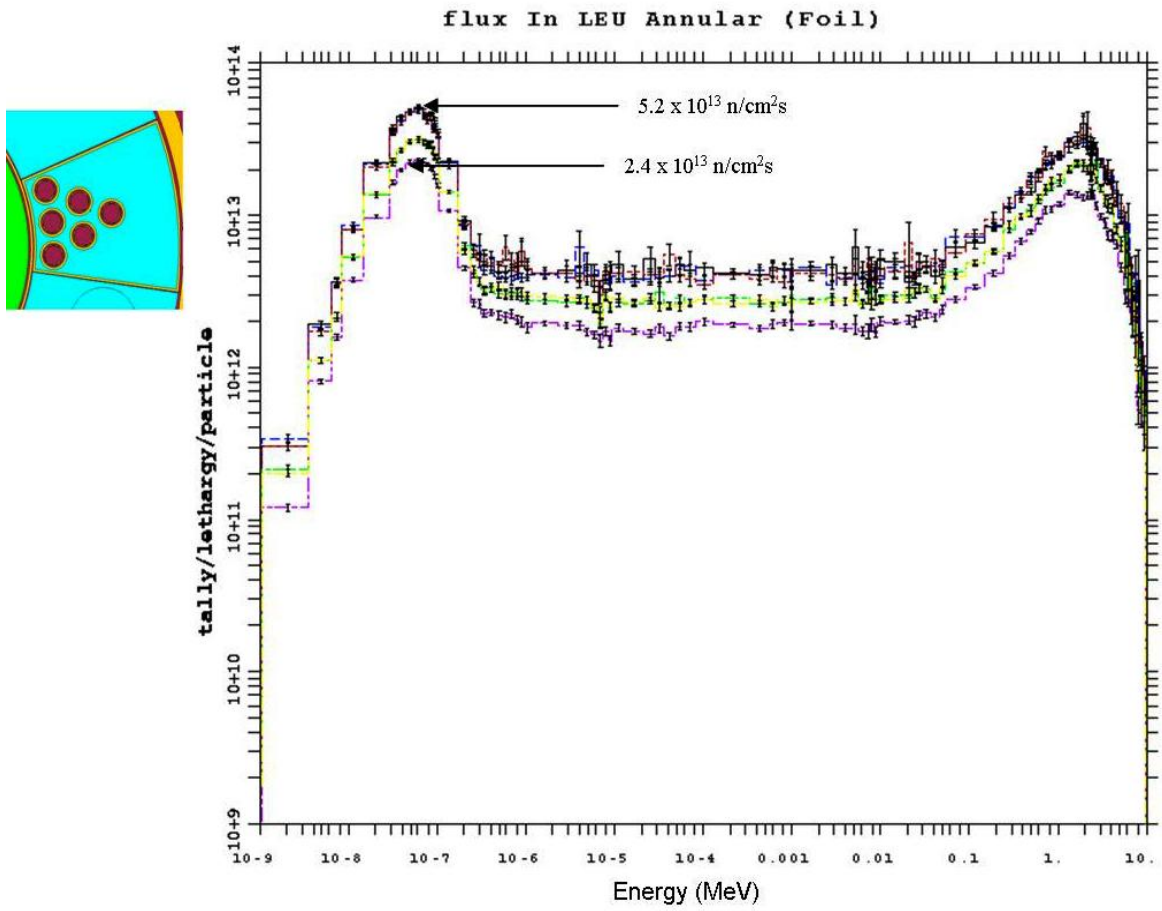
Fig. 7.5(b) Flux spectra for the targets in annular geometry 2

127

Thermal Flux $E_n < 0.5$ eV

	2.68+14
	1.49+14
	8.27+13
	4.59+13
	2.55+13

	2.59+14
	1.35+14
	7.09+13
	3.71+13
	1.94+13
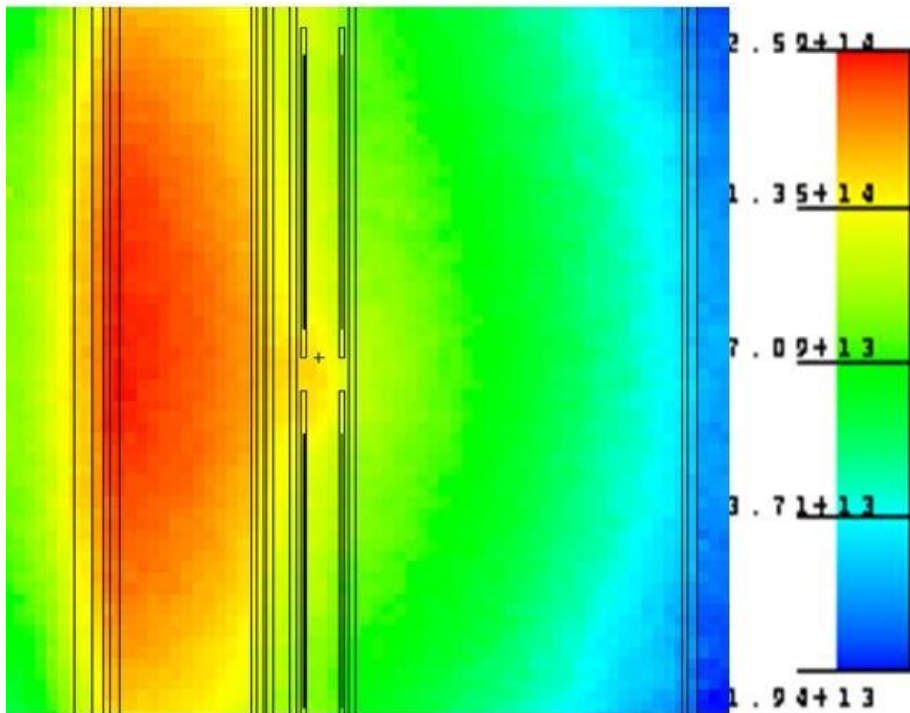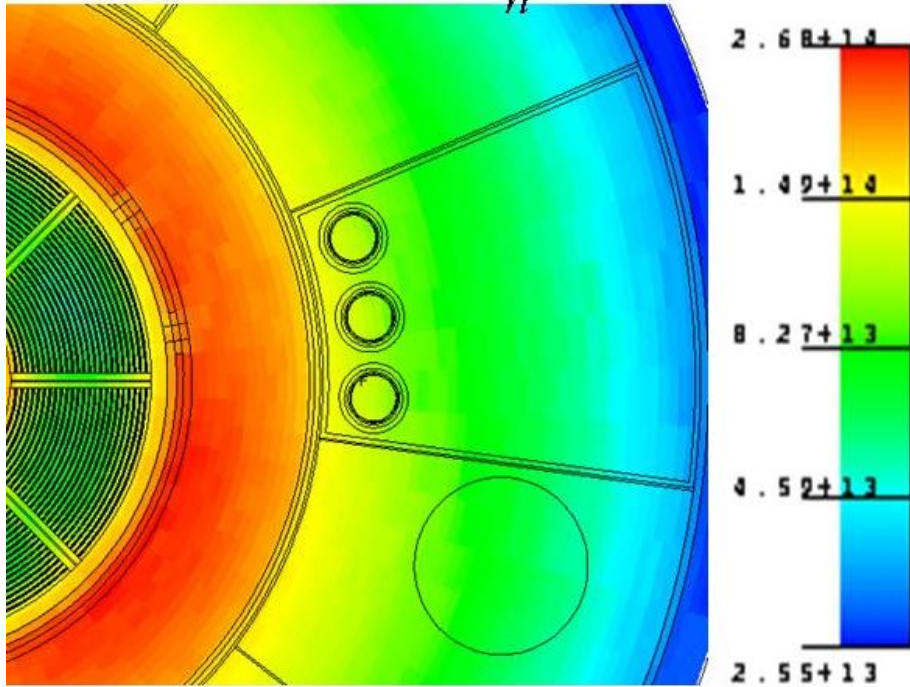
Fig. 7.6(a) Radial and vertical thermal flux profile for annular geometry 3

128
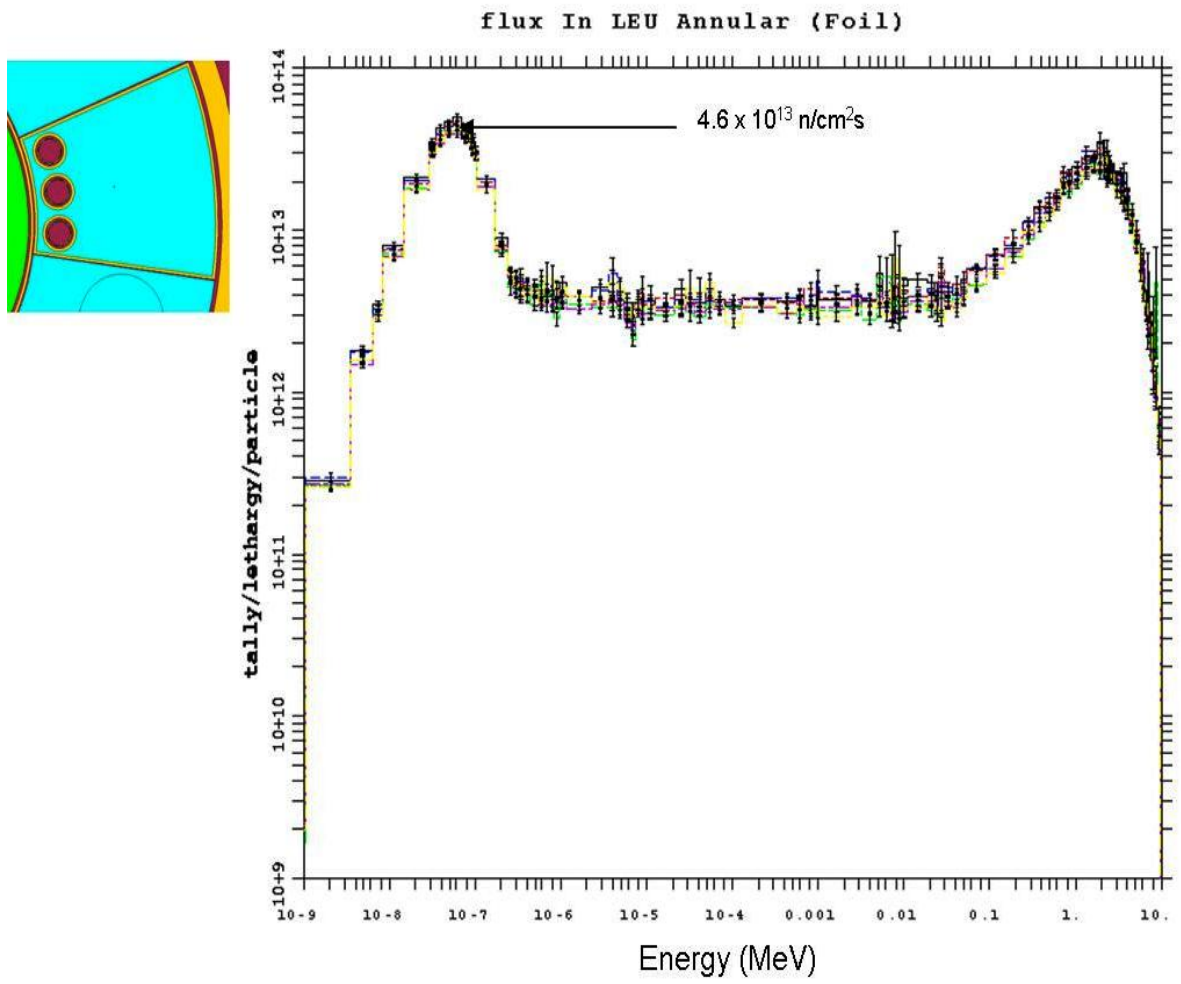
Fig. 7.6(b) Flux spectra for the targets in annular geometry 3.

129
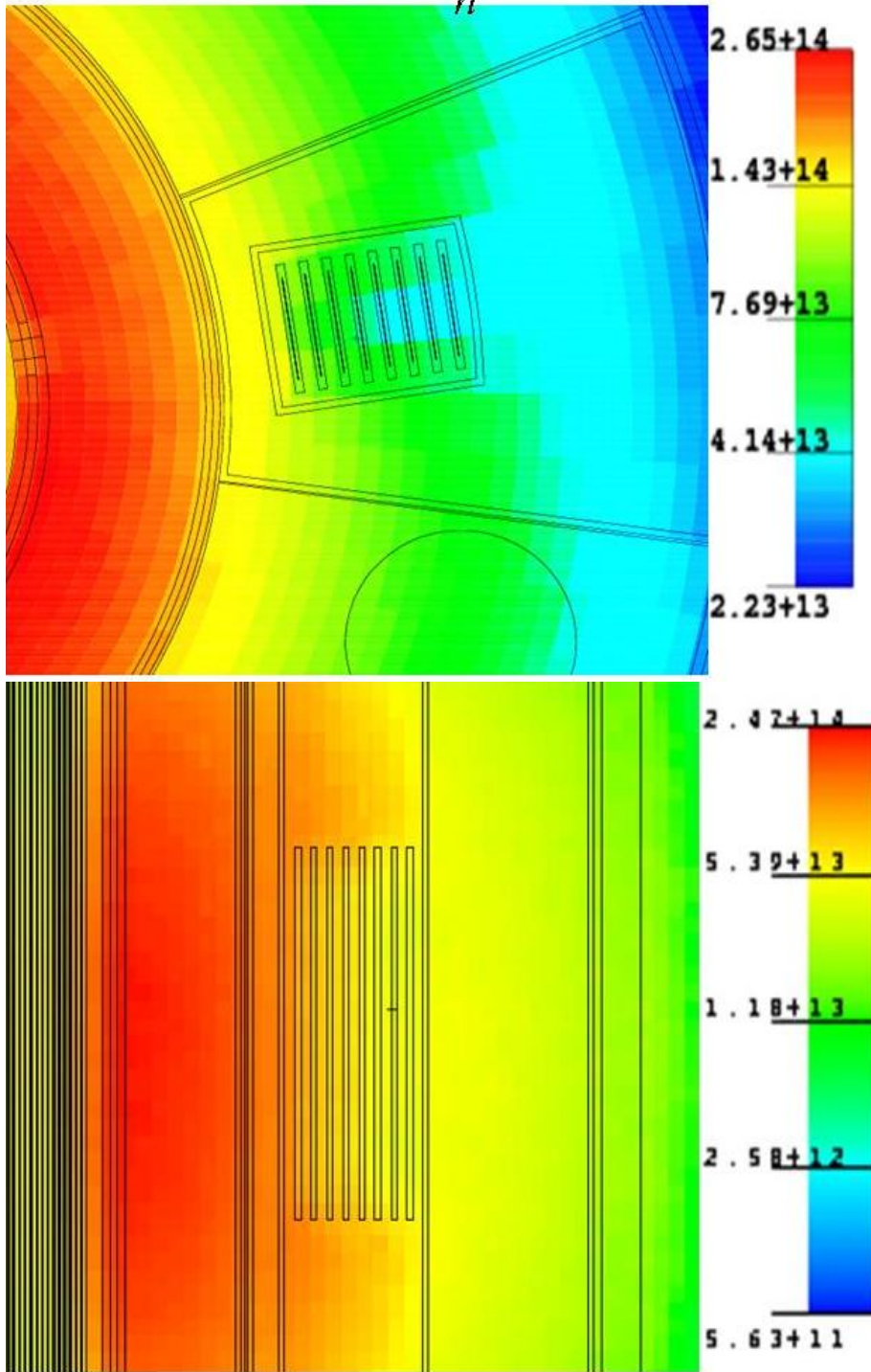
Fig. 7.7 (a) Radial and vertical thermal flux profiles for plate geometry 1

130
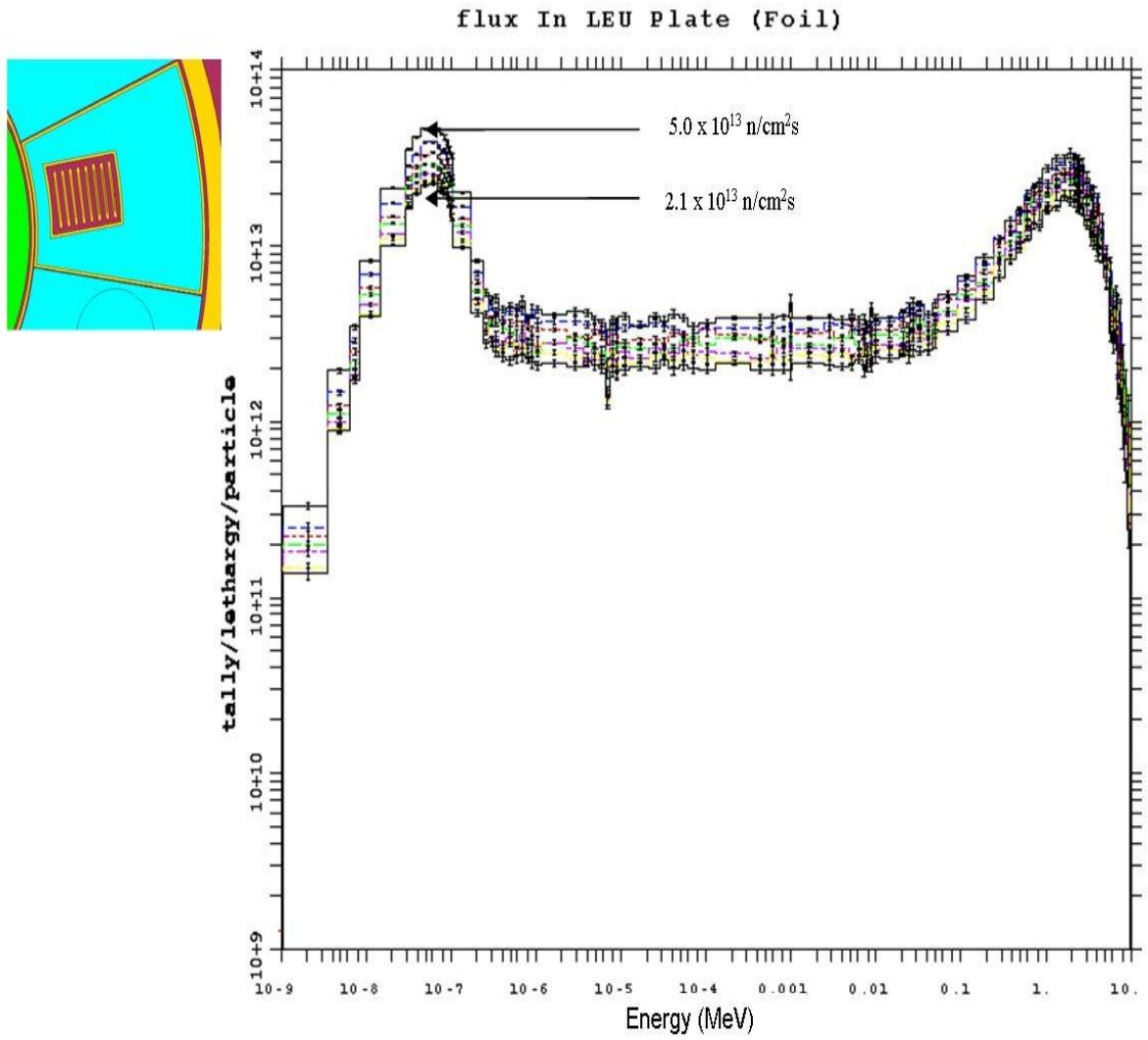
Fig.7.7(b) Flux spectra the for targets in plate geometry 1

Thermal Flux $E_n < 0.5$ eV
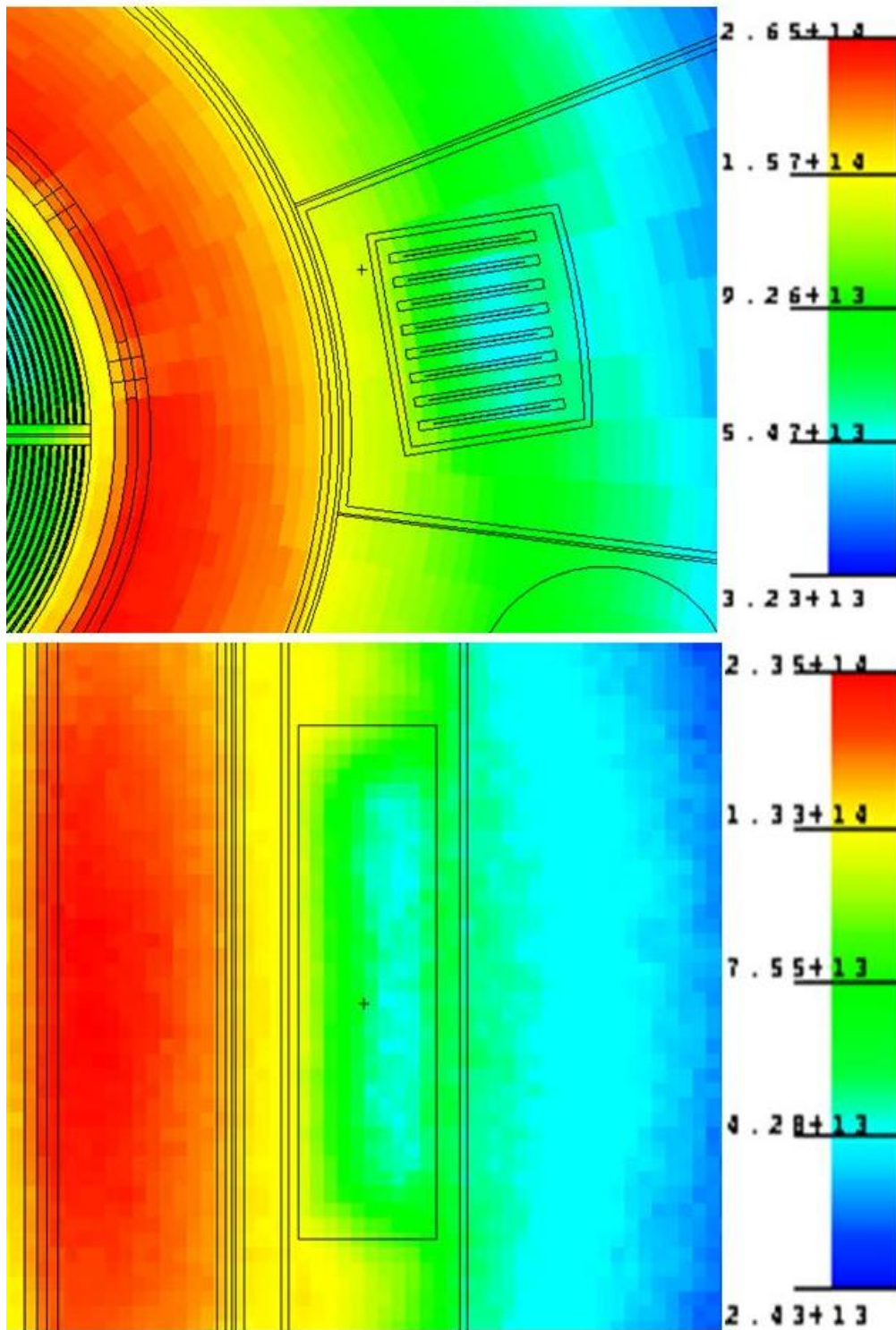
Fig. 7.8(a) Radial and vertical thermal flux profile for plate geometry 2.
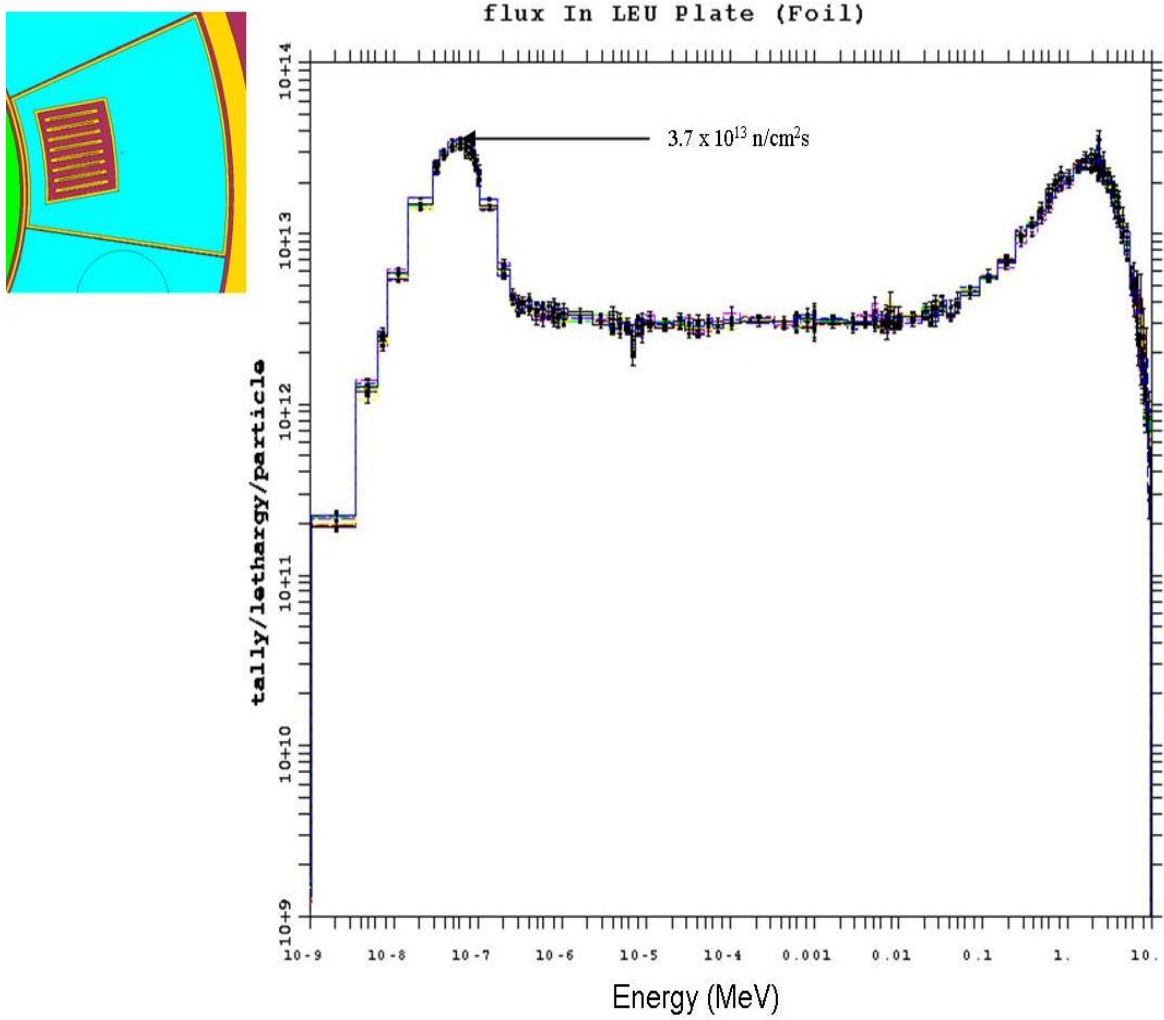
Fig. 7.8(b) Flux spectra for the targets in plate geometry 2.

7.4 Mo-99 Predictions at MURR

7.4.1 Benchmarking MCNP5 – ORIGEN 2 Coupled Calculations

An estimation of the EOI Mo-99 activity can be done using a system of time-dependent Bateman equations [13]. These equations can be used to account for the total production and depletion of Mo-99 during irradiation through all available reaction channels, (see Figure 7.9). However, to solve the complete set of Bateman equations analytically for this system is tedious and time consuming.
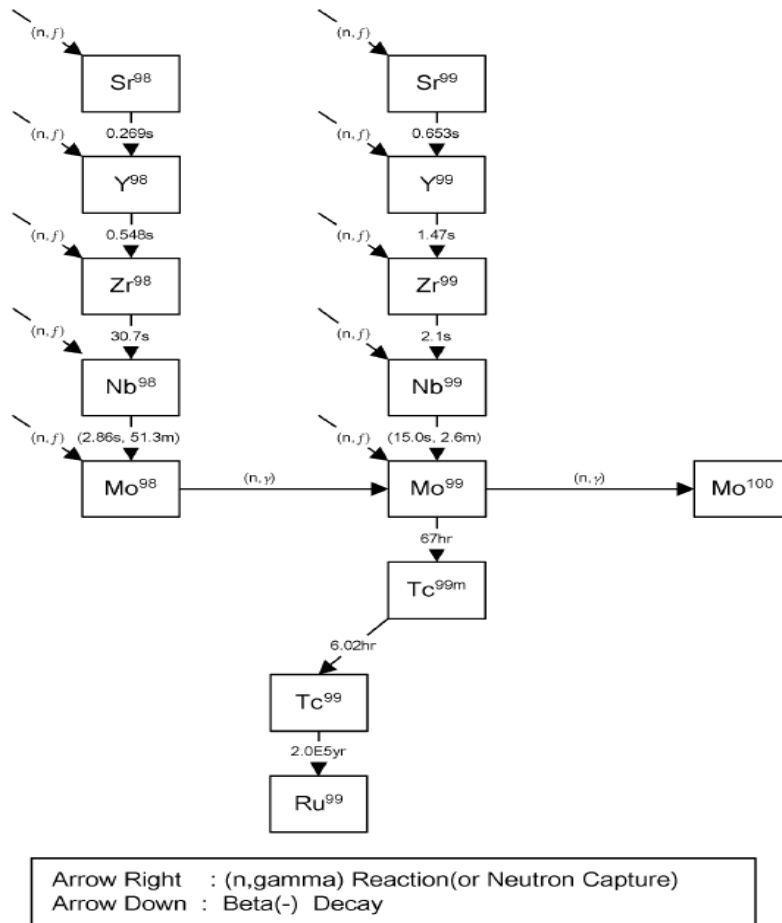
Fig. 7.9 Figure 4 taken from Ref. [109] showing the production total scheme for Mo-99 from fission of U-235.

In addition, solving this set of equations does not accurately account for the changes in LEU absorption and fission cross-sections that occur as uranium foil burnup continues. To simulate the cross-sectional changes in the LEU target, along with solving the time-dependent Bateman equations to accurately predict Mo-99 activity, the combinatory use of a neutron transport and isotope production-depletion code is necessary.

In this work, the code ORIGEN 2 [107] was coupled to MCNP5 models to accurately predict Mo-99 activity at MURR. ORIGEN 2 is an isotope production–depletion code used to study the nuclear burnup processes using the time-dependent Bateman equations. ORIGEN 2 can be supplied a flux value to perform burnup calculations at a point based on its default one-group cross-section libraries, but these computations are not very accurate. However, ORIGEN 2 can use the accurate fluxes and one-group cross-sections generated by a detailed MCNP5 model when the two codes are coupled. For this study, the burnup code MONTEBURNS 2.0 (MB) [106] was used to couple ORIGEN 2.2 to MCNP5. For a selected material, MB first passes accurate fluxes and one-group cross-sections from MCNP5 (generated from the kcode calculation mode) to ORIGEN 2. ORIGEN 2 uses the one-group flux and cross-sections to predict isotope depletion-production tables for the material being burned up. MB uses these tables to create an updated material definition then passes it back to MCNP5. This cycle continues for a designated amount of steps until the end of the burnup simulation.

To benchmark the MB simulation, data from an experiment irradiating a single 5-gram annular LEU target in irradiation channel K-2 was used. The centerline of K-2 is located adjacent to two Topaz irradiation cans at approximately 8 cm from the nearest and 25 cm from the furthest Topaz can. Each Topaz can is permanently lined with a 50

135

mm-thick layer of cadmium. The experiment was done to test the chemistry of the modified Cintichem process [111] for Mo-99 production at MURR. The Cintichem process is a four-stage method involving isotope production and separation from irradiating uranium targets with neutrons. Here, with the first stage being irradiating the target, the chemistry of the target must be suited for the sequence of the next three stages steps that follows which involves acid dissolution, precipitation and purification of the isotope of interest. For the irradiation stage, the LEU target positioned approximately 33 cm above core centerline and was irradiated steadily for 140 hours. In a separate measurement, an aluminum target containing dilute cobalt and gold flux-wires was irradiated in the same position to determine the average flux by flux-unfolding methods [112-114]. The aluminum target was designed to replicate the dimensions of a 30-gram annular LEU target.

The 5-gram LEU irradiation experiment was modeled by MCNP5 in a steady-state core configuration. The burnup simulations were performed using MB. Here, Figure 7.10 shows a detailed MCNP5 model of the irradiation experiment.
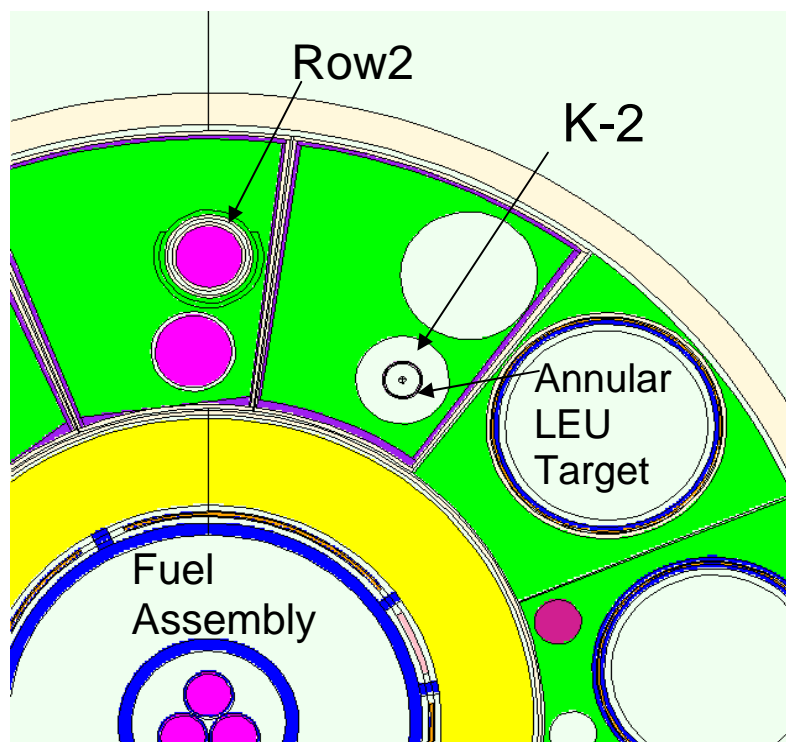
Fig. 7.10 The MURR core MCNP5 model showing the simulation experiment for the irradiation of a 5-gram annular LEU target in the K-2 irradiation channel.

For the MB simulations, three separate models of a 5-gram annular LEU target irradiated for 140 hours in the K-2 position were performed. Since MB does not report uncertainties for the end of irradiation activities, the kcode particle statistic for each of the three burnup simulations were different. This was done to check the integrity of the MB predictions. The kcode parameter for kcode calculation of MB simulations one, two and three were set at 30,000, 5000, and 1000 particles per cycle, respectively, each for 1000 active cycles. The number of MB cycles (outer steps) was set to six and an output table was requested for the isotope ^{99}Mo. A separate static MCNP5 kcode calculation, the average

flux in the 'mock' LEU target was computed in K-2 irradiation position. This was done so that the calculated flux in the irradiation position can be directly compared to the measured flux using Co-Al flux monitors. Here, the kcode parameters were set at 30,000 particles per cycle for 1000 active cycles.

Results for the measured and MCNP computed average thermal and epithermal flux in K-2 are listed in Table 7.1. The results for the front and back of the target, in addition to the average value for both measurements and MCNP5 predictions are shown. There is a 15% difference between the predicted and the measured thermal flux values. The differences between the computations and the measurements indicate a different flux spectrum for K-2 in which the measurements report a softer (more thermal) spectrum than the calculations.

Section of Annular Target	Measured Φ_{therm} n/cm^{2}s	MCNP5 Φ_{therm} n/cm^{2}s
Front (towards core)	1.65×10^{13}	1.40×10^{13}
Back	1.21×10^{13}	1.02×10^{13}
Average	1.43×10^{13}	1.21×10^{13}

Table 7.1 A list of the results of the MCNP5 computed flux compared to the measurements of the average thermal fluxes in the target position of the K-2 irradiation channel.

138

Experiment	EOI ^{99}Mo Curies (Ci)	Thermal Flux at Target
MB Simulation 1	13.6	8.85×10^{12} n/cm^{2}s
MB Simulation 2	13.2	
MB Simulation 3	14.2	
Measured	13.3	
WIMS (at CCHEN)	13.2	9.18×10^{12} n/cm^{2}s

Table 7.2 The end of irradiation Mo-99 activities in Curies after 140 hours compared to the measured end of irradiation Mo-99 activity for a 5-gram annular target. A comparison calculation was also done using the WIMS criticality code system at the CCHEN reactor in Chile. The integrated flux at the target is also reported.

The results in Table 7.2 show the EOI Mo-99 activities for a 5-gram annular target after 140 hours of irradiation for the three MB simulations in comparison to measurement for the recovery process. An increased in the kcode statistics generally improves the results. However, this effect is small (i.e., ~ 3%). If the simulation with the greatest kcode statistics is used (MB Simulation 1), then there is a 2.3 % deviation from the measured value. If the worst case simulation is used, the deviation is 6.6%. Either way, the results suggest excellent agreement between the MB simulation and measurement. For further validation, a 5-gram metal foil target irradiation simulation was done at the CCHEN reactor in Chile using the WIMS criticality code system [115] for 140 hours to predict the EOI Mo-99 yield. The CCHEN result reported in Table 7.2 also shows excellent agreement with the measured value (i.e., less than 1% difference) and between the MURR model prediction using results from MB simulation 3 (i.e., ~3% difference). Figure 7.11 shows the calculated saturation activity curve for Mo-99 for MB simulation 1 over the 140-hour irradiation.
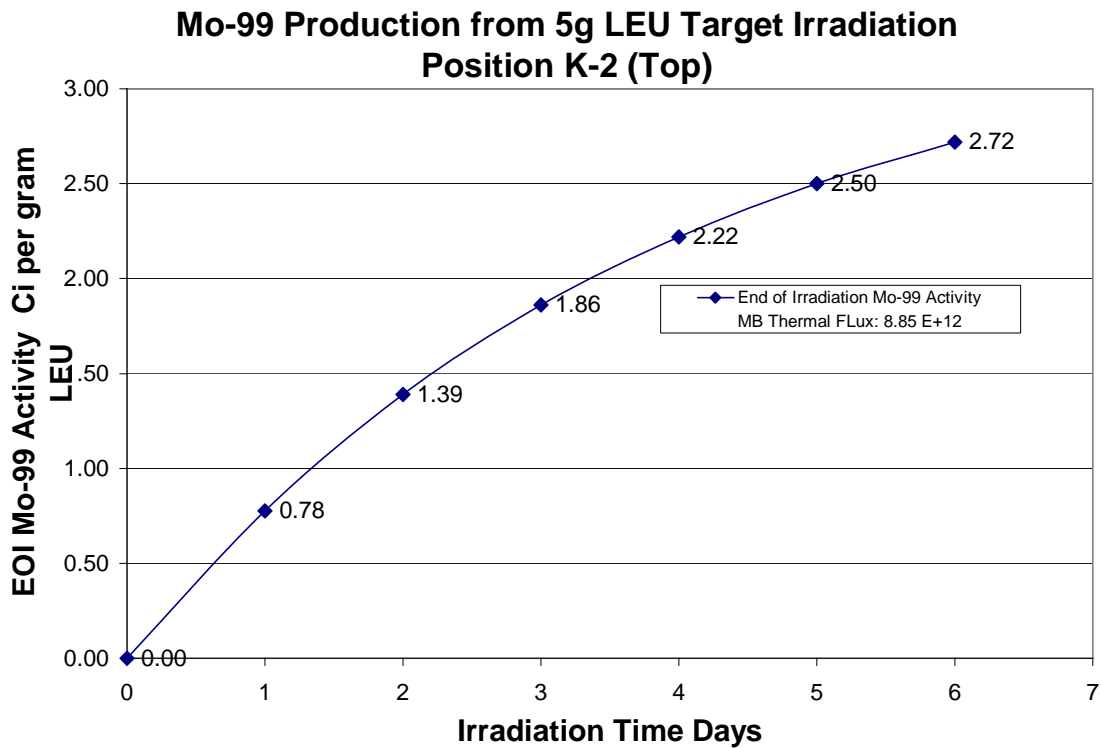
Fig. 7.11 The saturation production curve for Mo-99 from a MB calculation (MB simulation 1) of a 5-gram annular LEU fuel target was irradiated for 140 hours.

Most of the fission events in the LEU fuel target (and consequently the Mo-99 yield) depend on the intensity of the thermal flux at the target position due to large the U-235 thermal fission cross-section. However, the integrated thermal fluxes reported in Table 7.1 are higher than the values in the presence of a LEU target (see Table 7.2). Since the thermal (microscopic) absorbance cross-section alone for uranium is over 600 barns, significant flux suppression at the target position is expected. Nonetheless, it is reasonable to focus mainly on the thermal portion of the spectrum where U-235 fission is concerned. In light of this, comparing of variance between the thermal flux data (Table 7.1) and the Mo-99 activity data (Table 7.2), the deviation between the predicted thermal

140

flux and the measured thermal flux is 5 times greater than the deviation between the predicted and measured data for the Mo-99 EOI activity. This indicates a concerning inconsistency.

One possible explanation for this measured "softer neutron spectrum" may be a positioning error of the flux monitors during irradiation. Although, there is no conclusive evidence of this, since K-2 is located adjacent to a Topaz can lined with cadmium (a strong thermal-neutron absorber), small variations in the target position can impact the measured flux significantly. This is because the flux-gradient between the target (in K-2) and the cadmium lining of the nearest Topaz can is expected to fall off rapidly. Another cause can be related to the unfolding method of determining the flux. Flux-unfolding techniques as such require an initial guess that influences the final results [15, 116, 117]. Therefore, a poor initial guess can lead to poor results. In addition, in these methods the thermal flux is unfolded using the capture cross-section's point value at 2200 ms^{-1} (0.025 eV). However, the thermal (1/v) portion for the capture cross-sections should be averaged over the entire Maxwell-Boltzmann thermal neutron spectrum. This introduces a correction factor of 0.128 to the evaluation at 2200 m/s [18]. Also, the Maxwell-Boltzmann neutron spectrum is not ideal (i.e., harder), therefore the actual average thermal cross-section is even less [18].

For unfolding the epithermal flux which is less important here, the resonance integral (see equation 1.11), which is based on an ideal 1/E epithermal flux spectrum, is used. This is used because deviations from the ideal epithermal spectrum in K-2 cannot be determined from the information provided by the flux monitors. Therefore, it is likely that an unfolded epithermal flux will be incorrect. This is also true even for very precise

methods of experimentally determining the epithermal flux such as using epi-cadmium reaction rates as described by Rogus et al [113]. Furthermore, the thermal and epithermal fluxes are simultaneously unfolded from the same bare (or integrated) reaction rates. Therefore, if there is an inconsistency in unfolded thermal flux, it is expected to also be present in the epithermal flux. However, because the epithermal flux is much smaller than the thermal flux, its sensitivity to any inconsistency is greater. One way in which the speculation can be rationalized is using the capability of ORIGEN 2 to independently predict activities using the default (fission) cross-section libraries. However, these libraries are not reliable for precise calculations since many of the files are outdated [118] and are listed as the value of the fission cross-sections at 2200 ms^{-1}. Corrections for the average thermal fission cross-section can be estimated to be slightly over 50%.

7.4.2 LEU Target Thickness Optimization

The thicknesses of the LEU foils were optimized by considering the flux-averaged neutron self-shielding factor. The flux-averaged neutron self-shielding factor G_{ave} for LEU can be expressed as

$$G_{ave} = \frac{\int_0^\infty \phi^*(E)\Sigma_a(E)d(E)}{\int_0^\infty \phi(E)\Sigma_a(E)d(E)} \quad where \; \Sigma_a = \sigma_{cU235} + \sigma_{cU238} + \sigma_{fU235}\cdots \tag{7.1}$$

where $\phi^*(E)$ is the real energy-dependent flux spectrum in the LEU target, $\phi(E)$ is the unperturbed energy-dependent flux spectrum, and $\Sigma_a(E)$ is the total energy-dependent

absorption cross-section (including fission) for ^{235}U and ^{238}U. Similar expressions can be used to calculate thermal G_t and epithermal G_{epi} self-shielding factors separately. For a G_{epi} calculation for LEU, in addition to changing the integration limits (i.e., taking the lower limit to be the cut off energy 0.5 eV and the upper limit at least 0.1 MeV or greater) the cross-section may be replaced by a complex flux-averaged resonance absorbance cross-section. Fission neutrons are produced within the LEU foil with an average energy of 2 MeV and at a rate of 2.5 neutrons per ^{235}U fission [18]. For any material where neutron transport is concerned, elastic potential scattering is the main process where fission neutrons are moderated to lower energies [44]. For ^{238}U, (which is the major component of LEU) the resonance integral for potential elastic scattering is 593 barns [33]. The resonance integral for ^{238}U is also quite large (i.e., 275 barns [33]). However, this value may vary due to the production of epi-cadmium neutrons within the fuel target which can vary the shape of the 1/E epithermal flux spectrum. Epi-cadmium neutrons are those with energies greater than the chosen cadmium cut-off energy. Here, the thermal cut-off energy is chosen to be 0.44 eV [119]. However, almost all fissions within the LEU target foil are due to the thermal neutrons. With this in mind, we will focus on the thermal and effective (or flux–averaged) self-shielding calculations for the LEU targets.

Equation 7.1 cannot be solved analytically; therefore, several MCNP5 models using an SDEF source [24, 32] and the ENDF/B-VII.0 [33] neutron data for uranium were developed to calculate effective G factors for various foil thicknesses. Here, the absorbance (capture) cross-sections of fission-products are not included. The methodology using MCNP5 to deduce self-shielding factors has been used to develop

143

universal thermal and epithermal self-shielding factors for various flux monitors [68, 69, 90, 91]. However, it was not used for LEU fuel targets as such. A series of eight LEU targets was modeled as 1 cm discs with thicknesses varying from 25 to 500 microns. The SDEF neutron source was modeled such that each LEU disc is irradiated in an isotropic neutron flux field. Here, the shape of the flux distribution was obtained from the computed flux spectrum at K-2 irradiation position (see Figure 7.10). For thermal self-shielding calculations, the integration limits for equation 7.1 were set from zero to the cadmium cut-off energy 0.44 eV. For the flux-averaged self-shielding calculation, the upper integration limit in eq. 7.1 was set to 10 MeV (essentially infinity for a thermal reactor spectrum).
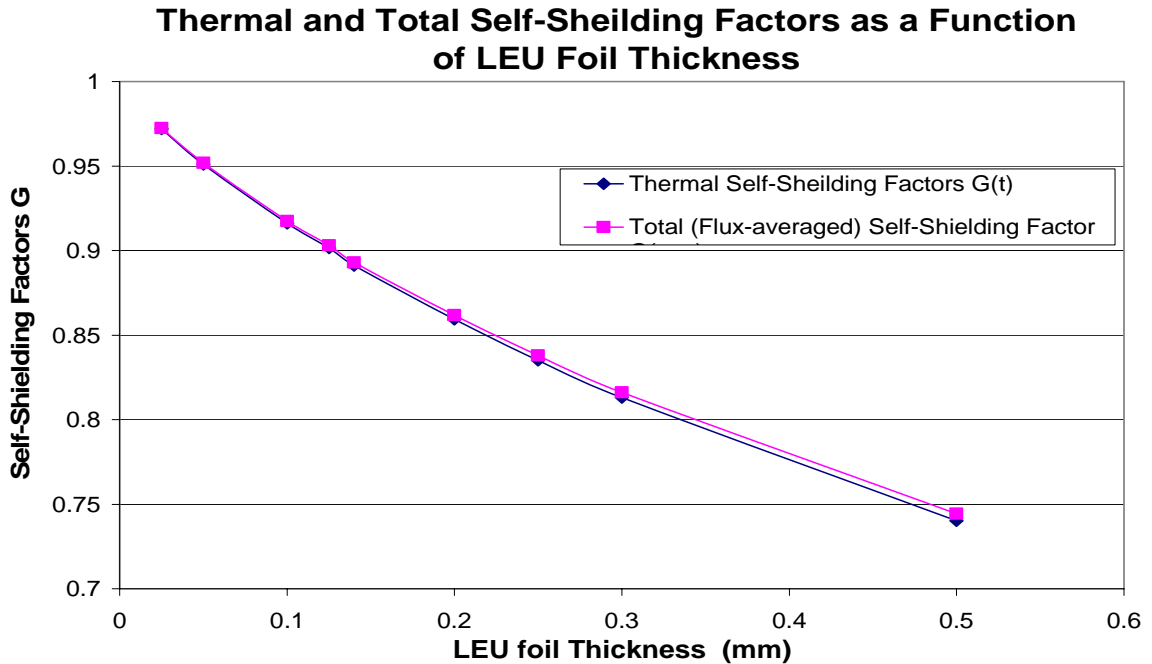
Fig. 7.12 A plot of the MCNP5 calculated G_t (diamonds) and G_{ave} (squares) for different thicknesses.

Figure 7.12 shows a plot of the MCNP5 calculated G_t and G_{ave} for the different LEU foil thicknesses. The plot reveals little to no difference between G_t and G_{ave}. Also, as expected, thinner foils have less self-shielding effects. However, an increase in G is not directly proportional to a decrease in foil thickness. Extrapolating the lower end of the plot, the foil thickness with no self-shielding effects is one which is infinitely thin and is obviously not practical. In the manufacturing process for LEU foils, producing foil thicknesses below 125 microns is problematic.

Next, a MB simulation was done to study the self-shielding effects while the target is being irradiated. Although in small quantities, fission products such as ^{135}Xe and ^{151}Sm have notoriously large thermal neutron capture cross-sections (i.e., at 2200 m/s) of values 2,647,600 and 15,170 barns, respectively, as reported in the ENDF-B/VII.0 data [33]. Therefore, the total effective absorbance cross-section of LEU is expected to change with the production of these fission-products. For this investigation, a LEU target thickness of 135 microns and its corresponding static (i.e., no burnup) G factors were used. The length of the irradiation was set for 140 hours. The kcode parameters for an equilibrium core were set at 10,000 particles per cycle for 1000 active cycles. Plots of the material's effective capture cross-section, the effective fission cross-section, the sum (fission + capture) and the fission-capture ratio as functions of irradiation time are presented in Figure 7.13.

The plot of the effective capture cross-section shows an increase to an equilibrium value. This is consistent with the production curve for the fission-product Xe-135. A plot of the fission-to-capture ratio suggests that an increase in the effective capture cross-section is larger than the magnitude of the changes in the effective fission cross-section.

145

The plot of the effective fission cross-section shows very slight variation over the irradiation period. However, one may expect its value to decrease since fissile material is being steadily utilized. However, the burnup percentage of initial fissile U-235 is small (i.e., 3%) over 150 hours. In addition, the fissile isotope Pu-239 is bred through the fast (n, γ) reaction of ^{238}U (the major component of the foil) which then beta decays into Pu-239. The thermal fission cross-section alone for Pu-239 is over 740 barns and its fission resonance integral ~300 barns [33]. Therefore, the production of Pu-239, even in small quantities, can influence the material fission cross section. The sum of the material capture and fission cross-section represents the total absorbance cross-section. The plot of this sum shows an increase to an equilibrium value.

The change in the total absorbance cross-section during irradiation must be reflected in the self-shielding factors G_{ave} and G_{therm}. Figure 7.14 shows a plot of the change in G_{ave} as a function of irradiation time. Time zero refers to G_{ave} based on the foil thickness of 125 μm and without any burnup effects (see Figure 7.13). Figure 7.14 shows the effective self-shielding factor as a function of irradiation days in time for a 135-micron thick LEU target. There is an initial dip in the plot of G_{ave} just after irradiation begins. However, the value of G_{ave} increases to an equilibrium value that is slightly less than the initial value. One speculation is that this dip may be related to the initial burnup effects within the foil moments after irradiation begins. As equilibrium is established, the value of G_{ave} is stabilized to a value slightly less than the initial value. Overall, the effective self-shielding factor shows only a slight decrease of ~3 % over the entire irradiation period.

Fig. 7.13 Plots of the LEU material capture, fission, sum of fission and capture, and fission-to-capture ratio as a function of irradiation time in days.

Effective (Flux-averaged) Self-Shielding Factor For 5-g 135 micron LEU Target For 140 Hours Irradiation period
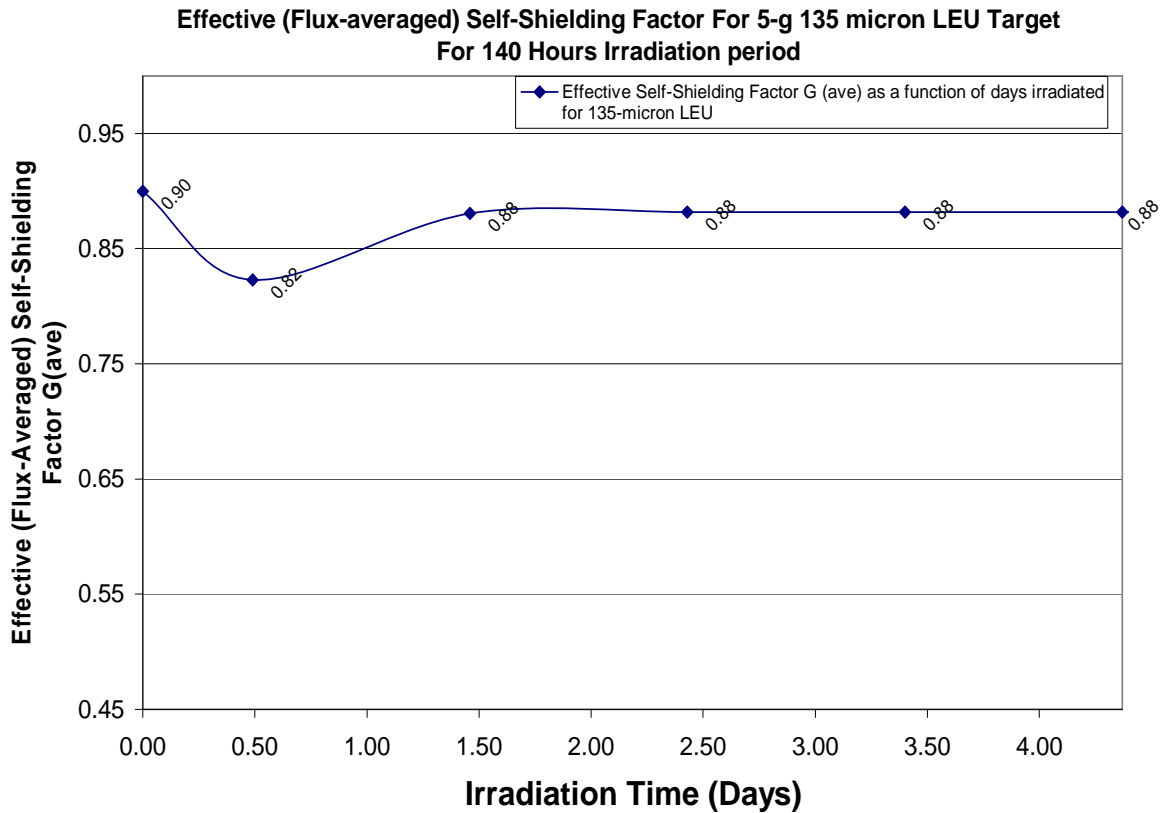
Fig. 7.14 A plot of the effective self-shielding factor as a function of irradiation days in time for a 135-micron thick LEU target.

7.4.3 Mo-99 Predictions for Multiple Target Arrangements

Based on excellent agreement between the benchmarking MB simulation and experimental data, the MB Mo-99 predictions were done for all irradiation geometries shown in Figure 7.2. The objective of the MB simulations was to maximize the specific activity of Mo-99 that can be produced from a single graphite wedge position at MURR. For each MB simulation, the kcode calculations were for 20,000 particles per cycle, for 1000 active cycles. The total irradiation time was set for 6.25 days and the Mo-99 activity

was output after every 1.4 days. The thicknesses for the annular targets were set to 125 µm while the plate targets were set to 135 µm. The total mass of LEU irradiated in each annular arrangement was 180 grams while the plate arrangements each had a total of 192 grams. The saturation activity curves for Mo-99 are presented for the annular geometries in Figure 7.15 and for the plate geometries in Figure 7.16, as a function of irradiation time in days.

Calculated EOI ^{99}Mo yield per gram of LEU for t_{irr} = 150 hours Annular Geometries
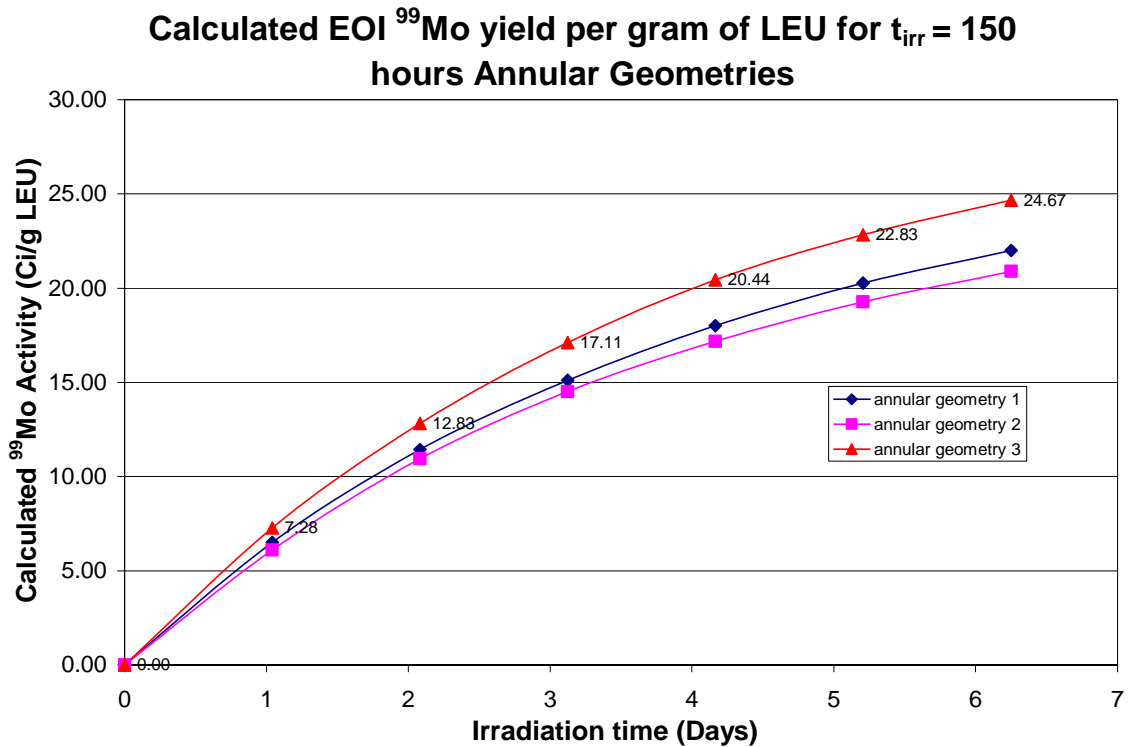
Fig. 7.15 Saturation curves for Mo-99 specific activity for annular geometry 1 (diamonds), 2 (squares) and 3 (triangles). The 1.4-day Mo-99 activities are only shown for annular geometry 3.

The activity curves in Figure 7.15 and in Figure 7.16 represent the average Mo-99 activity that each target arrangement produces at 1.4-day increments over a total of 150

hours of irradiation. In Figure 7.15, annular geometry 3 (triangles) shows the highest

average specific activity (EOI = 24.67 Ci/g of U), while the annular geometry 2 (squares)

shows the least for these arrangements (EOI = 20.89 Ci/g U). This is not very surprising

since these trends are consistent with trends of the calculated thermal peak fluxes from

MCNP5.

In Figure 7.16, plate geometry 2 (crosses) shows the higher average specific activity

(EOI = 17.60 Ci/g of U), while the plate geometry 1 (circles) is the slightly lower of these

two arrangements (EOI = 16.46 Ci/g U). Again, this is not very surprising since the

trends observed between the activity plots are consistent with trends of the average

calculated thermal peak fluxes from MCNP5 for these arrangements.

Calculated EOI ^{99}Mo Yield per gram of LEU for t_{irr} = 150 hours Plate Geometries
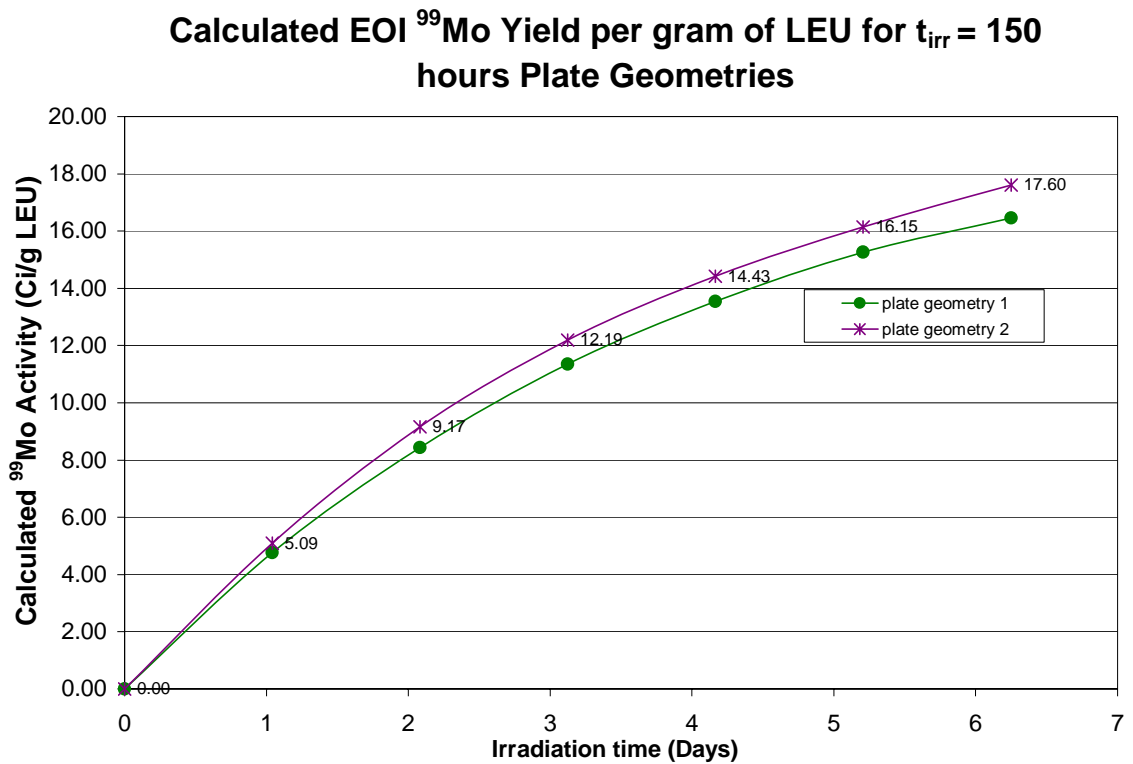
Fig. 7.16 Saturation curves for Mo-99 specific activity for plate geometry 1 (circles) and 2 (crosses). The 1.4-day Mo-99 activities are only shown for plate geometry 2.

Over all, the annular arrangements show a significantly higher Mo-99 production yield than the plate arrangements by ~ 30%. This is also consistent with the predicted thermal flux values. Using the annular geometry 3 arrangement, the maximum six-day EOI curies of Mo-99 from one graphite wedge is predicted to be 4500 Ci. The MURR is attempting to produce a target of 3000 six-day (~24,000 EOI) curies of Mo-99. This can be met if the geometry 3 arrangement is repeated in at least four similar graphite wedges at MURR.

7.5 Conclusions and Future Work

An MCNP5 model of MURR was developed and benchmarked against activation rates for a number of isotopes in both dilute, single-element standards and two NIST standard reference materials. The benchmarking isotopes included those that are sensitive to epithermal activation and those that are sensitive to thermal activation. The measured and calculated values showed excellent agreement.

The MCNP5 model was then coupled to ORIGEN 2 to predict the Mo-99 activity from the irradiation of a 5-gram LEU foil following a 140 hour irradiation. The model predicted an end of irradiation activity of 13.6 Ci. The measured EOI activity was 13.3 Ci.

A total of five MCNP5 models were created where each possesses a different LEU target irradiation geometry. Each model was coupled separately to ORIGEN via MB to predict the six-day EOI Mo-99 activity. The results show that 4500 six-day EOI curies of Mo-99 could be produced from one graphite wedge with six 30-g LEU annular targets.

In order to fully certify the MCNP5 parametric INAA as the standard methodology to be used at MURR, the variability of the parameter π_{MCNP} for the particular irradiation position must be completely understood. In essence, a careful investigation must be done to fully understand the major causes of variations in the local flux distribution. Because variations in the flux also affect the local reaction rates for isotope production, in this case Mo-99 from the fission of LEU foils, an investigation as such is quite necessary to predict accurate yields. There are a number of factors that can lead to changes in the flux distribution at an irradiation position. However, under normal operating conditions of a reactor, one of the most prominent factors is thought to be changes in the fuel's macroscopic absorbance cross-section.

Two preliminary investigations were carried out to study the variability in the local flux distribution in ROW2 based on changes in the fuel's macroscopic absorbance cross-section due to refueling and fuel burnup during a fuel cycle. Using sensitive epithermal flux monitors (Au and Zr) and pure 1/v thermal flux monitors (Ti and Mg) the variation in the flux distribution was observed between refueling and during a fuel cycle. Initial results show that variations in the thermal flux are likely to be small since the RSD of the mean n=7 thermal reaction rates was less than 3%. However, a significantly larger RSD observed for the mean n=7 epithermal reaction rates of (8%) implies larger variations in

the epithermal flux. A detailed MCNP5 coupled ORIGEN burn up simulation testing the different fuel loadings shows that the variations are not an effect of the refueling. Initial speculations are that the variations are related to temperature of the secondary coolant (water).

A similar experimental approach was done for the flux stability during a fuel cycle. Initial results indicate small variations in the thermal reaction rates (less than ~2%). The results are slightly larger for the epithermal (or epi-cadmium) rates, but the RSD is still within 8%. However, the indicative trends for the thermal and epithermal flux are similar to the fuel cycle observations. Further investigation suggests a correlation between the temperature of the pool-water surrounding the core and the variations in the reaction rates.

At this point the evidence is still rather inclusive and more detailed investigations are needed. However, plans are made for further investigations. One approach is to extend the measurements for a much longer period of time (e.g., over one year) or artificially regulating the (pool) water temperature between upper and lower safety limits during normal steady-state operations. Another approach is to create several detailed MCNP5 models of the MURR core to study a range of water temperatures between 294K and 363K. For each temperature setting, the appropriate changes in the water density and $S(\alpha, \beta)$ thermal scattering laws must be made. Although, there are limited publicly available $S(\alpha, \beta)$ laws for water below 374K, $S(\alpha, \beta)$ thermal scattering date can be custom-made with the LEAPR, THERMR and ACER modules of NJOY 99 [35]. These MCNP5 models can be benchmarked by designing an appropriate experiment to measure the water temperature closest to the irradiation position. In the event that the pool-water

temperature plays a significant role in altering the flux distribution at MURR, the results from the MCNP5 computations can be used to model the temperature variation in a least-squares fit fashion. Then, the parameter π_{Theo} will be modified to become a function of the water temperature.

Appendix 1 Neutron Self-Shielding Factor Calculations using MCNP5

A1.1 Overview

Neutron self-shielding is a process where the neutron flux intensity is reduced within the material placed in a neutron field due to the effective absorbance cross-section of the material. Therefore, for a cubic, strong thermal-neutron absorber placed in an isotropic thermal-neutron flux field, the center of the cube will only receive a fraction of the thermal flux incident on the surface. An example Ref. [120] shows that for a 0.1 mm layer of gold (with a thermal cross-section of ~100 barns) the thermal flux is already reduced by 6%. However, the process is not only limited to thermal-neutrons. If the material has a high resonance absorption cross-section, the flux attenuation will be similar for the epithermal-neutrons. Gold, for instance has a resonance integral of over 1550 barns [33, 34]. Therefore, using the 0.1 mm gold layer as an example, placed in a mono-energetic isotropic epithermal flux field of energy around 5 eV, the epithermal flux will decrease by over 60%.

Naturally, some materials are stronger thermal neutron absorbers than others. Similarly, some materials are stronger epithermal (resonance) absorbers than others. Therefore, in quantifying the neutron self-shielding for various materials, it is convenient to both determine the thermal-neutron self-shielding and the epithermal-neutron self-shielding factors G_{th} and G_{epi}, respectively. The general expression to determine thermal-neutron self-shielding factors G,

155

$$G = \frac{\int_{E1}^{E2} \phi^*(E)\sigma_a(E)d(E)}{\int_{E1}^{E2} \phi(E)\sigma_a(E)d(E)} \quad , \tag{A1.1}$$

where, $\phi^*(E)$ is the real flux spectrum within the target, $\phi(E)$ is the unperturbed flux spectrum at the irradiation position, $\sigma_a(E)$ is the continuous-energy absorption cross-section, $E1$ and $E2$ are the energy bins of the integrations. The factors G_{th} and G_{epi} can be calculated by changing the limits of the integration from 0 eV – 0.44 eV (for G_{th}) to 0.44 eV -10 MeV (for G_{epi}) [13].

However, equation A1.1 can not be solved analytically and is either experimentally or numerically determined [68, 69, 89-91]. Experimentally, G_{th} or G_{epi} are determined by irradiating several thicknesses of the target material in identical configuration in either thermal or epithermal flux conditions. The unperturbed rate (flux) is usually obtained by using very dilute target (i.e., where its mass is less than 10^{-6} grams). In this case, the infinitely dilute or microscopic absorption cross-section of the target is assumed. However, in this work G_{th} or G_{epi} (i.e., equation A1.1) were computed using MCNP5. This approach has been used in references [68, 90, 91] for a number of single-element materials. The objective here is to determine self-shielding factors for a list of selected flux wires and SRMs used in the activation and reactor calibration experiments done in irradiation position ROW2. These include pure Zr and Zn wire, and SRM278 [73] and SRM1633a [70].

A1.2 Neutron Self-Shielding Factors

In the MCNP5 calculations, a detailed geometric model of a Rabbit was created. An SDEF neutron source was defined in the walls of the Rabbit and neutrons were allowed to survive only if they propagate inwards within the volume of the Rabbit. The SDEF neutron source was created such that the target is irradiated in an isotropic neutron flux field. Here, the shape of the flux distribution was obtained from the computed flux spectrum in the ROW2 irradiation position. For the initial calculations, four thicknesses of pure Zr wire ranging in diameter from 0.1 mm to 0.2 mm were modeled. Figure A1.1 shows the MCNP5 model of the Rabbit containing a length of pure Zr wire.

The intrinsic reaction rate of ^{96}Zr was tallied for each Zr wire thickness modeled; in addition to the ^{96}Zr reaction rate from a dummy Zr wire (no actual Zr was modeled). The dummy Zr wire was used to obtain the unperturbed reaction rate. Since ^{96}Zr is very sensitive to epithermal neutrons, a plot of G_{epi} as function of energy (in MeV) was made for each thickness of Zr wire in Figure A1.2.
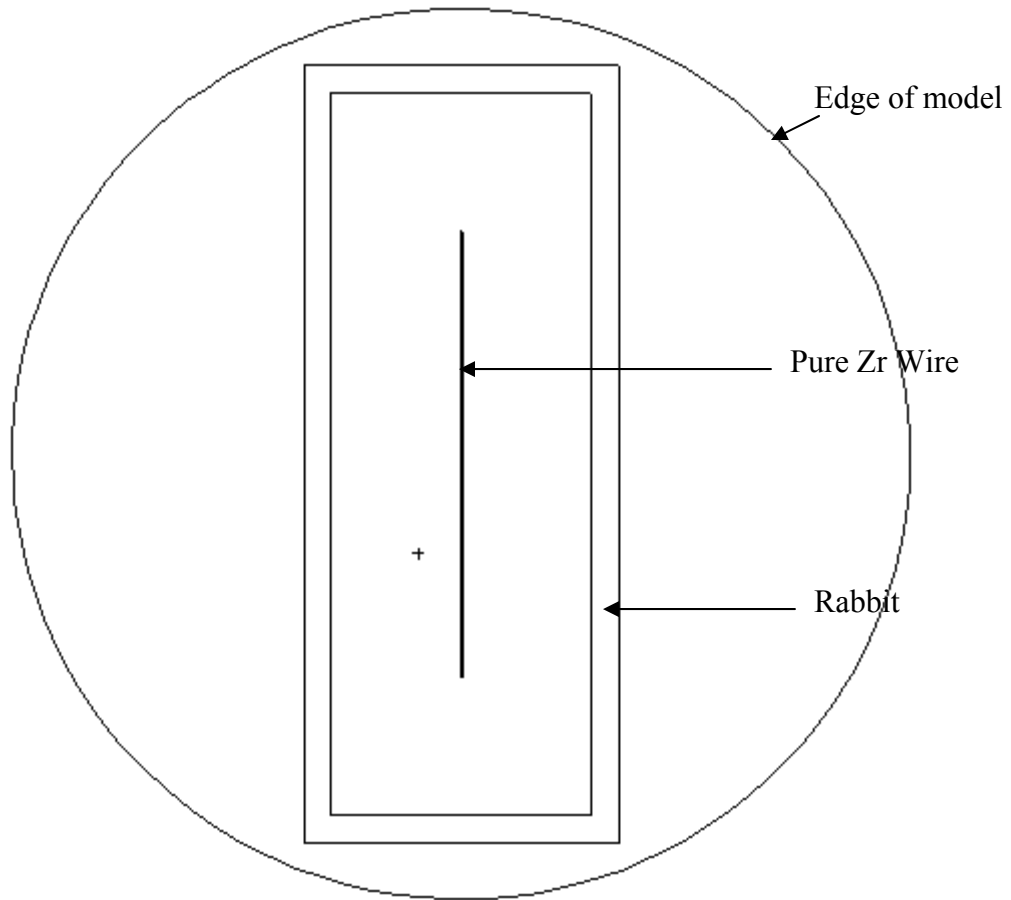
Fig. A1.1 A geometrical representation of the MCNP5 model of the Rabbit containing a length of pure Zr wire.

Figure A1.2 shows an increasing depression in G_{epi} around 0.000338 MeV as the thickness increases. This is expected as the largest resonance peak for ^{96}Zr is at 0.000338 MeV. Next, the computed G_{th} or G_{epi} for ^{94,96}Zr were plotted as a function of wire diameter in mm; the plots are shown in Figure A1.3. As expected, the functions are identical for both ^{94,96}Zr and the effect of the G_{epi} is greater than G_{th}. This is also expected for pure elemental Zr since its total resonance-neutron absorption cross-section is larger

than its thermal-neutron absorption [33]. In either case, significant self-shielding effects (i.e., less then $G = 0.9$) are expected when the wire diameter is greater than ~0.135 mm.
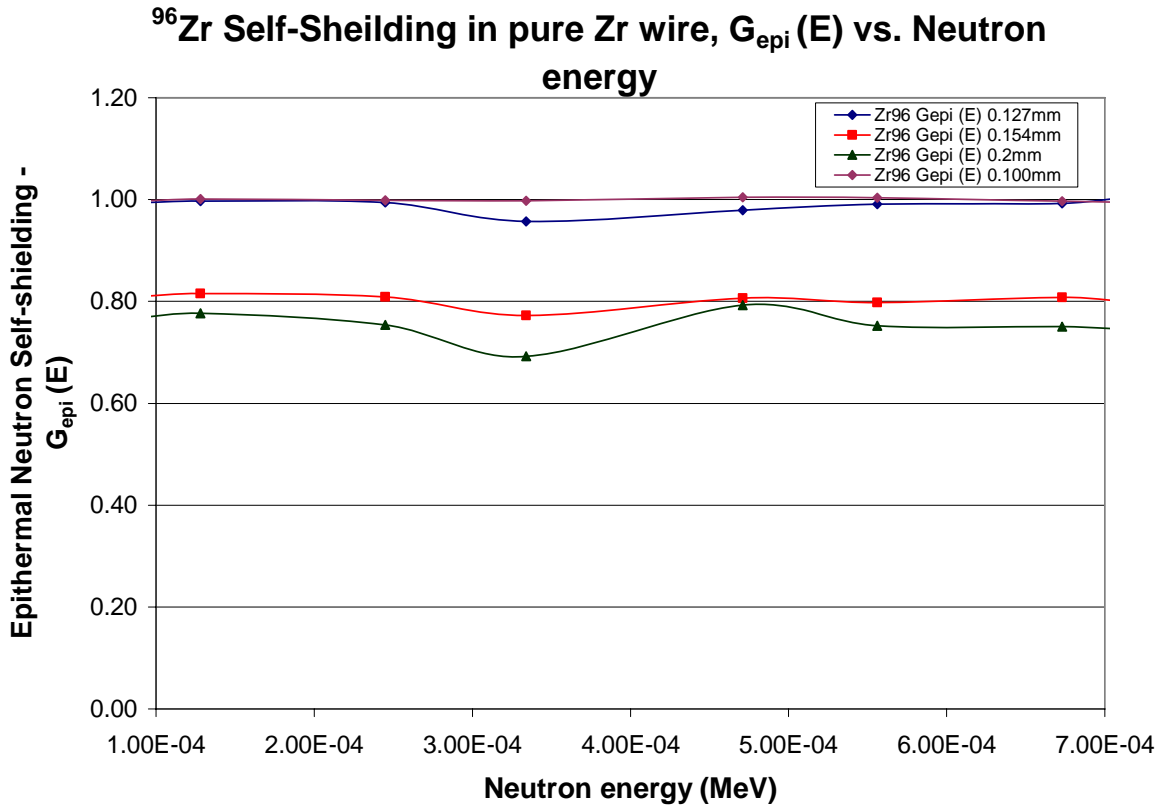
Fig A1.2 A plot of G_{epi} for ^{96,}Zr as a function of energy in MeV for four different thicknesses of pure Zr wire. The plots show an increasing drop in G_{epi} around the effective resonance energy for ^{96}Zr as thickness increases.

159
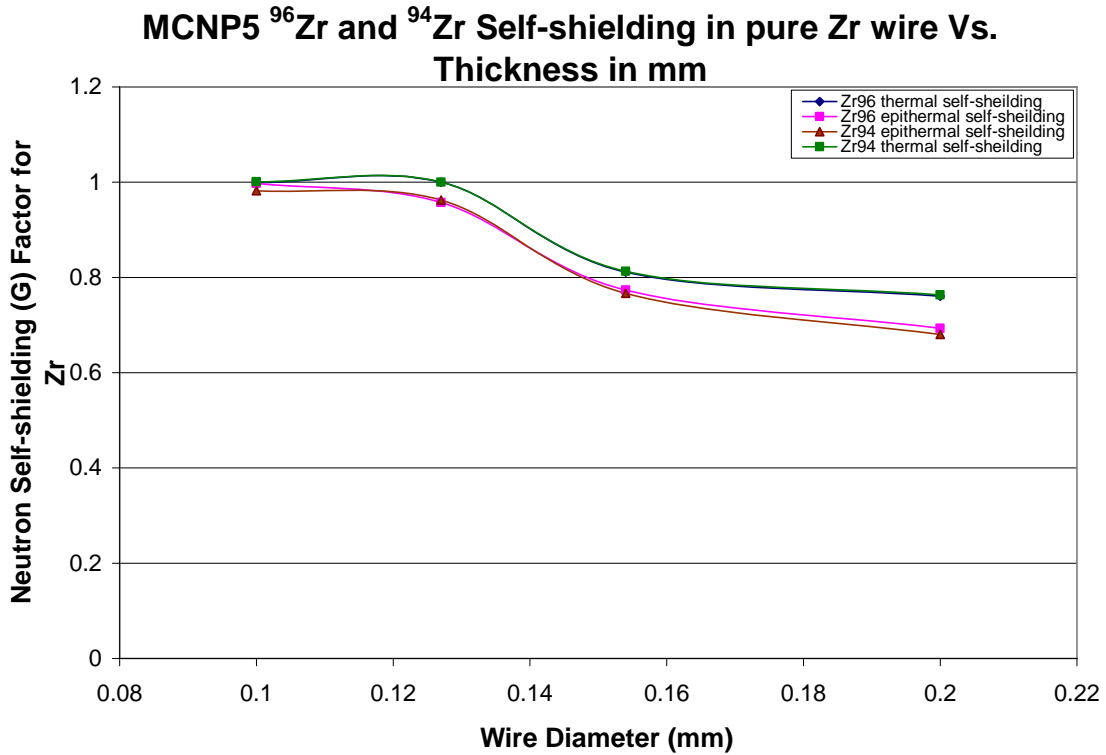
Fig. A1.3 Plots of the computed G_{th} and G_{epi} for ^{94,96}Zr as a function of wire diameter.

G-factor	^{94}Zr/ Pure Zr wire dia. 0.127 mm	^{96}Zr/ Pure Zr wire dia. 0.127 mm	^{68}Zn/ Pure Zn wire dia. 0.25 mm	^{41}K/ SRM278 (NIST% K =3.45)	^{41}K/ SRM1633 (NIST %K = 1.88)
G_{th}	1.00	1.00	1.00	1.00	1.00
G_{epi}	0.96	0.96	0.91	0.99	0.99

Table A1.1 A list of G_{th} and G_{epi} for various flux monitors used in activation and reactor calibration measurements in ROW2. The G_{th} and G_{epi} for the SRM278 and SRM1633a were based on the reaction rates for ^{41}K.

Table A1.1 lists the computed G_{th} and G_{epi} for the actual dimensions of wire used in the activation and reactor calibration experiment done in ROW2 for Zr, Zn, SRM278 and SRM1633a.

A1.3 MCNP5 Input Deck for Self-Shielding Calculations

```
c MCNP ipnut deck for Gth and Gepi Calculations
c
c     Created on: Wednesday, October 22, 2008 at 01:02
  100    0        -800  fill=1
  101    0        -700 -702 706  #102 #103  u=1 $HD PE rabbit
  102    0        -701 -703 705  #103  u=1 $Polystyrene foam
  103    5   -6.52 -709 -707 708  u=1 $Zr wire
  104    1 -0.0013 #101 #102 #103  u=1 $ Air outside rabbit
c
  200    0        800

c   Surface for rabbit
  700       c/z 0 0 1.75
  701       c/z 0 0 1.45
  702        pz 4.375
  703        pz 4.0575
  705        pz -4.0575
  706        pz -4.375
c Surface for Zr wire
  707        pz 4
  708        pz -4
  709       c/z 0 0 0.00635
c edge of model
  800        so 5

mode  n p
c  Material definitaions
m1   7014.60c         0.785  $ air
     8016.60c         0.211 18000.42c        0.004
m2   1001.00c             4  $HD PE density = 0.95g/cm3
     6000.00c             2
m3   1001.00c         0.6667  $MAT
     8016.60c        0.3333
m4   1001.00c           0.5  $MAT Polystyrene (EPS)
     6000.00c           0.5
m5   40096.01c          0.028  $Zr
     40090.66c        0.5145 40091.66c        0.1122 40092.66c        0.1715
     40094.66c        0.1738
m6   40096.66c           1 $Zr96
m7   40094.66c           1 $Zr94
imp:n        1 1r                1        1        0 $ 100, 104
             0  $ 200, 200
imp:p        1 1r                1        1        0 $ 100, 104
             0  $ 200, 200
imp:e        1 5r          $ 100, 200
c
c     SDEF SOURCE DEFINITIONs
sdef pos=d1 rad=d2 $
```

```
     axs 0. 0. 1.
     ext=d3
     erg=d4
     par=n
si2 s 5 6 7
sp2 d 1 1 1
si3 s 8 9 10
sp3 d 1 1 1
si4 H   0 1.05E-09 3.57E-09 6.45E-09 8.37E-09 1.45E-08 2.86E-08 3.50E-08
       4.40e-08 5.56E-08 6.75E-08 7.32E-08 8.18E-08 8.67E-08 9.19E-08
       9.82e-08 1.05E-07 1.71E-07 2.37E-07 2.80E-07 3.15E-07 3.67E-07
       4.45e-07 5.45E-07 6.32E-07 7.37E-07 8.43E-07 9.45E-07 1.15E-06
       2.25e-06 3.56E-06 4.45E-06 5.36E-06 6.57E-06 7.32E-06 8.45E-06
       9.40e-06 1.27E-05 2.15E-05 2.93E-05 3.55E-05 4.78E-05 6.18E-05
       8.25e-05 1.28E-04 3.34E-04 5.56E-04 6.73E-04 9.67E-04 1.02E-03
       2.47e-03 3.23E-03 4.93E-03 5.52E-03 6.92E-03 7.52E-03 8.32E-03
       9.05e-03 1.11E-02 1.85E-02 2.30E-02 2.51E-02 2.89E-02 3.64E-02
       4.61e-02 5.41E-02 8.92E-02 1.47E-01 2.40E-01 3.33E-01 4.33E-01
       5.53e-01 6.75E-01 7.82E-01 9.12E-01 1.18E+00 1.50E+00 1.79E+00
       2.08e+00 2.29E+00 2.36E+00 2.42E+00 2.60E+00 2.87E+00
sp4   0 2.48E-08 4.57E-07 1.07E-06 9.76E-07 4.05E-06 1.21E-05 5.57E-06
       7.37e-06 8.12E-06 6.69E-06 2.63E-06 3.37E-06 1.68E-06 1.65E-06
       1.65e-06 1.48E-06 6.51E-06 1.50E-06 4.21E-07 2.46E-07 3.02E-07
       3.54e-07 3.45E-07 2.43E-07 2.36E-07 2.05E-07 1.71E-07 3.08E-07
       9.57e-07 5.99E-07 2.66E-07 2.37E-07 2.40E-07 1.40E-07 1.73E-07
       1.31e-07 3.56E-07 6.52E-07 3.82E-07 2.28E-07 3.54E-07 3.36E-07
       3.49e-07 5.07E-07 1.06E-06 5.27E-07 2.00E-07 4.16E-07 5.25E-08
       9.18e-07 2.46E-07 3.90E-07 9.64E-08 1.90E-07 7.45E-08 9.34E-08
       7.18e-08 2.04E-07 4.64E-07 1.84E-07 6.57E-08 1.20E-07 1.91E-07
       2.38e-07 1.29E-07 4.93E-07 5.19E-07 5.23E-07 4.01E-07 3.47E-07
       3.77e-07 3.31E-07 2.38E-07 3.02E-07 4.12E-07 3.76E-07 4.45E-07
       1.98e-07 1.75E-07 5.07E-08 1.17E-08 8.55E-08 3.55E-08
si5 L 1.45 1.75
sp5 -21 1
si6 H 0 1.75
sp6 -21 1
si7 H 0 1.75
sp7 -21 1
si8 H -4.0575 4.0575
sp8 -21 0
si9 H 4.0575 4.375
sp9 -21 0
si10 H -4.375 -4.0575
sp10 -21 0
si1 L 0.0 0.0 0.0  $
sp1 1. $
c
c END of SDEF
c
c S(a,b) tables
c
mt2  poly.60t
```

```
c
phys:e
phys:p
phys:n 150 5.0e-6 0 -1 1
nps 7.5e9
print
c
c
fc14 3-Group Flux spectrum in Zr wire
f14:n 103
e14 0.5e-6 0.1 10
c
fc24 Zr94 Rate
f24:n 103
fm24 1 7 102
e24 0.5e-6 0.1 10
c
fc34 Zr94 Rate
f34:n 103
fm34 1 7 102
e34  1.05e-9 3.57e-9 6.45e-9 8.37e-9 1.45e-8 2.86e-8 3.50e-8 4.40e-8
     5.56e-8 6.75e-8 7.32e-8 8.18e-8 8.67e-8 9.19e-8 9.82e-8 1.05e-7
     1.71e-7 2.37e-7 2.80e-7 3.15e-7 3.67e-7 4.45e-7 5.45e-7 6.32e-7
     7.37e-7 8.43e-7 9.45e-7 1.15e-6 2.25e-6 3.56e-6 4.45e-6 5.36e-6
     6.57e-6 7.32e-6 8.45e-6 9.40e-6 1.27e-5 2.15e-5 2.93e-5 3.55e-5
     4.78e-5 6.18e-5 8.25e-5 1.28e-4 2.45e-4 3.34e-4 4.71e-4 5.56e-4
     6.73e-4 7.35e-4 8.62e-4 9.67e-4 1.02e-3 2.47e-3 3.23e-3 4.93e-3
     5.52e-3 6.92e-3 7.52e-3 8.32e-3 9.05e-3 1.11e-2 1.85e-2 2.30e-2
     2.51e-2 2.89e-2 3.64e-2 4.61e-2 5.41e-2 8.92e-2 1.47e-1 2.40e-1
     3.33e-1 4.33e-1 5.53e-1 6.75e-1 7.82e-1 9.12e-1 1.18 1.50 1.79
     2.08 2.29 2.36 2.42 2.60 2.87 3.53 5.41 6.72 7.55 8.27 9.69
c
fc64 Detailed Flux spectrum in Zr Wire
f64:n 103
e64  1.05e-9 3.57e-9 6.45e-9 8.37e-9 1.45e-8 2.86e-8 3.50e-8 4.40e-8
     5.56e-8 6.75e-8 7.32e-8 8.18e-8 8.67e-8 9.19e-8 9.82e-8 1.05e-7
     1.71e-7 2.37e-7 2.80e-7 3.15e-7 3.67e-7 4.45e-7 5.45e-7 6.32e-7
     7.37e-7 8.43e-7 9.45e-7 1.15e-6 2.25e-6 3.56e-6 4.45e-6 5.36e-6
     6.57e-6 7.32e-6 8.45e-6 9.40e-6 1.27e-5 2.15e-5 2.93e-5 3.55e-5
     4.78e-5 6.18e-5 8.25e-5 1.28e-4 2.45e-4 3.34e-4 4.71e-4 5.56e-4
     6.73e-4 7.35e-4 8.62e-4 9.67e-4 1.02e-3 2.47e-3 3.23e-3 4.93e-3
     5.52e-3 6.92e-3 7.52e-3 8.32e-3 9.05e-3 1.11e-2 1.85e-2 2.30e-2
     2.51e-2 2.89e-2 3.64e-2 4.61e-2 5.41e-2 8.92e-2 1.47e-1 2.40e-1
     3.33e-1 4.33e-1 5.53e-1 6.75e-1 7.82e-1 9.12e-1 1.18 1.50 1.79
     2.08 2.29 2.36 2.42 2.60 2.87 3.53 5.41 6.72 7.55 8.27 9.69
c mplot tal 64 loglog leth xlims 1.0e-9 10 freq 4
```

Appendix 2 Material Definitions for MURR core MCNP5 Model

The material definitions for the MURR core model are presented in a format usable by MCNP5. Each nuclide and its respective continuous-energy neutron data are defined by the number **xxxx.yyc** see ref. [24, 32].

xxxx- is defined as the ZAID and is the proton and mass numbers.

yy – is the name of neutron library.

c – is defining the library to be continuous-energy neutron data.

All neutron data libraries with the exception of the .00c libraries can found in the default MCNP5 package. The .00c libraries were made using the raw ENDF-BVII.0 neutron data and [33] processed specifically for the MURR core using the NJOY 99 [35] cross-section handling code. The numbers following the ZAID represents the isotopic composition for the elements in each material and are given as an atom fraction or (with a minus sign) a mass fraction. The densities used in the model are also provided for each material.

```
c   Pressure Vessel water (primary loop)
m1    1001.00c       0.6667      $MAT density = 0.98 g/cc
       8016.60c       0.3333
c   Pressure vessel aluminum structure Al-6110A series
m2    13027.00c        -0.9545    $ MAT density = 2.71 g/cc
       25055.00c        -0.009  12000.62c     -0.011      29063.62c     -0.00552
       29065.00c       -0.00248  14028.62c    -0.010145   14029.62c   -0.0005137
       14030.62c      -0.000341  22000.62c     -0.001     30000.00c     -0.002
       26054.62c  -0.00040915  26056.62c    -0.006423   26057.62c   -0.0001483
       26058.62c   -1.974e-005  24050.62c  -0.00010863 24052.62c   -0.0020973
       24053.62c     -0.0002375  40000.42c     -0.001
c   Reflector Be 200S F series (ref. [39])
```

```
m4    4009.00c       -0.989    $ MAT density = 1.75 cc/g
      14028.62c  -0.0002767  14029.62c  -1.401e-005  14030.62c  -9.3e-006
      26054.62c  -5.8e-005    26056.62c  -0.0009172   26057.62c  -2.2e-005
      26058.62c  -2.8e-006    12000.62c  -0.0002      6000.00c   -0.0012
      13027.00c  -0.0005      8016.60c   -0.0078
c    Graphite - Nuclear grade 2 (ref. [38])
m5    6000.00c      -0.999957 $ MAT  density =1.7 cc/g
      5010.00c       -1e-006  14028.62c  -9.223e-006  14029.62c  -4.67e-007
      14030.62c  -3.1e-007  26054.62c    -5.8e-007    26056.62c  -9.172e-006
      26057.62c  -2.2e-007  26058.62c    -2.8e-008    13027.62c   -1e-005
      20040.21c    -1e-005  22000.62c      -1e-006    23051.42c   -5e-006
c    Boral control blade
m7    13027.00c       0.275   $ MAT density = 2.297 cc/g
      5010.00c        0.11 5011.00c       0.455 6000.00c       0.16
c    Stainless steel 300 series regulating blade
m8    26054.62c    0.0385    $ MAT density = 7.85 g/cc
      26056.62c    0.64204   26057.62c       0.0154
      26058.62c  1.96e-003   24050.62c  8.69e-003   24052.62c     0.16756
      24053.62c  0.019       24054.62c  4.73e-003   28000.50c      0.1
c    Helium
m9    2004.60c          1     $MAT density = 0.1786 g/cc
c    LEU metal foil for Mo-99 Production
m11   92235.00c       0.1975  $MAT density = 19.8 g/cc
      92238.00c       0.7996 92234.00c      0.0029
c    Natural cadmium
m12   48106.65c       0.0125  $MAT density =  8.65 g/cc
      48108.66c       0.0089 48110.66c      0.1249 48111.66c      0.128
      48112.66c       0.2413 48113.66c      0.1222 48114.66c      0.2873
      48116.66c       0.0749
c    Boron
m13   5010.00c          1     $MAT density = 2.25 g/cc
c    Air
m15   7014.60c        0.785   $ MAT density = 0.0013 cc/g
      8016.60c        0.211 18000.42c      0.004
c    Heavy Concrete Shielding
m16   1001.00c         -0.01  $MAT density = 2.4 g/cc
      6000.00c         -0.1   8016.60c     -0.5301   11023.60c      -0.016
      13027.00c        -0.361 14000.60c    -0.3366   20000.64c      -0.0564
      26054.62c  -8.062e-004  26056.62c    -0.012751 26057.62c      -3.058e-4
      26058.62c  -3.892e-005
c  Outer vessel aluminum structure  Al-6110A series
m18   13027.00c     -0.9545  $ MAT density = 2.71 g/cc
      25055.00c       -0.009    12000.62c    -0.011    29063.62c    -0.00552
      29065.00c     -0.00248  14028.62c    -0.010145 14029.62c  -0.0005137
      14030.62c    -0.000341  22000.62c    -0.001     30000.00c    -0.002
```

```
        26054.62c  -0.00040915 26056.62c   -0.006423  26057.62c  -0.0001483
        26058.62c  -1.974e-005 24050.62c  -0.00010863 24052.62c  -0.0020973
        24053.62c   -0.0002375 40000.42c      -0.001
c   High Density polyethylene HDPE
m20  1001.00c         4  $ MAT density = 0.95 g/cc
     6000.00c         2
c   Pool water
m21  1001.00c       0.6667  $ MAT density = 0.9985 g/cc
     8016.60c       0.3333
c   Polystyrene (EPS) in rabbit
m22  1001.00c        0.5  $ MAT density  = 0.25 g/cc
     6000.00c        0.5
c   Material definition for Flux wires
m23  40096.01c        1  $Zr
m24  79197.00c        1  $Au
m25  28000.42c        1  $Nickel
c   Aluminum Al-3003 series cladding  for Uranium Foil (Mo99 Target)
m26  13027.00c      -0.986  $MAT denisty  = 2.71 g/cc
     25055.00c      -0.012 29063.62c   -0.008628 29065.00c    -0.003372
c   Fuel Material -HEU AlU_x Dispersion Type Fuel Ref [37]
m44   –   $ MAT density = 3.83 g/cc
```

References:

1. Levi, H., *George De Hevesy : 1 August 1885-5 July 1966.* Nuclear Physics A, 1967. **98**(1): p. 1-24.
2. Guinn, V., *Nuclear activation analysis 45 years after George Hevesy's discovery.* Journal of Radioanalytical and Nuclear Chemistry, 1980. **59**(2): p. 309-314.
3. Glascock, M.D. *An overview of neutron activation analysis.* 2004 11/05/2004 [cited 2009 5/29]; Available from: http://ecow.engr.wisc.edu/cgi-bin/get/ne/427/edwards/naaoverview.pdf.
4. Beck, J.N., Lamberty,C. M. , *Thermal neutron actiavtion analysis - an important analytical tool.* Applied spectroscopy reviews, 2002. **37**(1): p. 19–55
5. Kucera, J., *The use of neutron activation analysis in environmental and biomedical research.* Nuclear Physics Methods and Accelerators in Biology and Medicine,, 2007: p. 28-32.
6. Laoharojanaphand, S., Dharmavanij, W.; Busamongkol, A., et al *Research and development on activation analysis at the Thailand Institute of Nuclear Technology.* Journal of Radioanalytical and Nuclear Chemistry, 2008. **278**(3): p. 675–679.
7. Bédard, L.P., Wiedenbeck, M.,, *Neutron Activation Analysis, Atomic Absorption and X-Ray Fluorescence Spectrometry Review for 2003.* Geostandards and Geoanalytical Research, 2003: p. 22-25.
8. Bédard, L.P., Wiedenbeck, M.,, *Neutron Activation Analysis, Atomic Absorption and X-Ray Fluorescence Spectrometry Review for 2004-2005.* Geostandards and Geoanalytical Research, 2006. **30**(3): p. 183-186.
9. Bédard, L.P., Wiedenbeck, M.,, *Neutron Activation Analysis, Atomic Absorption and X-Ray Fluorescence Spectrometry Review for 2006-2007.* Geostandards and Geoanalytical Research, 2008. **32**(4): p. 399-403.
10. Steinnes, E., *Neutron activation analysis in the geosciences: lost territory, or new Deal?* Journal of Radioanalytical and Nuclear Chemistry, 2004 **261**(3): p. 701-708.
11. Jarvis, K.E., A. L. Gray; R. S. Houk, *Handbook of Inductively Coupled Plasma Mass Spectrometry.* 1992, New York: Chapman and Hall.
12. Domon, B., Aebersold, R.,, *Mass spectrometry and protien Analysis.* Science 2006. **312**(5771): p. 212-217.
13. De Soete, D., Gijbels, R.; Hoste, J., *Neutron Actiavtion Analysis* Vol. 34. 1972: Wiley - Interscience.
14. Adams, F., *Traceability and analyitical chemistry.* Accred Qual Assur, 1998. **3**: p. 308-316.
15. Stallmann, F.W., Kam, F.B.K. , *Review of unfolding methods for neutron flux dosimetry*, in 1975, ORN CONF-750935--1.
16. De Corte, F., *k0 and Comparator NAA: Influences and Interactions.* Journal of Radioanalytical and Nuclear Chemistry, 2000. **245**(1): p. 157-161.
17. Girardi, F., Guzzi, G.; Pauly, J., *Reactor Neutron Activation Analysis by the Single Comparator Method.* Analytical Chemistry, 1965. **37**(9): p. 1085-1092.

18.   Glasstone, S., *Principles of Nuclear Reactor Engineering*. 1957, New York: D. Van Nostrand Company, Inc.

19.   Lamarsh, J.R., *Introduction to Nuclear Reactor Theory*. 1966, Reading: Addison-Wesley.

20.   Bell, G.I., Glasstone, S.C., *Nuclear Reactor Theory*. 1970, New York: Van Nostrand Reinhold.

21.   Kittel, C., *Elementary Statistical Physics*. 1958, New York: Wiley.

22.   Sears, F.W., Salinger, G.L. , *Thermodynamics,Kinetic Theory, and Statistical Thermodynamics* 3ed. 1975: Addison-Wesley. 331-336, 355-361.

23.   Thornton, S.T., Marion, J.B.,, *Classical dynamics of particles and systems*. 5th ed. 2004, Davis Thomson Books

24.   X-5 Monte Carlo Team, *MCNP — A General Monte Carlo N-Particle Transport Code, Version 5*, D.o. Energy, Editor. 2005, Los Alamos National Laboratory-LA-UR-03-1987.

25.   Trkov, A., *Nuclear Reactions and Physical Models for Neutron Activation Analysis*, in *Workshop on Nuclear Data for Activation Analysis*. 2005: Miramare - Trieste, Italy.

26.   Vandenbosch, R., Huizenga, J.R,, *Nuclear Fission*. 1973, New York: Accademic Press.

27.   De Corte F., M., L., Sordo-El Hammami K. Simonits, A. et al, *Modification and generalization of some methods to improve the accuracy of alpha-determination in the 1/E^(1+alpha) epithermal spectrum.* Journal of Radioanalytical and Nuclear Chemistry, 1979. **52**(2): p. 305-316.

28.   De Corte F., S., A.; De Wispelaere, A. et al *Ko-Measurements and realted nuclear data compliation for (n,y) reactor neutron actiavtion analysis.* Journal of Radioanalytical and Nuclear Chemistry, 1989. **133**(1): p. 3-41.

29.   Brockman, J.D., *Development and Application of the K0-NAA at MURR and Investigation of the Toenail as a Biomonitor for Mg, Zn, Cu, Se and Hg*, in *Chemistry* 2006, University of Missouri Columbia

30.   De Wispelaere, A., De Corte, F.;Bossus, D.A.W et al *Re-determination and re-evaluation of the f and alpha parameters in channels Y4 and S84 of the BR1 reactor, for use in ko-NAA at DSM Research.* Nuclear Instruments and Methods in Physics Research Section A: Accelerators, Spectrometers, Detectors and Associated Equipment, 2006. **564**: p. 636-640.

31.   Mughabghab, S.F., *Atlas of Neutron Resonances* ed. B.N.L. National Nuclear Data Center. Vol. 1. 2006: Elsevier Science.

32.   X-5 Monte Carlo Team, *MCNP — A General Monte Carlo N-Particle Transport Code, Version 5*, D.o. Energy, Editor. 2005, Los Alamos National Laboratory - LA-CP-03-0245.

33.   Chadwick, M.B., Obložinský, P.; Herman, M.; Greene, N.M.;   McKnight, R.D; Smith, D.L.; Young, P.G.;   MacFarlane, R.E.; Hale, G.M.; Frankle, S.C.; Kahler, A.C.; Kawano, T.; Little, R.C.; Madland,D.G., Moller, P.; Mosteller, R.D.; Page, P.R.; Talou, P. ; Trellue, H.; White   M.C. et al., *ENDF/B-VII.0: Next Generation Evaluated Nuclear Data Library for Nuclear Science and Technology* Nuclear Data Sheets, 2006. **Vol. 107**(Issue 12): p. Pages 2931-306.

34. *The JEFF-3.1 Nuclear Data Library*, A.F. Koning, R.; Kellett, M.; Mills, R.; Henriksson, H.; Rugama, Y. , Editor. 2006.

35. MacFarlane, R.E., Muir, D. W.; George, D. C. , *NJOY 99*, RSICC, Editor. 2000, Oak Ridge National Laboratory - PSR-480.

36. Kelly, B.T., *Modelling of the Kinetics of Release of Wigner Energy in Graphite*, U.R. NRL-R-2028(S), Editor. 1989.

37. Matos, J.E., Snelgrove, J.L., *Research reactor core conversion guidebook Volume 4:Fuels* 1992.

38. Marsden, B.J., *Nuclear Graphite for High temperature Reactors*. 2000, IAEA-TECDOC--1238: Risley, Warrington.

39. Tomberlin, T.A. *Beryllium – A unique material In nuclear applications*. in *36th International SAMPE Technical Conference*. 2004: INEEL.

40. Zhou, T., *Benchmarking Thermal Neutron Scattering in Graphite*, in *Nuclear Engineering*. 2006, North Carolina State University.

41. Kulikowska, T., Andrzejewski, K.,. *Parasitic absorption is beryllium blocks of MARIA reactor*. in *International Conference Nuclear Nnergy for New Europe 2002*. Kranjska Gora, Slovenia.

42. Wahba. M., *On the use of Beryllium as thermal neutron filter* Egypt. J. Sol., 2002. **25**(2): p. 215-227.

43. MacFarlane, R.E., *Cold scattering kernel methods*. 1996, Los Alamos national laboratory, LA-UR-98-655.

44. Fultz, B., Kelley,T.; McKerns,M. et al, *Inelastic Neutron Scattering*. 2005: Pasadena.

45. Mattes, M., Keinert, J., *Status of Thermal Neutron Scattering Data for Graphite*. 2005, Institute for Nuclear Technology and Energy Systems (IKE) - INDC(NDS)-0475.

46. Mattes M., K., J., *Thermal Neutron Scattering Data for the Moderator Materials H2O, D2O and ZrHx in ENDF-6 Format and as ACE Library for MCNP(X) Codes*. 2005, Institute for Nuclear Technology and Energy Systems (IKE) - INDC(NDS)-0470.

47. Feshbach, H., *Theoretical Nuclear Physics: Nuclear reactions*. 1992, New York: John Wiley & Sons, Inc.

48. Von Dardel G.F, *A study of interaction of neutrons with moderating materials* Phsyical review 1954. **94**(5): p. 1272-1283.

49. Hawari, A.I., Al-Qasir, I.I.;Mishra, K.K. *Accurate simulation for thermal neutron filter effects in the design of research reactor beam applications* in *ANS Topical Meeting on Reactor Physics* 2006. Vancouver, BC, Canada: Canadian Nuclear Society

50. Freund, A.K., *Cross-section of materials used as neutron momochromators and filters* Nuclear Instruments and Methods in Physics Research Section A: Accelerators, Spectrometers, Detectors and Associated Equipment, 1983. **213**: p. 495-501.

51. Primak, W., *Fast-neutron damaging in nuclear reactors: Its kinetics and the carbon atom displacement rate*. Physical Review C (Nuclear Physics), 1956. **103**: p. 1681-1692.

52. Badr, Y., Ali, Z.; Zahran, A., *Characterization of gamma irradiated polyethylene films by DSC and X-ray diffraction techniques.* Polymer International, 2000. **49**: p. 1555-1560.

53. Díaz Rizo, O., et al., *The slowing-down thickness dependency of some neutron flux parameters for k 0-standardization.* Journal of Radioanalytical and Nuclear Chemistry, 1999. **240**: p. 391-393.

54. Malkawi, S.R., Ahmad, N., *Determination of neutron energy spectrum at a pneumatic rabbit station of a typical swimming pool type material test research reactor.* annals of NUCLEAR ENERGY, 2002. **29**: p. 101-108.

55. Lin, X., D. Alber, and R. Henkelmann, *Calibration of the irradiation channel DBVK at BER-II reactor and feasibility of applying the k0-method at this device.* Journal of Radioanalytical and Nuclear Chemistry, 2003. **257**(3): p. 531-538.

56. Gould, C.R., Sharapov, E. I.;Lamoreaux, S. K. , *Time variability of α from realistic models of Oklo reactors.* Physical Review C (Nuclear Physics), 2006. **74**: p. 1-10.

57. Mahmed, Y.A., Umar,I.M. ; Ewa I.O.B. et al (2006) *An alternative approach to the determination of epithermal flux shaping factor (α) for ko-NAA*. **Volume**,

58. Torkzadeh, F., Manouchechri, F., Mohammedzadeh, A.H. et al, *In-core thermal high neutron fluence measurement by TLD actiavtion method.* Nuclear Instruments and Methods in Physics Research Section A: Accelerators, Spectrometers, Detectors and Associated Equipment, 2007.

59. Beynon, T.D., Moon, J. R. , *Thermal neutron transport near a moderator discontinuity using the method of weighted residuals-I. Theory.* Journal of Physics D: Applied Physics, 1972. **5**: p. 931-949.

60. Matsushita, R., Koyam, R. ;Yamada, S. , *Neutron flux gradients and spectrum changes in the irradiation capsule for reactor neutron activation analysis.* Journal of Radioanalytical and Nuclear Chemistry, 1997. **216**: p. 95-99.

61. Natto, S.A., Lewis, D. G. ; Ryde, S. J. S. , *Benchmarking the MCNP code for Monte Carlo modelling of an in vivo neutron activation analysis system.* Applied Radiation and Isotopes, 1998. **49**(5/6): p. 545-547.

62. Frankle, S.C., Briesmeister,J. F., , *Spectral Measurements in Critical Assemblies: MCNP Specifications and Calculated Results*. 1999, Los Alamos National Laboratory - LA-13675.

63. Shahriarib, M., Sohrabpour,M. , *Borehole parametric study for neutron induced capture gamma-ray spectrometry using the MCNP code.* Nuclear Instruments and Methods in Physics Research Section A: Accelerators, Spectrometers, Detectors and Associated Equipment, 2000. **52**: p. 127-135.

64. Joneja, O.P., Plaschy, M.; Jatuff., F.,, *Validation of an MCNP4B whole-reactor model for LWR-PROTEUS using ENDF/B-V, ENDF/B-VI and JEF-2.2 cross-section libraries.* Annals of NUCLEAR ENERGY, 2001. **27**: p. 701-713.

65. Athari Allafa, M., Shahriarib, M.; Sohrabpour, M. , *Monte Carlo source simulation technique for solution of interference reactions in INAA experiments: a preliminary report.* Radiation Physics and Chemistry, 2004. **69**: p. 461-465.

66. Perret G., K., R.; Hudelot, J.P et al, *Modeling report of the CEA Cadarache MINERVE reactor for the OSMOSE project*, ANL-04/18, Editor. 2004.

67. Jonah, S.A., Liaw, J.R.; Matos, J.E., *Monte Carlo simulations for core physics parametersof he Nigeria Research Reactor-1 (NIRR-1).* Annals of Nuclear Energy, 2007.

68. Goncalves, I.F., Martinho, E.; Salgado, J., *Monte Carlo calculation of epithermal neutron resonance self-shielding factors in foil of different materials* Journal of Radioanalytical and Nuclear Chemistry, 2002. **56**: p. 945-951.

69. Chilian, J.S.P., J., Kennedy, G. et al, *Dependence of therrnal and epithermal neutron self-shielding on sample size and irradiation site.* Nuclear Instruments and Methods in Physics Research Section A: Accelerators, Spectrometers, Detectors and Associated Equipment, 2006. **564**: p. 629-635.

70. *Certificate of Analysis, Standard Reference Material SRM 1633a Coal Fly Ash*, Office of Standard Reference Materials, National Bureau of Standards, US Department of Commerce Washington D.C.

71. *Certificate of Analysis, Standard Reference Material SRM 1577 Bovine Liver*, Office of Standard Reference Materials, National Bureau of Standards, US Department of Commerce, : Washington D.C.

72. *Certificate of Analysis, Standard Reference Material SRM 1573 Tomato Leaves*, Office of Standard Reference Materials, National Bureau of Standards, US Department of Commerce: Washington D.C. .

73. *Certificate of Analysis, Standard Reference Material SRM 278 Obsidian Rock*, Office of Standard Reference Materials, National Bureau of Standards, US Department of Commerce Washington D.C.

74. Chilian, C., Kassakov, J.; St.Pierre, J. et al *Extending NAA to materials with high concentrations of neutron absorbing elements.* Journal of Radioanalytical and Nuclear Chemistry, 2006. **270**: p. 417-423.

75. Szoke, R., Sziklai-László, I. , *Epiboron NAA: An option to analyze unfavorable matrices.* Journal of Radioanalytical and Nuclear Chemistry, 2008.

76. De Corte F., *The standardization of of standardless NAA.* Journal of Radioanalytical and Nuclear Chemistry, 2001. **248**(1): p. 13-20.

77. Akahoa, E.H.K., Nyarkob, B.J.B. , *Characterization of neutron flux spectra in irradiation sites of MNSR reactor using the Westcott-formalism for the ko-neutron activation analysis method.* Applied Radiation and Isotopes, 2002. **57**: p. 265-273.

78. Ojo, J.O. and R.H. Filby, *ZAKI: a windows-based ko standardization code for in-core INAA.* Nuclear Instruments and Methods in Physics Research Section A: Accelerators, Spectrometers, Detectors and Associated Equipment, 2002. **481**(1-3): p. 502-508.

79. Acharya, R., Chatt, A.,, *Characterization of the DAlhousie University SLOWPOKE-2 reactor for ko-NAA and applications to medium-lived nuclides.* Journal of Radioanalytical and Nuclear Chemistry, 2003. **257**(3): p. 525-559.

80. Dung, H.M., Hien, P.D., *The application and development of ko-standardization method of neutron actiavtion analysis at Dalat research reactor.* Journal of Radioanalytical and Nuclear Chemistry, 2003. **257**: p. 643-647.

81.   Nyarko, B.J.B., E.H.K. Akaho, and Y. Serfor-Armah, *Application of NAA standardization methods using a low power research reactor.* Journal of Radioanalytical and Nuclear Chemistry, 2003. **257**(2): p. 361-366.

82.   Chung, Y.S., et al., *Implementation of the k0-NAA method in the NAA#3 irradiation hole of the HANARO research reactor.* Nuclear Instruments and Methods in Physics Research, Section A: Accelerators, Spectrometers, Detectors and Associated Equipment, 2006. **564**(2): p. 702-706.

83.   Siong, W.B., Dung, H.M.:Wood, A.K., et al, *Testing the applicability of the ko-NAA at the MINT's triga MARKII reactor.* Nuclear Instruments and Methods in Physics Research Section A: Accelerators, Spectrometers, Detectors and Associated Equipment, 2006. **564**: p. 716-720.

84.   Buccar, T., et al., *Quality assessment of k0-NAA by statistical evaluation of CRM results.* Acta Chimica Slovenica, 2008. **55**(1): p. 166-171.

85.   Kennedy, G., St-pierre J., *Is the ko Method accurate for elements with high Qo values ?* Journal of Radioanalytical and Nuclear Chemistry, 2003. **257** p. 475-480.

86.   De Corte F., s., A., *Recommended nuclear data for use in the ko-standardization of neutron activation analysis.* Atomic data and Nuclear data tables, 2003. **85**: p. 47-67.

87.   J. Kucera*, J.F., Z. Horak *Calibration of the the reactor neutrun spectrum for the ko-NAA standardization using several apppraoches* Czechoslovak Journal of Physics, 1999. **Vol. 49**(Suppl. S1).

88.   De Corte F., D.W.F., *The use of a Zr-Au-Lu alloy for calibrating the irradiation facility in ko-NAA and for general neutron spectrum monitoring* Journal of Radioanalytical and Nuclear Chemistry, 2005. **263**: p. 653-657.

89.   Krzysztof, P., Jozefowicz, K.,; Beatrycze, P. et al, *Self-shielding effect in neutron spectra measurements for neutron capture therapy by means of activation foils.* Radiation protection dosimetry, 2004. **110**: p. 823-826.

90.   Martinho, E., Goncalves, I.F.; Salgado, J., *Universal curve for epithermal neutron resonance self-shielding factors in foils, wires and spheres.* Applied Radiation and Isotopes 2003. **58**: p. 371-375.

91.   Martinho, E., Goncalves, I.F.; Salgado, J., *Universal curves of the thermal neutron self-shielding factor in foils, wires spheres and cylinders.* Applied Radiation and Isotopes, 2004. **261**: p. 637-643.

92.   Knoll, G.F., *Radiation Detection and Measurements.* 3rd ed. 1999, Ann Arbor: John Wiley & Sons.

93.   Rittersdorf, I., *Gamma Ray Spectroscopy.* 2007, Nuclear Engineering & Radiological Sciences, University of Michigan.

94.   Westphal, G.P., *Loss-free counting: a concept for real time compensation of dead-time and pile-up in nuclear pulse spectroscopy.* Nuclear Instruments and Methods in Physics Research Section A: Accelerators, Spectrometers, Detectors and Associated Equipment, 1977. **146**: p. 605-606.

95.   Upp, D.L., Keyser, R. M.; Gedcke, D. A. et al, *An Innovative Method for Dead Time Correction in Nuclear Spectroscopy* 2006, PerkinElmer Instruments, Inc. ORTEC.

96. Holden, N.E., *Temperature dependence of the Westcott g-factor for neutron reactions in activation analysis* IUPAC, Pure Applied Chemistry, 1999. **71**(12): p. 2309-2315.

97. Diaz Rizo, O., Herrera Peraza,E. F. ; Manso Guevara,M. V. et al, *Development and implementation of the k0-standardization and other parametric methods of INAA in Cuba. Part II.* Journal of Radioanalytical and Nuclear Chemistry, 1999. **240**(2): p. 445-450.

98. *Handbook of nuclear activation cross-sections* D. Brune, Schmidt, J. J. , Editor. 1974, IAEA - Tech.Rep. 156.

99. Ahmed, Y.A., Ewa, I.O.B; Umar, I.M, *Variations in nuclear data and its impact on INAA* Journal of Applied Sciences 2006. **6**(8): p. 1692-1697.

100. Leinweber, G., Burke, J.; Lubitz, C.R. et al, *Neutron capture and total cross-section measurements and resonance parameter analysis of zirconium up to 2.5 keV.* Nuclear science and engineering 2000. **134**: p. 50-67.

101. Lomakin, S.S., Romanvo, V.S.; Bochin, V.P, *Measurement of neutron temperature by means of lutetium isotopes* Atomnaya Energiya, 1968. **24**(4): p. 389-390.

102. St-Pierre, J. and G. Kennedy, *Corrections for neutron activation analysis with non-1/v nuclides using reactor moderator temperature readings.* Journal of Radioanalytical and Nuclear Chemistry, 2007. **271**(2): p. 283-287.

103. Kelley, K., Hoffman, R. D.; Dietrich, F. S. , *Neutron and Charged-Particle Induced Cross Sections for Radiochemistry for Isotopes of Scandium, Titanium, Vanadium, Chromium, Manganese, and Iron.* 2005, Lawrance Livermore National Laboratory, UCRL-TR-211668.

104. De Corte, F., Simonits, A.;De Wispelaere, A. et al *Ko-Measurements and realted nuclear data compliation for (n,y) reactor neutron actiavtion analysis.* Journal of Radioanalytical and Nuclear Chemistry, 1989. **133**(1): p. 3-41.

105. Miller, N.M., Miller, J. C., ed. *Statistics and chemometrics for analtyical chemistry.* 4th ed. 2000, Pearson Education: New York. 263.

106. Laboratory, L.A.N., *MONTEBURNS 2.0 - An Automated, Multi-Step Monte Carlo Burnup Code System*, D.o. Energy, Editor. 2003, RSICC.

107. Laboratory, O.R.N., *ORIGEN 2.2 Isotope Generation and Depletion Code Matrix Exponential Method*, D.o. Energy, Editor. 2002, RSICC.

108. Committee on Medical Isotope Production Without Highly Enriched Uranium, N.R.C., ed. *Medical Isotope Production Without Highly Enriched Uranium.* 2009, The National Academies Press: Washington D.C.

109. Dong-Keun, C., Myung-Hyun, K., *Uncertainty analysis of fission molybdenum production with a nuclear fuel target in a research reactor.* Nuclear Technology 2003. **Vol. 144**.

110. Hofman, G.L., Wiencek, T. C.; Wood, E. L. et al, *"Development of 99Mo Isotope Production Targets Employing Uranium Metal Foils.* Trans. Am. Nucl. Soc., 1997. **77**

111. Vandegrift, G.F., Conner,C.; Wiencekt,T.C.; Hofman,G.L.;Snelgrove, J.L. *Demonstration of 99Mo Production Using LEU Metal-Foil Targets in the*

Cintichem Process. in *Proc. 1999 Int. Mtg. Reduced Enrichment for Research and Test Reactors*. 1999. Budapest, Hungary.

112. Dennis, J.A., *Neutron flux and energy measurements*. Phys. Med. Biol., 1966. **11**: p. 1-14.

113. Rogus, R.D., Harling, O.K.; Yanch, J.C., *Mixed field dosimetry for epithermal neutron beams for boron neutron capture therapy at the MITR-II research reactor*. Medical Physics 1994. **21**.

114. Crow, M.L., Jeng, U.;Nunes, A.C. et al *Thermal neutron measurements of the Rhode Island Nuclear Science Center reactor aftere conversion to a compact low enriched unranium core*. Nuclear Instruments and Methods in Physics Research Section A: Accelerators, Spectrometers, Detectors and Associated Equipment, 1995. **365**: p. 433-445.

115. Askew, J.R., Fayers, F. J., Kemshell, P. B., *A general description of the lattice code WIMS*. J. British Nuclear Energy Society, 1966. **564**.

116. McElroy, W.N.e.a., *SAND-II Neutron Flux Spectra Determination by Multiple Foil Activation Iterative Method*. 1967, AWRL-TR-67-41.

117. Nigg, D.e.a., *Collaborative Physical And Biological Dosimetry Studies For Neutron Capture Therapy At The RA-1 Research Reactor Facility* 2004, INEEL/CON-04-02353.

118. National Nuclear Data Center, *Benchmarking of the ENDF- IV data* 1977, BNL-NCS-21118 (ENDF-230).

119. Osac, E.K., Nyarko, B. J. B.; Scrfor-Armah, Y. et al, *An alternative method for the measurement of thermal neutron flux (modified cadmium ratio method)*. Journal of Radioanalytical and Nuclear Chemistry, 1998. **238**(1-2): p. 105-109.

120. Friedlander, G., Kennedy, J.W.; Macias, E. S. et al ed. *Nuclear and radiochemistry*. 3rd ed. 1981, John Wiley & and Sons, Inc: New York.

VITA

Nickie Peters (Belmont, St Vincent and the Grenadines W.I) graduated Suma Cum Laude from Coppin State University in 2003 with a B.S. in chemistry and computer science. In 2001, Nickie was awarded a REU-NSF fellowship at Indiana University, Bloomington, to do research in Nuclear Chemistry. On several occasions, he received NCAA division 1 All-American Academic awards (2002-2003). He was given the Coppin State's Department of Natural Science award and was inducted into the school's academic honour society.

In 2003, he began graduate studies in chemistry at Indiana University, Bloomington after being awarded a full fellowship to work under the guidance of distinguished Professor, Victor E. Viola, Jr. In 2006, he completed a MS degree in Nuclear Chemistry at Indiana and transferred to University of Missouri to complete his PhD in Radiochemistry under the guidance of Professor J. David Robertson. Since then, he has received prestigious fellowships from the university, as well as from Idaho National Laboratories to attend its summer school sessions. In 2008, he was inducted into the International Golden Key academic honour society and April 2009 he was awarded the first ever Dr. Deward "Wes" Efurd Memorial Scholarship for outstanding graduate student in radiochemistry.